Dynamic behaviour and fragmentation of quasi-brittle materials: application to rock fragmentation by blasting

Ahmed Rouabhi

ECOLE DES MINES
DE PARIS

Collège doctoral

T040120AROU

N° attribué par la bibliothèque
/__/__/__/__/__/__/__/__/__/__/

THÈSE

pour obtenir le grade de

DOCTEUR DE L'ÉCOLE NATIONALE SUPÉRIEURE DES MINES DE PARIS

SPÉCIALITÉ : TECHNIQUE ET ECONOMIE DE L'EXPLOITATION DU SOUS-SOL

présentée et soutenue publiquement par

Ahmed ROUABHI

le 20 Janvier 2004

Comportement et fragmentation dynamiques des matériaux quasi-fragiles

⋆⋆⋆

Dynamic behaviour and fragmentation of quasi-brittle materials

Application to rock fragmentation by blasting

Directeur de thèse : Michel TIJANI

Jury

M. Alain MILLARD	Professeur	Commissariat à l'Énergie Atomique	Rapporteur
M. Peter MOSER	Professeur	Université de Leoben-Autriche	Rapporteur
M. Nicolas CHEIMANOFF	Professeur	École des Mines de Paris	Examinateur
M. Philippe WEBER	Professeur	École des Mines d'Alès	Examinateur
M. Hédi SELLAMI	Docteur	École des Mines de Paris	Examinateur
M. Michel TIJANI	Professeur	École des Mines de Paris	Examinateur

Centre de Géotechnique et d'Exploitation du Sous-Sol - École des Mines de Paris
35, Rue Saint-Honoré - 77305 Fontainebleau Cedex

Acknowledgements

This thesis is in keeping with the scope of two projects. The first one (DBF), carried out jointly by the École des Mines de Paris and the University of Leoben (Austria), try to get a better understanding of the mechanisms which cause fragmentation of rock materials. The second project (LESS FINES), is an European project which seeks to find methodologies that minimize the generation of fine materials in open pit mines.
The work presented in this dissertation would not have been possible without the support and the interaction with several other persons.

I would like to acknowledge my advisor, Michel TIJANI, for his patient guidance and helpful suggestions during the past three years. His knowledge of computational mechanics is extensive, and I feel very fortunate to have been one of his students. I wish him a fulfilling and happy future.

I would also like to thank Nicoals CHEIMANOFF for giving me the opportunity to do this work, for serving on my thesis committee and for many helpful suggestions during my first year.

I am especially grateful to Peter MOZER for his guidance and for the many discussions with him, which were a source of stimulation. Collaborations with his team are gratefully acknowledged.

I am also grateful to Alain MILLARD and Philippe WEBER for having agreed to be part of my thesis committee.

I would like to thank Hédi SELLAMI for serving on my thesis committee and for the many conversations with him.

Special thanks goes to Damien GOETZ who generously supported me and who patiently corrected my English in several situations.

I was fortunate to meet Finn OUCHTERLONY. The many conversations with him were of great importance in my understanding of certain points.

Last, but not least, I thank all my colleagues of the CGES center and all my friends for their support in hard times during the last three years. I am also grateful to Marie-Philomène PETITIMBERT for providing help in realizing this publication and for preparing the defence of my thesis.

A. Rouabhi

Abstract

This thesis seeks to find a computational methodology to simulate both the behaviour and the fragmentation of quasi-brittle materials, such as rocks and concrete, under dynamic loadings. Such a methodology will help to a better understanding of the explosive rock breakage mechanisms and, as consequence, will contribute in the optimization of blasting performances. In this study, we consider that the fragmentation process is a natural extension of the fracture process. In order to describe the dynamic fracture process, a suitable phenomenological constitutive model is developed and implemented in a finite element code. As for the dynamic fragmentation, it is treated by a post-processing analysis based on the history of the material's thermodynamic state.

To reproduce the macroscopic behaviour of quasi-brittle materials including load-induced anisotropy due to cracking, the internal variables method based on continuum thermodynamics is used. A scalar internal variable is introduced to model, at the macroscopic level, the strain softening under compressive loadings. Under tensile loadings, a second-order symmetric tensor is used to describe the essential features of the induced anisotropic damage. Under complex loadings, these two models are coupled and the crack closing-reopening effect is also treated. The integration of the developed model in the finite element code VIPLEF3D has led to the development of a relaxation method characterized by an explicit updating of the state variables.

Concerning the dynamic fragmentation, from laboratory blasting tests, a general formulation of predicting the fragment size distribution is provided. In this formulation, a mean fragment size is linked to a mechanical quantity, which is assumed to be the origin of the fragmentation process, by an intrinsic function which can be identified by using suitable laboratory fragmentation tests. This mechanical quantity is given by the resolution of the Initial Boundary-Value Problem where the developed constitutive model is considered.

Finally, the complete approach is then applied to the modelling of the fracture and the fragmentation of chamber blasting tests of cylindrical rock material samples.

KEY-WORDS: quasi-brittle materials / dynamic behaviour / dynamic fragmentation / constitutive laws / internal variables method / anisotropic damage / plasticity / viscoplasticity / softening / numerical simulations / blasting.

Résumé

Le but de cette thèse est de trouver une méthodologie numérique pour simuler le comportement et la fragmentation des matériaux quasi-fragiles, tels que les roches et le béton, sous sollicitations dynamiques. Une telle méthodologie aidera à une meilleur compréhension des mécanismes de fragmentation des roches à l'explosif et, par conséquent, contribuera dans l'optimisation des performances du tir à l'explosif. Dans cette étude, on considère que le processus de la fragmentation est une extension naturelle de celui de la rupture. Afin de décrire ce dernier processus, un modèle de comportement phénoménologique adapté aux matériaux considérés est développé et implémenté dans un code de calcul par éléments finis. Quant à la fragmentation dynamique, elle est traitée par une analyse en post-traitement basée sur l'historique de l'état thermodynamique du matériau.

Pour reproduire le comportement macroscopique des matériaux quasi-fragiles incluant l'anisotropie induite par le chargement, la méthode des variables internes basée sur la thermodynamique des milieux continus est employée. Une variable interne de type scalaire est introduite pour modéliser, au niveau macroscopique, l'adoucissement du matériau suite à des chargements de compression. Sous des chargements de traction, un tenseur symétrique du second ordre est utilisé pour décrire l'endommagement anisotrope induit. Sous des chargements complexes, ces deux modèles sont couplés et l'effet de fermeture-réouverture des fissures est également traité. L'intégration du modèle développé dans le code éléments finis Viplef3d a conduit à l'élaboration d'une méthode de relaxation caractérisée par une actualisation explicite des variables d'état.

Concernant la fragmentation dynamique, à partir d'essais de fragmentation au laboratoire, une formulation générale permettant de prédire la distribution des fragments est fournie. Dans cette formulation une taille moyenne de fragments est liée à une grandeur mécanique, supposée être l'origine du processus de la fragmentation, par une fonction intrinsèque qui peut être identifiée en utilisant des essais adéquats de fragmentation. Cette grandeur mécanique est donnée par la résolution du problème aux limites où le modèle rhéologique est utilisé.

Enfin, l'approche complète est alors appliquée à la modélisation des essais de rupture et de fragmentation, en chambre, d'échantillons cylindriques de roches.

Mots-clés: matériau quasi-fragile / comportement dynamique / fragmentation dynamique / lois rhéologiques / méthode des variables internes / endommagement anisotrope / plasticité / viscoplasticité / adoucissement / simulations numériques / tir à l'explosif.

Contents

Introduction

La rupture séquentielle mène à la fragmentation. Un des aspects les plus importants de la fragmentation dynamique est qu'un corps de matériau fragile ou quasi-fragile, à la fin du processus de la rupture, est divisé en de nombreux morceaux. Dans des conditions de chargement quasi-statique, un corps est souvent cassé seulement en deux morceaux. Sous des vitesses de chargement très élevées où de fortes contraintes atteintes dans un temps très court, le même corps se casse par fragmentation en de nombreux morceaux. La fragmentation joue un rôle important dans une grande variété de processus industriels dans laquelle on désire causer la fragmentation de la manière la plus efficace et la plus contrôlée. Ainsi, l'élaboration de méthodes efficaces et sûres pour l'abattage des roches à l'explosif est d'intérêt considérable pour l'industrie minière. Les opérations d'abattages réussies peuvent mener à réaliser la distribution la plus appropriée des fragments de roche avec un coût de production minimum. Néanmoins, jusqu'à aujourd'hui, la fragmentation dynamique avait été en dehors de la province des méthodes théoriques générales et a été étudié principalement avec l'utilisation de méthodes ad hoc basées sur une variété d'hypothèses non contrôlables et parfois mutuellement contradictoires.

Avec le développement des ordinateurs à grande vitesse, des efforts considérables ont été orientés pour élaborer des modèles continus (Grady et Keep, 1980; Preece et al, 1994), discontinus (Potyondy et Cundall, 1996; Donzé et al, 1997) et continus-discontinus (Munjiza et al, 1995) afin de décrire la fracturation et la fragmentation. D'autres chercheurs ont préféré appliquer une approche micro-statistique (Curran et al, 1987) au problème de la fracturation et de la fragmentation dynamiques des solides. De nos jours et à la connaissance de l'auteur, l'approche la plus appropriée n'a pas été identifiée. Actuellement, il y a une variété de modèles numériques traitant la rupture et la fragmentation mais qui sont loin d'aboutir à une prévision fiable et précise de la distribution granulométrique et ce à partir de la connaissance de la géométrie, des propriétés mécaniques et physiques (dynamiques et statiques), des conditions initiales et des conditions aux limites. Il est en dehors de la portée de ce rapport de décrire tous les modèles disponibles et donc la revue de la littérature sera illustrative plutôt qu' exhaustive.

Il semble raisonnable de dire que la fragmentation dynamique est le résultat d'un problème couplé impliquant l'initiation et la propagation des fissures dans un milieu initialement intact et la formation de fragments isolés. Ainsi, les aspects du continu et du discontinu avec la transition continu-discontinu, sont tous présents. Malheureusement, d'un point de vue de la mécanique des milieux continus, il n'est pas possible de tenir compte de la formation explicite des fragments. D'autre part, la mécanique de la rupture en dynamique ne peut pas également traiter, en même temps, un grand nombre de fissures. Afin de surmonter ces limitations, dans notre approche, nous suivons l'idée qui considère le processus de la fragmentation comme étant une extension naturelle de celui de la rupture. En d'autres termes, nous supposons que nous pouvons séparer la rupture de la formation des fragments (Ortiz R., 2000). Pour décrire la rupture dynamique, un modèle phénoménologique, conforme avec la thermodynamique des milieux continus, est développé. Une fois le processus de la rupture est achevé, on procède à un post-traitement basé sur l'historique de l'état thermodynamique du milieu. Ensuite, un modèle de fragmentation est employé pour produire la distribution granulométrique.

Le reste de ce rapport est organisé de la façon suivante. Le chapitre I traite une formulation générale du problème de la fragmentation dynamique. Le lien entre le problème aux limites est également présenté. En chapitre II, un modèle de comportement des matériaux quasi-fragiles sous sollicitations dynamiques est présenté. Des questions au sujet de l'influence de la vitesse de chargement et des pressions hydrostatiques sur la rupture dynamique sont explorées. L'anisotropie induite par le chargement est également présentée en chapitre II. Enfin, les simulations numériques de la rupture et de la fragmentation d'échantillons de roches et la validation de l'approche complète sont présentées en chapitre III. Dans ce chapitre nous développons également une solution analytique du problème dit "de cavité" et nous discutons l'interaction explosif-matériau.

Sequential fracture leads to fragmentation. One of the most important aspects of dynamic fragmentation is that a body of brittle or quasi-brittle material, at the end of the fracturing sequence, is divided into many parts. Under conditions of slow loading, quasi-static fracture often breaks the body only into two pieces. On the other hand, under very high rates of loading where large stresses are achieved in a very short time, the same body fails by fragmentation into numerous pieces. Fragmentation plays an important role in a wide variety of industrial process in which one desires to cause fragmentation in the most efficient and controlled manner. Thus, the development of efficient and safe methods for breaking rocks with explosives is of considerable interest to the mining industry. Successful blasting operations can lead to achieve the most suitable distribution of rock fragments with a minimum total mining production cost. Nevertheless, until now the dynamic fragmentation process had been outside the province of general theoretical physics methods and was investigated primarily with the use of *ad hoc* methods based on a variety of uncontrolled and sometimes mutually contradicting assumptions.

With the advance of high-speed computer methods, considerable efforts have been directed toward developing continuum (Grady and Keep, 1980; Preece et al, 1994), discontinuum (Potyondy and Cundall, 1996; Donzé et al, 1997) and continuum-discontinuum (Munjiza et al, 1995) descriptions of fracture, fragmentation, and wave propagation to evaluate complex fracturing events. Others workers have preferred to apply a microstatistical fracture mechanics approach (Curran et al, 1987) to the problem of dynamic failure and fragmentation of solids. Until now, as far as the author knows, the most appropriate approach has not been identified. There are currently a variety of numerical models dealing with fracture and fragmentation which are far from achieving the ultimate goal to get reliable and accurate prediction of the fragment size distribution from the set of geometry parameters, material properties (dynamic and static), initial conditions and boundary conditions. It is outside the scope of this report to describe all the models available and therefore the literature review will be illustrative rather than exhaustive.

It seems reasonable to say that dynamic fragmentation is the result of a coupled problem involving the initiation and the propagation of cracks in a previously intact material and the formation of isolated fragments. Thus, aspects of both continuum and discontinuum with transition from continuum to discontinuum, are present. Unfortunately, from a continuum mechanics point of view, it is not possible to take into account the explicit formation of discrete fragments. On the other hand, dynamic fracture mechanics is also unable to treat, at the same time, a great number of cracks. In order to overcome these limitations, in our approach, we follow the idea that considers the fragmentation process as a natural extension of the fracture process. In other words, we assume that we can separate the fracture from the formation of discrete fragments (Ortiz R., 2000). To describe the dynamic failure, a continuum phenomenological model, consistent with thermodynamics, is developed. When the fracture process is complete, the history of the thermodynamic state is post-processed and used in a fragmentation model to produce fragment size distribution.

The remainder of this report is organized in the following way. Chapter I deals with a general formulation of the dynamic fragmentation problem. The link between the Initial Boundary-Value Problem is also presented. In chapter II, a constitutive modelling of quasi-brittle materials behaviour under dynamic loading conditions is presented. Questions concerning the influence of the rate and the hydrostatic pressure effects on the dynamic fracture are explored. The load-induced anisotropy is also introduced in chapter II. Finally, Numerical simulations of laboratory rock fragmentation by blasting and validation of the complete approach are presented in Chapter III. In this chapter we develop also an analytical solution of the cavity problem and we discuss the explosive-material interaction.

Chapter I

Dynamic fragmentation

Sous l'effet d'une charge impulsive, divers matériaux solides se fragmentent en de nombreux morceaux. Une telle charge peut être due à l'impact avec un autre corps, une radiation énergétique fournie, par exemple, par des rayons X, un choc thermique, une onde de choc, etc. La fracturation et la fragmentation des matériaux sont en général opposées à leur résistance. En effet, d'un point de vue stabilité d'une structure, elles sont indésirables. Cependant, il y a une large gamme de procédés industriels tels que le tir à l'explosif, la démolition, le concassage, le découpage, etc, où la fracturation et la fragmentation deviennent désirables.

La fragmentation dynamique des matériaux quasi-fragiles est un processus impliquant un certain nombre de mécanismes physiques. Dans la plupart des cas, ce processus est trop complexe pour être traité seulement par des théories déterministes, des approches statistiques doivent être également considérés. Un travail pionnier, incorporant des considérations statistiques, sur la fragmentation des matériaux ductiles a été rapporté par Mott (1947). Des aspects statistiques et géométriques de la fragmentation des matériaux fragiles ont été introduits par Grady et Kipp (1985).

De nos jours, probablement les modèles théoriques les plus appliqués sont ceux de Grady (1982) et de Gleen et Chudnovsky (1986) qui utilisent des approches énergétiques pour prédire la taille des fragments. Récemment, la modélisation de la fracturation, que se soit dans un but de prévention de la rupture ou de la fragmentation, a été l'objet de plusieurs calculs numériques. Toutefois, malgré ces efforts considérables, une description théorique cohérente du processus de la fragmentation n'est pas encore disponible.

L'objectif de ce chapitre est d'analyser, à partir de l'observation expérimentale, le processus de la fragmentation afin de mettre au point une approche théorique du problème.

Le concept de la fragmentation homogène et celui de la fragmentation hétérogène sont introduits. Par ailleurs, pour relier la taille des fragments aux sollicitations auxquelles le milieu a été soumis, deux modèles basés sur des explications physiques sont présentés. Le premier modèle utilise l'approche classique du bilan énergétique, quant au deuxième, il est basé sur la notion de la zone de cohésion. La formulation générale du problème, adaptée dans la présente thèse, est donnée à la fin de ce chapitre. La relation entre la taille des fragments et le problème mécanique aux limites est identifiée.

I.1 Introduction

Several materials fail by fragmentation into numerous pieces when subjected to rapid energy input. Such rapid energy input may be due to impact with another body, high-energy radiation provided, e.g., by lasers or X-rays, rapid temperature change, shock wave, etc. Fracture and fragmentation of engineering materials are in general opposite to the strength of materials. When considered from the point of view of structure stability, they are undesirable. However, there is a whole range of industrial processes such as blasting, demolition, crushing, cutting, etc., which are possible only because of the ability of materials to fracture or fragment.

The dynamic fragmentation of quasi-brittle materials involves a number of physical mechanisms. In most cases, this process is too complex to be treated only by using deterministic

theories, statistical approaches must also be considered. Pioneering work incorporating statistical aspects for ductile fragmentation was reported by Mott (1947). The statistical and geometrical aspects of brittle fragmentation were introduced by Grady and Kipp (1985).
To date, perhaps the most widely applied theoretical models of the fragmentation process are those of Grady (1982) and Glenn and Chudnovsky (1986) which involve global energy balance to predict fragment sizes. Very recently, modelling fracture, whether with an aim of preventing failure or of inducing considerable fracture and fragmentation of material, has been carried out by large numerical simulations. In spite of these considerable efforts, a consistent theoretical description of the fragmentation process is not yet available.
The purpose of the present chapter is to analyse, from laboratory experiments, the fragmentation process with an aim of a theoretical formulating of the problem.
The concept of homogeneous and heterogeneous fragmentation are introduced and it will be shown that the fragmentation is closely connected with an extremely inhomogeneous distribution of the stresses over the target. In order to relate the fragment size to the input loading, two physics models are discussed. The first one deals with the energy balance concept. The second concerns the cohesive surfaces approach. In the final section, a general formulation of the dynamic fragmentation is provided. In this formulation the fragment size distribution is connected to the Initial Boundary-Value Problem which involves the complexities of stress loading, geometry, and the interaction of stress and relief waves.

I.2 Experimental observations

Experimental investigations were done with the collaboration of the Department of Mining Engineering of the University of Leoben (Peter Moser and co-workers).
All blasting experiments were done in a blasting chamber that allowed to collect close to 100% of the blasted material. Collected fragments are then screened in order to determine the fragment size distribution. All samples were blasted with a constant 5 mm diameter PETN charge.
In what follows we will consider results of three cylindrical shaped limestone samples. The first has a diameter of 300 mm and a height of 500 mm, the second has a diameter of 200 mm and a height of 260 mm and the third has a diameter of 100 mm and a height of 200 mm. The screened muck-pile gives the particle size distributions of Fig. I.1.
Other interesting tests were done, among them we can mention the following two tests. The first one was done with an aim of identifying the origin of fine materials. Indeed, a cylindrical concrete sample composed with 50% of magnetic concrete and 50% of non-magnetic concrete, was built. Fig. I.2 shows such a sample.
In this figure, the black color is the magnetic concrete, while the gray one is the non-magnetic concrete. It should be emphasized that the interface between the two continua was tested and obtained results showed that it does not represent a weakness plan for the sample. The result of the test blast is shown in Fig. I.3 in terms of the fragment size distributions. As can be seen, the fragmentation curve of the magnetic and the non-magnetic concrete are ranging from fine particles to big ones. This result shows clearly that particles coming from either the inner part (magnetic concret) or the outer part (non-magnetic concrete) of the sample are well distributed. This result disagrees with classical ideas which assume that fine materials are generated only from regions near the blasthole (Ortiz R., 2000).
The second test was done with an aim of identifying the effect of boundary conditions. For this purpose, a magnetite concrete cylindrical sample, confined by a steel tube, was blasted. The blasting result is that the confined sample was intact with no visible cracks (Fig. I.4). This result consolidates the fact that the fragmentation event can be influenced not only by incident waves but also by reflected waves.

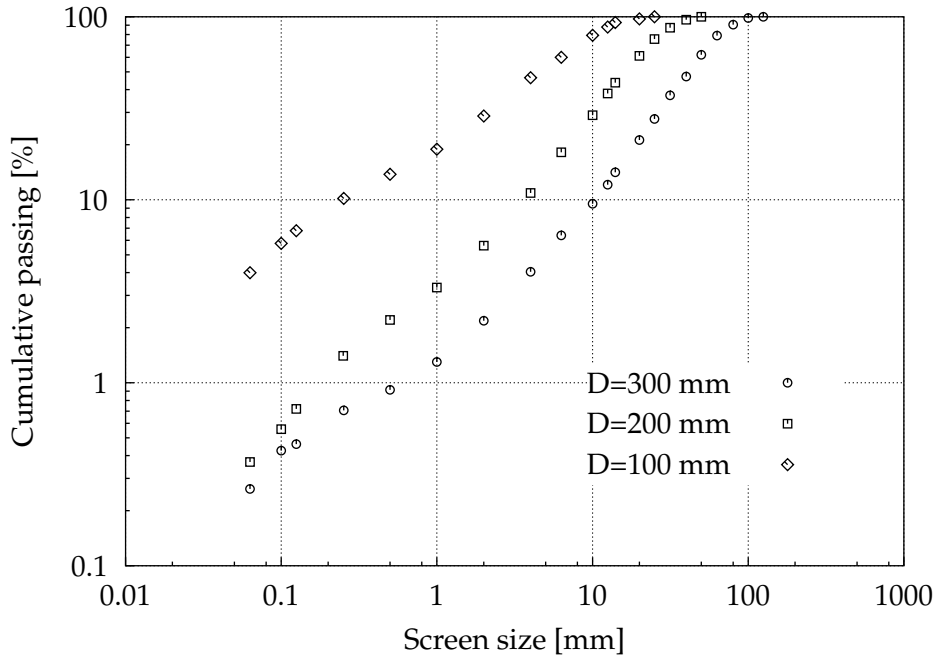

Figure I.1: Particle size distributions (D=Diameter)

Figure I.2: A section of the composite concrete cylinder

In the following sections, we propose a formulation of the dynamic fragmentation problem that can interpret the above experiments.

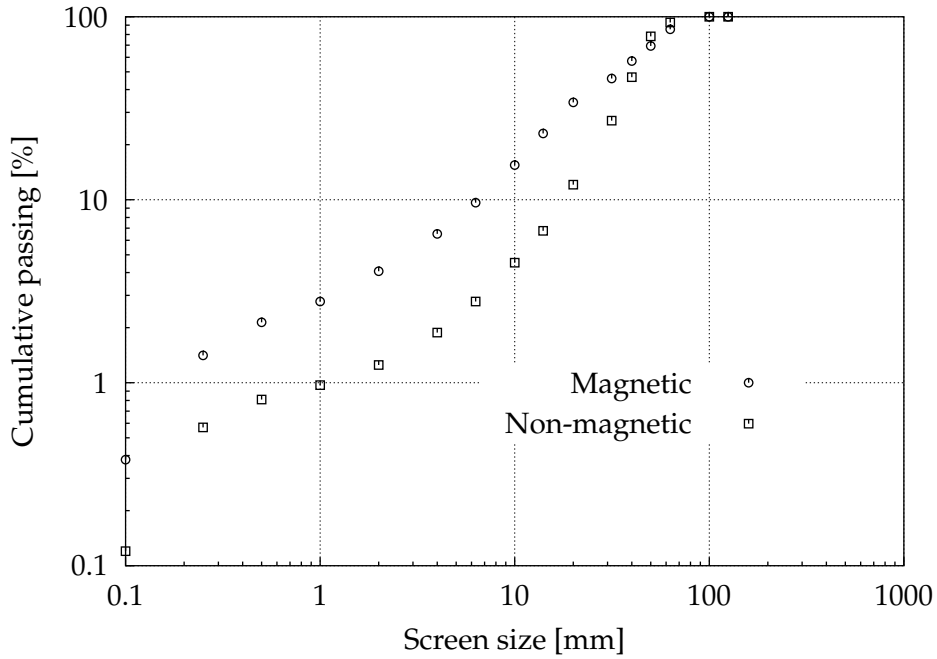

Figure I.3: Particle size distributions of the composite concrete cylinder

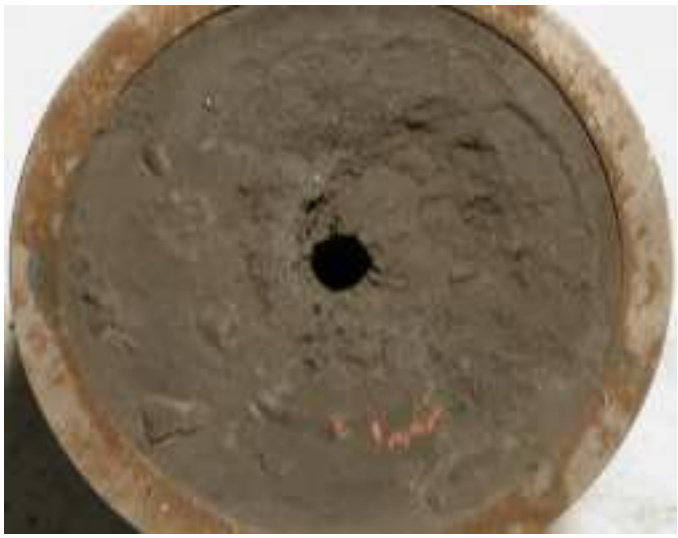

Figure I.4: Confined concrete cylinder after blasting

I.3 Theoretical formulation

I.3.1 General considerations

A theoretical understanding of dynamic fragmentation requires a satisfactory statistical as well as physical explanation. Even in situations of perfect homogeneous loading of perfect symmetric body, the process of breakup is never deterministic, leading to a distibution in fragment sizes and shapes. Before going further, it is interesting to point out some concepts which will be useful for later formulations.

Let Π be a sample space and let $X : \Pi \to \mathbb{R}$ be a continuous random variable. The propability density function (probability distribution) of X is the positive function $f : \mathbb{R} \to \mathbb{R}_+$, such that for any interval $[a,\ b]$ the probability of the event $\{\omega \in \Pi /\ a \leq X(\omega) \leq b\}$ can be computed as

$$P\left(a \leq X \leq b\right) = \int_a^b f(x)dx \tag{I.1}$$

$f(x)$ must satisfy

$$f \geq 0 \ \text{ and } \ \int_{-\infty}^{\infty} f(x)dx = 1 \tag{I.2}$$

The cumulative distribution function of X is the function $F : \mathbb{R} \to [0,\ 1]$ defined by

$$\forall\ x \in \mathbb{R}, \quad F(x) = P\left(\{\omega \in \Pi : X(\omega) < x\}\right) = \int_{-\infty}^{x} f(y)dy \tag{I.3}$$

$F(x)$ is the probability that X will assume a value less than or equal to x. The function F has the following characteristics:

$$\begin{cases} \text{F is an increasing function} \\ \lim\limits_{x\to-\infty} F(x) = 0 \text{ and } \lim\limits_{x\to+\infty} F(x) = 1 \\ F'(x) = f(x)\ \forall\ x \text{ at which the derivative } F'(x) \text{ exists.} \end{cases} \tag{I.4}$$

Now, consider a body Ω which, under abrupt or impulsive loading, will be broken into several fragments. We assume that all points in the body are accessible to fracture, which means that the fragmentation will be regarded as continuous. Under this assumption, the cumulative mass of fragments having a size less than or equal to s is assumed to be given by

$$M(s) = \int_\Omega \phi\left(s,\ s_m(\overrightarrow{x}),\ \alpha(\vec{x})\right) dm \tag{I.5}$$

where

- s_m : mean or average fragment size;
- α : shape factor;
- ϕ : cumulative mass density;
- dm : elementary mass.

The cumulative mass density varies as a function of position within the fragmented body because of spacial variations of the stresses causing fragmentation. In what follows, we will consider both the homogeneous and the heterogeneous cases.

I.3.2 Homogeneous fragmentation

Fragmentation in a body is regarded as homogeneous if the average size and the shape factor of fragments are the same at all points in that body:

$$\phi(s,\ s_m(\overrightarrow{x}),\ \alpha(\vec{x})) = \phi(s,\ s_m,\ \alpha) \qquad \forall \overrightarrow{x} \in \Omega \tag{I.6}$$

Therefore the cumulative mass becomes

$$M(s) = \int_\Omega \phi(s,\ s_m(\overrightarrow{x}),\ \alpha(\vec{x}))dm = \phi(s,\ s_m,\ \alpha) \int_\Omega dm \tag{I.7}$$

Hence, the cumulative passing of mass having a size less than or equal to s is

$$P(s) = \phi(s,\ s_m,\ \alpha) \tag{I.8}$$

In general, ϕ is determined by empirical means. Experimental results suggest that the mass distribution approximately satisfies the exponential law

$$p(m) = \frac{1}{m_0} e^{-(\frac{m}{m_0})} \tag{I.9}$$

where

- p : the probability density;
- m_0 : scale parameter, $m_0 > 0$.

Therefore, the cumulative mass density is

$$\int_0^m p(x)dx = 1 - e^{-(\frac{m}{m_0})} \tag{I.10}$$

Now, assuming that the mass of the fragment is related to its size as follows

$$\frac{m}{m_0} = \left(\frac{s}{s_0}\right)^\alpha \tag{I.11}$$

s_0 is a scale parameter which corresponds to m_0. $\alpha > 0$ is a shape factor which is equal to 3 for cubical or spherical fragments. Hence, the cumulative mass density of fragments having a size less than or equal to s is

$$1 - \exp\left[-\left(\frac{s}{s_0}\right)^\alpha\right] \tag{I.12}$$

Equation (I.12) is the well known two parameter Weibull distribution which can also be written as

$$\phi(s,\ s_m,\ \alpha) = 1 - \exp\left[-\ln(2)\left(\frac{s}{s_m}\right)^\alpha\right] \tag{I.13}$$

where s_m is the mean fragment size corresponding to a passing of 50% ($\phi(s_m,\ s_m,\ \alpha) = 1/2$). Using Eq. (I.13), we can, by curve fitting, find s_m and α for the limestone samples (Fig. I.5 [1]). The results of fitting show that we can obtain approximately the same shape factor but a different corresponding mean fragment size. These experiments demonstrate that, although we kept the same loading conditions and the same material, the fragmentation process changes with the size of the fragmented body. As a first conclusion, the dynamic fragmentation within a body is too complexer to be regarded as homogeneous.

[1] W.D.: Weibull Distribution

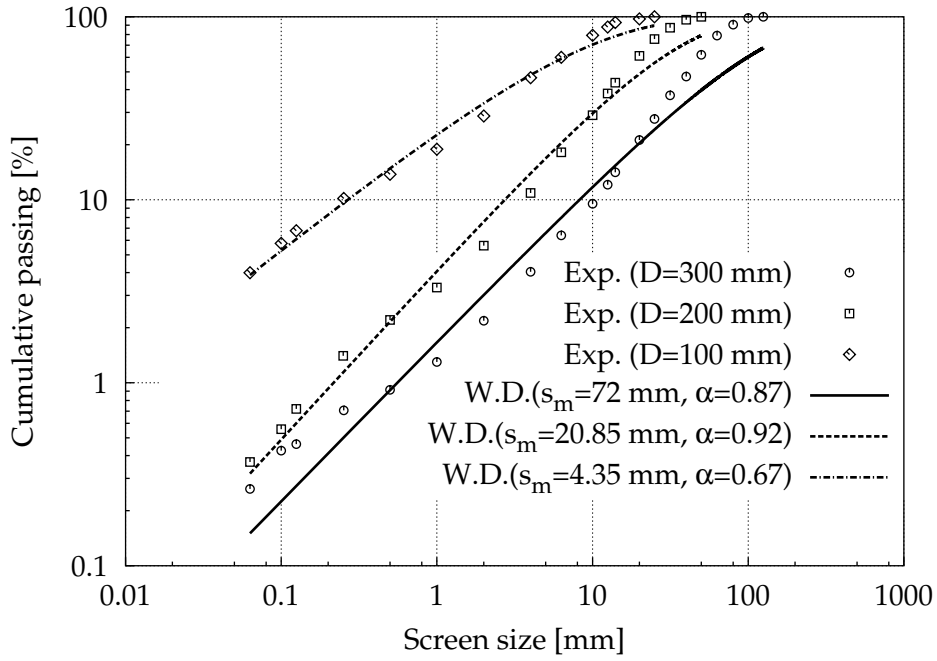

Figure I.5: Comparison of experimental and analytical distributions

I.3.3 Heterogeneous fragmentation

Fragmentation in a body is regarded as heterogeneous if the average size and the shape factor varie as a function of position within the fragmented body. Several blasting tests show us that the shape factor can be considered constant. Consequently, in what follows, only the mean fragment size will varie within the body.
In this work, attention is focused on the study of two different cumulative mass densities:

1. **Uniform cumulative mass density**

   The simplest assumption to make when determining fragment size distribution is to consider a uniform one. In this case, the cumulative mass can be given by the following equation:

   $$M(s) = \int_{\left\{\overrightarrow{x} \in \Omega,\ \ s_m(\overrightarrow{x}) < s\right\}} dm = \int_{\Omega} \mathscr{H}\left(s - s_m(\overrightarrow{x})\right) dm \tag{I.14}$$

   where $\mathscr{H}$ is the Heaviside function.

2. **Weibull cumulative mass density**

   As previously discussed, statistical considerations indicate that a distribution of fragment sizes should be determined around a mean fragment size. Using the function described by Eq. (I.13), the cumulative mass distribution of fragments having a size less than or equal to s is

   $$M(s) = \int_{\Omega} \left[1 - \exp\left[-\ln(2)\left(\frac{s}{s_m(\overrightarrow{x})}\right)^{\alpha}\right]\right] dm \tag{I.15}$$

I.3.4 Fragment size prediction in dynamic fragmentation

I.3.4.1 Experimental considerations

For an arbitrary body, $s_m(\overrightarrow{x})$ will be as complex as the complexity of the fragmentation event. In order to reduce the complexity of the problem we consider the above cylindrical samples. On the other hand, we assume that the explosive pressure in the drilled hole is uniformly distributed, so we can expect that the mean fragment size will be only function of the radius

$$s_m(\overrightarrow{x}) = s_m(r) \quad \forall\ r \in [r_i,\ \ r_e] \tag{I.16}$$

where r_i is the blasthole radius and r_e the sample radius. Finally, we assume that $s_m(r)$ is an increasing function. This assumption is widely accepted since the fracture process will be weakened when we move away from the explosive source.
Firstly, let us assume a uniform cumulative mass density. With these considerations, the cumulative mass distribution of fragments having a size less than or equal to $s = s_m(r)$ is

$$M(s_m(r)) = h \int_{r_i}^{r} \rho(x) 2\pi x dx \tag{I.17}$$

where ρ is the material density and h is the sample height. If we assume a uniform material density, we will have

$$M(s_m(r)) = \pi h \rho (r^2 - r_i^2) \tag{I.18}$$

Therefore, the cumulative passing of mass having a size less than or equal to s is

$$P(s_m(r)) = \frac{r^2 - r_i^2}{r_e^2 - r_i^2} \tag{I.19}$$

Hence, the function $s_m(r)$ may be given by

$$s_m(r) = P^{-1}\left(\frac{r^2 - r_i^2}{r_e^2 - r_i^2}\right) \tag{I.20}$$

Since experimental results give us the cumulative passing as a function of the fragment size, we can determine, by using (I.20), the mean fragment size as a function of the radius. Experimental results for the three considered samples are presented in Fig. I.6.

If we keep constant the blasthole radius (r_i), one can point out that with the assumption of a uniform cumulative mass density, the cumulative mass distribution of any sample having an outside radius r_e will be determined as follows

$$P(s_m(r)) = \frac{r_{ref}^2 - r_i^2}{r_e^2 - r_i^2} \times \frac{r^2 - r_i^2}{r_{ref}^2 - r_i^2} = \varpi P_{ref}(s_m(r)) \tag{I.21}$$

where P_{ref} is the cumulative passing of a blasted reference sample having an outside radius r_{ref}. Therefore, the case corresponding to $\varpi > 1$ can be interpreted in the following way: knowing only the fragmentation result of a sample with an outside radius r_{ref}, we can predict the fragmentation curve of any sample having an outside radius r_e such that $r_e \leq r_{ref}$. The predicted cumulative passing can be given by

$$P(s_m(r)) = \min\left(\varpi P_{ref}(s_m(r)),\ 1\right) \tag{I.22}$$

Fig. I.7 shows experimental and predicted results of the considered samples. Predicted results were based on the experimental fragmentation result of the biggest sample (300 mm in diameter). As can be seen, theoretical predictions are in good agreement with experiments.

However, the use of a uniform cumulative mass with the assumption of an increasing fragment size is in contradiction with experimental results obtained from the composite concrete cylinder which indicate that, at each position of the sample, one can expect a distribution in fragment sizes and shapes. In order to overcome this limitation, one possibility consists of using the Weibull cumulative mass density given by Eq. (I.13). In this case, the cumulative mass distribution of fragments having a size less than or equal to s will be defined as

$$M(s) = h \int_{r_i}^{r_e} \rho(x) \left[1 - \exp\left[-\ln(2) \left(\frac{s}{s_m(x)} \right)^{\alpha} \right] \right] 2\pi x dx \tag{I.23}$$

From Eq. I.23, it is difficult to obtain directly the mean fragment size as a radius function. Since we assume that $s_m(r)$ is an increasing function, we can suggest an analytical function with n adjustable parameters $s_m(r, \alpha_1, \alpha_2, .., \alpha_n)$ and try to find these parameters by curve fitting. Fig. I.8 shows $s_m(r)$ obtained by such a method for the three considered samples[2]. This figure shows that $s_m(r)$ of the biggest sample contains, approximately, the complete informations about the others. Thus, once again, we can predict the fragmentation curves of any sample having a diameter less than the biggest sample diameter. Fitted results for the biggest one and predicted curves for the two others are shown in Fig. I.9. This figure shows that analytical distributions are in good agreement with experiments.

However, in spite of the agreement between theoretical and experimental results, the above formulations are not complete because the evolution process that leads to catastrophic failure of the material was not considered. Furthermore, since the boundary conditions influence the fragmentation event, as was mentioned before, one can expect that, when using the present formulation which does not include such conditions, we are not able to predict the fragmentation result of the confined magnetite concrete. In order to overcome these limitations, we should introduce in our approach physical considerations of the breakage mechanisms which involve fractures governing laws. To convey ideas and assumptions clearly, in the following section, we propose to provide, by the analysis of the dynamic deformation problem, a rational basis for predicting the fragment size resulting from a fragmentation process.

[2]The suggested expression used for $s_m(r)$ is

$$s_m(r) = \alpha_1 + \alpha_2 r^{\alpha_3} + \alpha_4 e^{\alpha_5 r} \quad [\text{mm}]$$

for the considered tests, we obtain $(\alpha_1,\ \alpha_2,\ \alpha_3,\ \alpha_4,\ \alpha_5) = (-0.650,\ 0.0136,\ 1.760,\ -0.275,\ -7.553)$

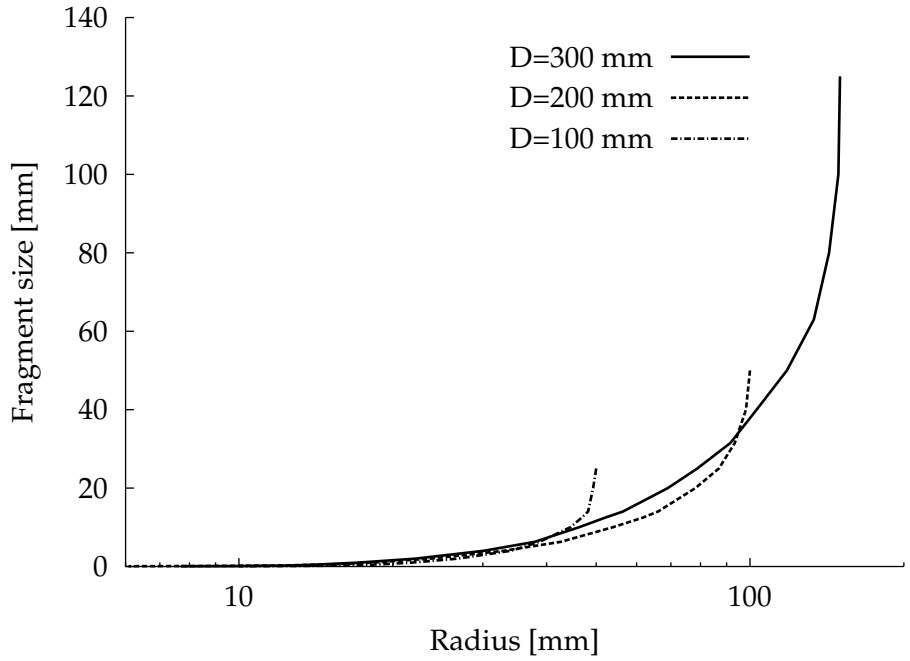

Figure I.6: Mean fragment size as a function of radius (uniform cumulative mass density)

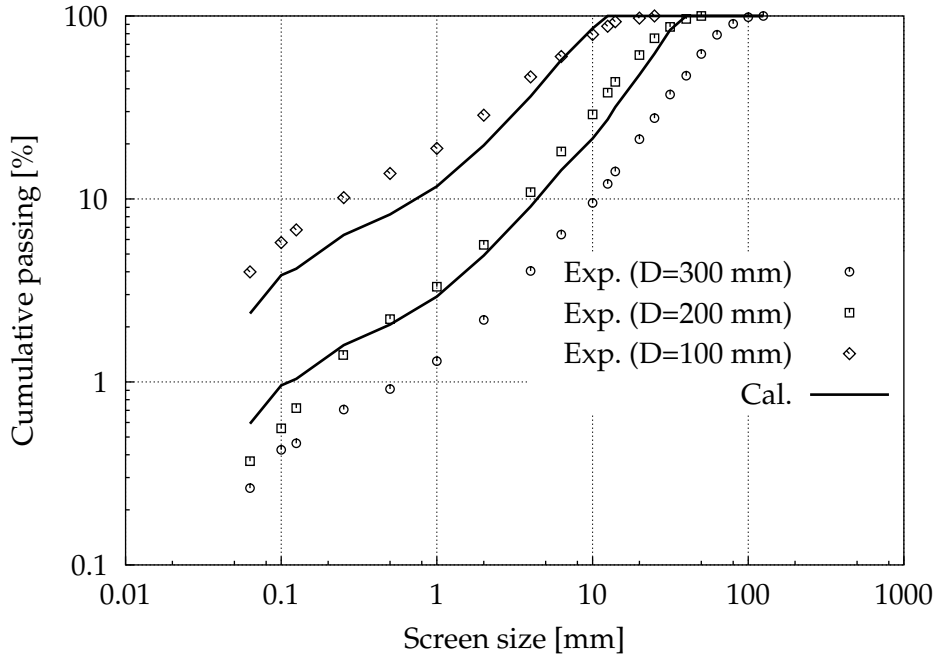

Figure I.7: Experimental and predicted distributions (uniform cumulative mass density)

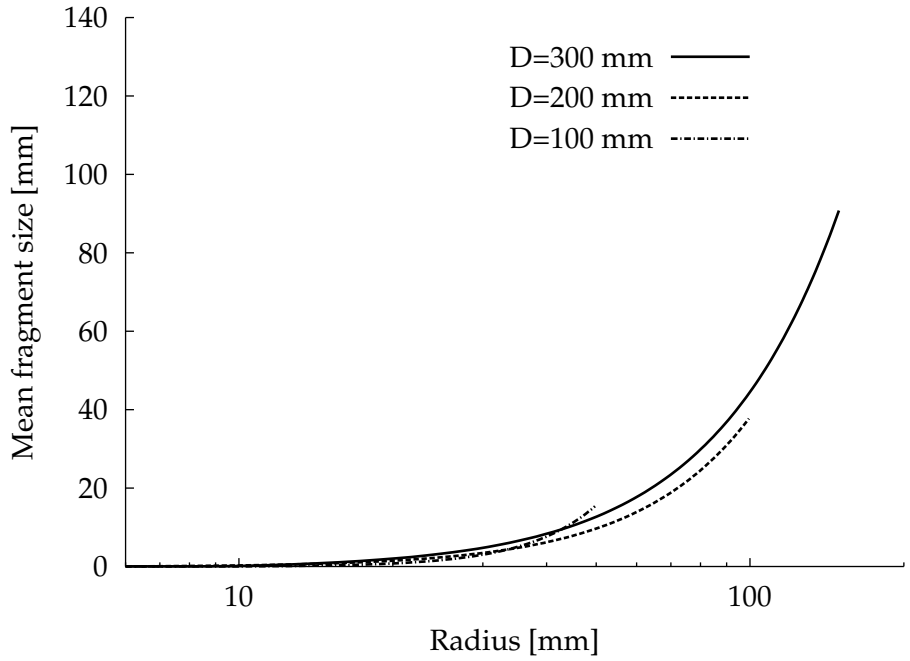

Figure I.8: Mean fragment size as a function of radius (Weibull cumulative mass density)

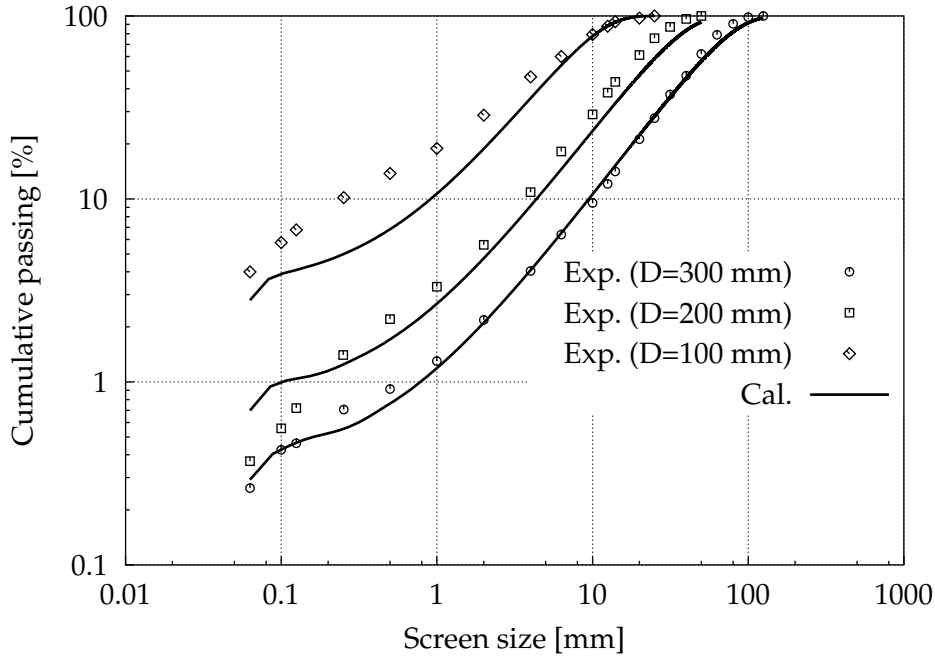

Figure I.9: Experimental and predicted distributions (Weibull cumulative mass density)

I.3.4.2 Physics-based modelling of dynamic fragmentation

Several models for dynamic fragmentation have been suggested in the past. To date, the most widely applied theoretical models of the process are those based on the pioneering studies of Grady (1982) and Glenn and Chundnovsky (1986). These models, based on energy balance principles, essentially assume that the energy available to form new fracture surfaces causes these to form instantaneously. Thus, these models are expected to be accurate at extremely high strain rates, when the time to fragmentation is extremely short.
Other studies are based on the incorporation of cohesive surfaces between standard elastic elements, to serve as prospective fracture paths in a dynamic simulation (Camacho and Ortiz, 1996; Espinosa et al, 1998). In what follows, the energy balance models are revisited. Then, one-dimensional version of the cohesive surface approach (Drugan 2001) is given. These models will be used to solve the following one-dimensional Initial Boundary-Value Problem. A bar of brittle elastic material with a uniform cross-sectional area A (Fig. I.10), occupying the region $-\frac{1}{2}L \leq x \leq \frac{1}{2}L,\ -\frac{1}{2}h \leq y \leq \frac{1}{2}h$, is permitted to deform only in the direction of the bar's axis. The bar has a mass density ρ, a Young's modulus E and a Poisson's ratio ν. In addition, we assume that there was some stress level, say σ_c, below which no cracks would grow for a given material.

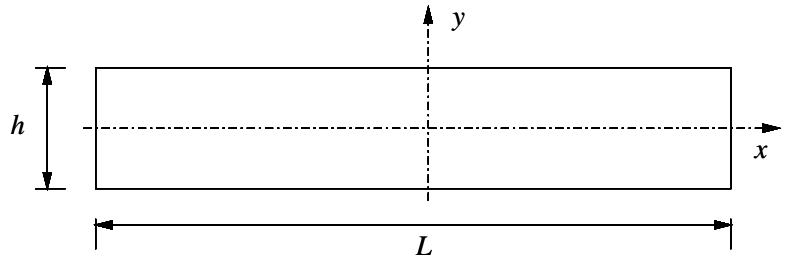

Figure I.10: Bar of brittle elastic material experiencing a uniform $x-$direction strain rate

The boundary conditions on this bar are

$$\begin{aligned} u_x\left(\pm\tfrac{1}{2}L,\ y,\ t\right) &= \pm\tfrac{1}{2}\dot{\epsilon}_0 Lt \qquad \forall (y,t) \in [-\tfrac{1}{2}h,\ \tfrac{1}{2}h] \times [0,\ T] \\ u_y\left(x,\ \pm\tfrac{1}{2}h,\ t\right) &= 0 \qquad\qquad \forall\ (x,t) \in [-\tfrac{1}{2}L,\ \tfrac{1}{2}L] \times [0,\ T] \end{aligned} \tag{I.24}$$

where u_x and u_y are x and y components of the displacement vector, $\dot{\epsilon}_0$ is a constant positive applied strain rate and $[0,\ T]$ is the time interval of interest.
The initial conditions, in accord with Grady assumption, are those of zero displacement and a uniform strain rate, which corresponds to a linear velocity distribution:

$$u(x,\ y,\ 0) = 0, \qquad \frac{\partial u}{\partial t}(x,\ y,\ 0) = \dot{\epsilon}_0 x \tag{I.25}$$

where $u = u_x$ is the only non zero displacement.

The energy balance concept

In the present approach we are not concerned with how or how fast a crack propagates, but only focus our attention on the resulting fragments.
Since the bar experiences a uniform constant strain rate, the axial stress will increase linearly until reaching σ_c. At this moment, we assume that the bar will be divided, instantaneously, into several fragments. It is assumed that the fractures at the ends of each fragment occur simultaneously. As a consequence, the change in forces at the ends of each fragment are equal but opposite and the net impulse delivered to the fragment during fracturing are zero.

The kinetic energy of an isolated fragment of length ℓ can be expressed as

$$\mathbf{E} = \frac{1}{2} A\rho \int_{-\ell/2}^{\ell/2} [v_0 + \dot{\epsilon}_0 x]^2 \, dx = \mathbf{E}_0 + \frac{1}{24} A\rho \dot{\epsilon}_0^2 \ell^3 \tag{I.26}$$

where v_0 is the velocity of the fragment mass center and $v_0 + \dot{\epsilon}_0 x \ \forall x \in [-\ell/2, \ \ell/2]$ is the velocity of material points at a distance x from the fragment center. $\mathbf{E}_0$ is the kinetic energy due to the translation of the fragment mass center.
Following Grady (1982), the principal source of energy available to drive the fractures is the kinetic energy, the effect of the stored elastic energy is neglected. Suppose that Γ_c is the average specific fracture energy for the material and that the area of each fracture surface is the cross-sectional area A. Then a fracture energy of $\frac{1}{2}\Gamma_c A$ is consumed at each end of the fragment from the energy supply within the fragment. In the original model of Grady (1982), a critical fragment size is estimated by the minimization of the energy $\bar{\mathbf{E}} + \Gamma_c$ with respect to the fracture surface area. Where $\bar{\mathbf{E}} = \mathbf{E} - \mathbf{E}_0$ is the energy consumed in the creation of new surfaces. For the present case, we consider the direct energy balance: the available kinetic energy $\bar{\mathbf{E}}$ is balanced against the energy associated with the new surface created in the process, then

$$\bar{\mathbf{E}} = \frac{1}{24} A\rho \dot{\epsilon}_0^2 \ell^3 = \Gamma_c A \tag{I.27}$$

Thus, an estimate of fragment size ℓ in terms of the initial state represented by $\dot{\epsilon}_0$ and the material parameters Γ_c and ρ is

$$\ell = \left(\frac{24\Gamma_c}{\rho \dot{\epsilon}_0^2} \right)^{1/3} \tag{I.28}$$

This model neglect the effect of the elastic stored energy, an omission that was later accounted for by Glenn and Chundnovsky (1986). The revised model predicted that the strain energy should dominate for quasi-brittle materials with low fracture toughness and high fracture-initiation stress. Moreover, for quasi-static loading, it is clear that fragmentation is controlled entirely by the balance between potential and surface energy, in accordance with the theory originally advanced by Griffith (1920).
When σ_c is reached, the elastic energy stored in a fragment is

$$\mathbf{P} = \frac{1}{2} \frac{\sigma_c^2}{\hat{E}} \ell A \ , \qquad \hat{E} = \frac{(1-\nu)E}{(1+\nu)(1-2\nu)} \tag{I.29}$$

In this case, The available energy to drive the fractures is the total energy $\bar{\mathbf{E}} + \mathbf{P}$, then the fragment size will verify the following cubical equation

$$\frac{1}{24} \rho \dot{\epsilon}_0^2 \ell^3 + \frac{1}{2} \frac{\sigma_c^2}{\hat{E}} \ell - \Gamma_c = 0 \tag{I.30}$$

The resolution of I.30 leads to a fragment size which is function of the strain rate and the material parameters (ρ, Γ_c, σ_c, $\hat{E}$).
It is important to note that in this approach we assume that the fragmentation process is instantaneous, it does not include the time dependence of the process. In reality, fragmentation occurs over finite time during which energy continues to be supplied to the system, and cracks nucleate and propagate throughout the body. Therefore, we propose, in the following section, a model that include the time history of the process.

The cohesive surface concept

In general, most rocks (limestone, granite, ...) and concrete, fracture in a quasi-brittle manner rather than exhibit yielding, but most metallic alloys fail by yielding and seldom by

cracking. This distinct difference leads to a distinct fracture process manner. In rocks and concrete the failure process can be divided into four stages, as illustrated in Fig. I.11 (Klein et al, 2001). The location of material at the four stages is indicated with markers in the figure. The four stages in Fig. I.11 are

1. The smooth field, or regular part, of the material response;
2. Initiation, or first appearance, of the localized deformation mode;
3. Evolution of the failure mode from the initiation to complete failure;
4. Complete failure and appearance of new surfaces.

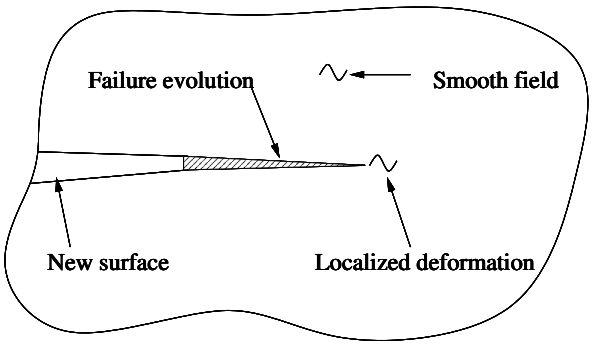

Figure I.11: A four-stage view of modelling failure

For each stage, a modelling approach must determine the constitutive laws governing the response of the material as well as the conditions that mark the transition to the next stage. One approach to model the above fracture process is the so-called **Cohesive zones approaches**. The cohesive approach to modelling fracture has recently become a very active area of research (Xu and Needleman, 1994; Camacho and Ortiz, 1996). The cohesive view of material is captured by surface constitutive relations that describe the evolution of traction generated across the faces of a crack as a function of the opening displacement. In what follows, we will use this approach in order to predict the minimum fragment size resulted from the fragmentation of the bar cited above. Following Drugan (2001), the key feature of the model is to analyse the time-varying dynamic deformation of a prospective brittle elastic fragment that is jointed by nonlinear cohesive zones to the rest of the body. We shall use the coordinate system centered in the fragment, as shown in Fig. I.12. This figure shows the prospective fragment, where δ_s is the displacement of the elastic segment end relative to its center, δ_c is the displacement of the half cohesive zone relative to the segment end, and $\delta = \delta_s + \delta_c$ is the total displacement.

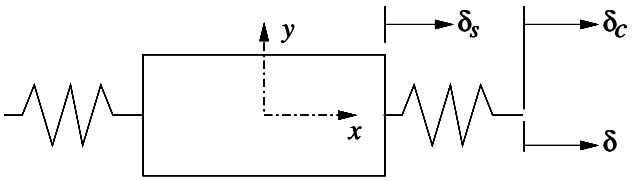

Figure I.12: A prospective fragment: elastic segment + two half cohesive zones

Our aim is to predict the minimum fragment size. To do that, we need the following developments. Let us consider the small displacements assumption. Since we permit only x-direction deformations, the only nontrivial equilibrium equation is then

$$\frac{\partial \sigma_{xx}}{\partial x} = \rho \frac{\partial^2 u}{\partial t^2} \tag{I.31}$$

where σ_{xx} is the x-direction component of the Cauchy stress tensor $\underline{\underline{\sigma}}$. For an homogeneous, isotropic linear elastic solid, the stress-displacement relation can be written as

$$\sigma_{xx} = \hat{E}\frac{\partial u}{\partial x} \tag{I.32}$$

Substituting Eq. (I.32) into (I.31), we obtain

$$\frac{\partial^2 u}{\partial t^2} - c^2\frac{\partial^2 u}{\partial x^2} = 0 \tag{I.33}$$

where $c = \sqrt{\hat{E}/\rho}$ is the elastic waves velocity.
Eq. (I.33) has to be resolved with the initial conditions and by enforcing the appropriate boundary conditions on the end of the elastic segment ($x = \ell/2$). These conditions are displacement and stress continuities with the cohesive surface.
The bar experiences a uniform constant strain rate $\dot{\epsilon}_{xx} = \dot{\epsilon}_0$ until fragmentation initiates. Therefore, since $\delta(0) = 0$, the total relative displacement δ can be shown to be

$$\delta(t) = \frac{1}{2}\dot{\epsilon}_0 \ell t \tag{I.34}$$

Using the definition of δ, continuity of displacement between the elastic segment and the cohesive zone requires

$$u\left(\frac{\ell}{2},\ t\right) = \delta_s(t) = \delta(t) - \delta_c(t) = \frac{1}{2}\dot{\epsilon}_0 \ell t - \delta_c(t) \tag{I.35}$$

The cohesive law is assumed to have a traction-crack opening displacement relation of the form

$$\mathrm{T}(2\delta_c) = \sigma_c \frac{2\delta_c}{\delta^\star}\exp\left(1 - \frac{2\delta_c}{\delta^\star}\right) \tag{I.36}$$

In this case, σ_c is the strength of the cohesive surface, which is attained when $2\delta_c = \delta^\star$. The cohesive crack model parameters can be related to the critical strain energy release rate (per unit surface) (Whittaker et al, 1992) as follows:

$$G_{IC} = \int_0^{+\infty} \mathrm{T}(2\delta_c) d(2\delta_c) \tag{I.37}$$

For plane strain linear elastic fracture mechanics, G_{IC} can be expressed as follows

$$G_{IC} = \frac{(1-\nu^2)K_{IC}^2}{E} \tag{I.38}$$

Using Eq. (I.36), (I.37) and (I.38), one can determine $\delta^\star$ as follows

$$\delta^\star = \frac{(1-\nu^2)K_{IC}^2}{\exp(1)E\sigma_c} \tag{I.39}$$

The stress continuity between the elastic segment and the cohesive zone requires

$$\hat{E}\frac{\partial u}{\partial x}(\frac{\ell}{2},\ t) = \mathrm{T}(2\delta_c(t)) \tag{I.40}$$

In order to calculate the minimum fragment size, Drugan assumes that the fragmentation initiation will occurs when the maximum stress level in the cohesive zone is reached. In terms of the cohesive zone displacement, this requires

$$2\delta_c(t_{cr}) = \delta^\star \tag{I.41}$$

where t_{cr} is the time corresponding to $\mathrm{T} = \sigma_c$. To carry this analysis further, Drugan makes an addition assumption. He supposes that the determination of the minimum fragment size ℓ_{min} requires that at time t_c, the prospective fragment has just stopped expanding, i.e. $\delta_s'(t_{cr}) = 0$. Thus, from Eq. (I.35), it follows that

$$\delta_c'(t_{cr}) = \frac{1}{2}\dot{\epsilon}_0 \ell_{min} \tag{I.42}$$

Analytical development of the defined Initial Boundary-Value Problem is given by Drugan (2001). The final result of this development is illustrated by the following system

$$\begin{cases} \tilde{\delta}_c^{(1)\prime}(\tilde{t}) + \tilde{\delta}_c^{(1)}(\tilde{t}) \exp\left[1 - \tilde{\delta}_c^{(1)}(\tilde{t})\right] = \tilde{\dot{\epsilon}}_0 \tilde{t}, \quad \tilde{\delta}_c^{(1)}(0) = 0, \qquad \text{for } 0 \leq \tilde{t} \leq \tilde{\ell}, \\ \tilde{\delta}_c^{(n+1)\prime}(\tilde{t}) + \tilde{\delta}_c^{(n+1)}(\tilde{t}) \exp\left[1 - \tilde{\delta}_c^{(n+1)}(\tilde{t})\right] = \tilde{\dot{\epsilon}}_0 \tilde{\ell} - \tilde{\delta}_c^{(n)\prime}(\tilde{t} - \tilde{\ell}) + \\ \tilde{\delta}_c^{(n)}(\tilde{t} - \tilde{\ell}) \exp\left[1 - \tilde{\delta}_c^{(n)}(\tilde{t} - \tilde{\ell})\right], \quad \tilde{\delta}_c^{(n+1)}(n\tilde{\ell}) = \tilde{\delta}_c^{(n)}(n\tilde{\ell}), \quad \text{for } n\tilde{\ell} \leq \tilde{t} \leq (n+1)\tilde{\ell} \end{cases} \tag{I.43}$$

where

$$\tau = \frac{\delta^\star \hat{E}}{2c\sigma_c}, \quad \tilde{t} = \frac{t}{\tau}, \quad \tilde{\delta}_c(\tilde{t}) = \frac{\delta_c(t)}{\delta^\star/2}, \quad \tilde{\dot{\epsilon}}_0 = \frac{\dot{\epsilon}_0 \tau}{\sigma_c/\hat{E}}, \quad \tilde{\ell} = \frac{\ell}{c\tau} \tag{I.44}$$

and n is the number of reflexions.
The above system is solved iteratively and ℓ_{min} is determined in such a way that Eq. (I.41) and Eq. (I.42) are simultaneously fulfilled.

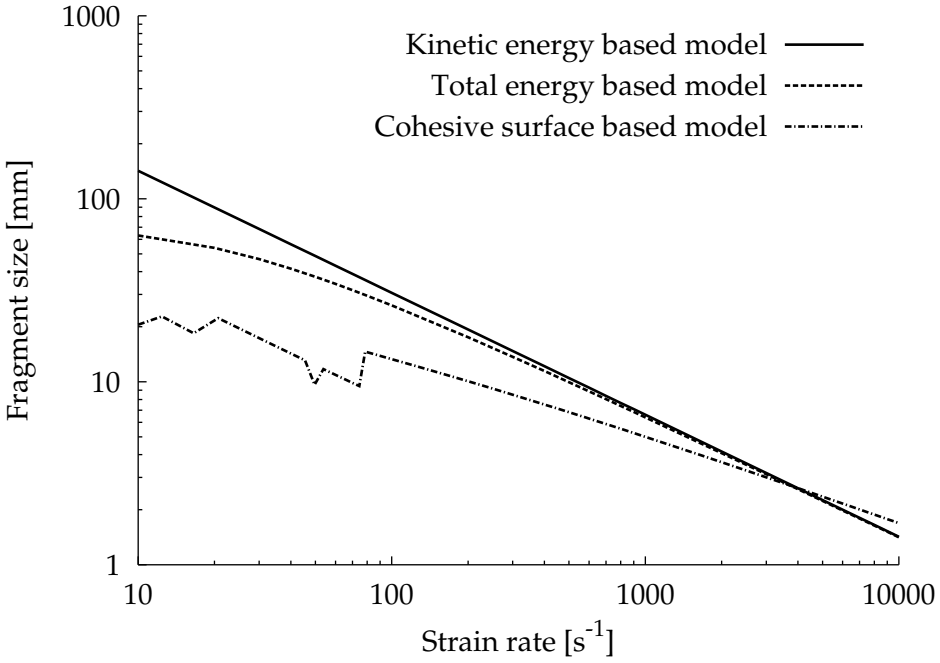

Figure I.13: Comparison of several model's predictions of fragment size versus applied strain rate (Material constants are: $E = 64$ GPa, $\nu = 0.2$, $\rho = 2200$ Kg/m^3, $K_{IC} = 1.3$ MPa$\sqrt{\mathrm{m}}$, $\sigma_c = 7$ MPa, $\Gamma_c = (1 - \nu^2)K_{IC}^2/E$)

Fig. I.13 compares the predictions, for a given brittle material, of the fragment size versus applied strain rate for the kinetic energy and the total energy (kinetic energy + stored strain energy) balance approachs, with those of the cohesive surface concept.
One very interesting feature of the results shown in this figure is the fact that the predictions of all models tend to "converge" at high strain rate. The kinetic energy model gives an upper limit which probably can be accurate at high strain rates, while the cohesive model gives a lower limit which probably can be accurate at lower strain rates.

This result is expected because Grady approach assumes that dynamic fragmentation is an instantaneous event, while Drugan approach accounts for the time-varying dynamic deformation that occurs prior to fragmentation onset.

I.3.5 General formulation

From the previous section, the main result that we should keep in mind is that one can predict the fragment size as a function of material properties and the applied strain rate. Now, the key feature to consider complex loadings and structures, is to assume that we can characterize the fragmentation event by the prediction of a mean fragment size s_m which can be related, at the **local level**, to a mechanical quantity G (strain rate, energy, ...). This relationship can be written formally as

$$s_m(\overrightarrow{x}) = \psi(G(\overrightarrow{x})) \quad \text{in } \Omega \tag{I.45}$$

where Ω is the considered body which is under impulsive loading. ψ is an **intrinsic** (only material dependent) scalar positive function which can be identified by considering special fragmentation tests. Concerning the mechanical quantity, it should be calculated by the resolution of the Initial Boundary-Value Problem. Therefore, if we assume that the shape factor is constant and that the fragmentation event of Ω is described by the Weibull distribution with parameters s_m and α, we can go up to the the cumulative mass of fragments by using Eq. (I.15) which can also be expressed as

$$M(s) = \int_{\Omega} \phi\left(s,\ \psi\left(G(\overrightarrow{x})\right),\ \alpha\right) \rho(\vec{x}) d\Omega \tag{I.46}$$

where $d\Omega$ is an elementary volume.
Since we deal only with dynamic fragmentation, it is essential to introduce a critical mechanical quantity G_c to distinguish between dynamic and static fragmentation. In fact, at very low rates of loading, most materials resist to fracture until a critical stress is reached. This is the static failure regime, in which fragmentation is dominated by the growth of a single weakest flaw. The dynamic regime is entered when growth of this flaw cannot relieve the applied loading, stresses rise in the adjacent material, and new flaws begin to nucleate and grow.
With this consideration, Eq. (I.46) becomes

$$M(s) = \int_{\Omega^\star} \phi\left(s,\ \psi\left(G(\overrightarrow{x})\right),\ \alpha\right) \rho(\vec{x}) d\Omega^\star \tag{I.47}$$

where $\Omega^\star$ is defined as

$$\Omega^\star = \{\overrightarrow{x} \in \Omega \ / \ G(\overrightarrow{x}) \geq G_c\} \tag{I.48}$$

Eq. (I.47) may also be rewritten as

$$M(s) = \int_{\Omega} \mathscr{H}\left(G(\overrightarrow{x}) - G_c\right) \phi\left(s,\ \psi\left(G(\overrightarrow{x})\right),\ \alpha\right) \rho(\vec{x}) d\Omega \tag{I.49}$$

where $\mathscr{H}$ is the Heaviside function.
The last thing that we want to introduce here is the concept of a minimum value of fragment size. Indeed, when the mechanical quantity becomes infinite, one can expect that a minimum non zero fragment size may exist, i.e.

$$\lim_{G \to +\infty} \psi(G) = s_{min} > 0 \tag{I.50}$$

In fact, since we note that the fragmentation of materials is the result of crack propagation, one can expect that any two cracks completely propagated must be at a distance greater than a certain value because of the unloading effect of release waves arising from crack nucleation. This fact shows that a minimum fragment size must exist. Obviously, this concept of minimum fragment size can be replaced by an irreducible material element when we deal with extensively crushing problem.

References

Camacho G.T., Ortiz M., 1996. *Computational modelling of impact damage in brittle materials.* Int. J. Solids Structures 33 (20-22), 2899-2938.

Curran D.R., Seaman L., Shockey D.A., 1987. *Dynamic failure of solids.* Physics Reports 147 (5 & 6), 253-388.

Digby P.J., Nilsson L., Oldenburg, M., 1985. *Finite elment simulation of the time dependent fracture and fragmentation processes in rock blasting.* Int. J. Num. Ana. Meth. Geomechanics 9, 317-329.

Dienes J.K., 1985. *A statistical theory of fragmentation processes.* Mech. Materials 325-335.

Donzé F.V., Bouchez J., Magnier S.A., 1997. *Modeling fractures in rock blasting.* Int. J. Rock Mech. Min. Sci. 34 (8), 1153-1163.

Drugan W.J., 2001. *Dynamic fragmentation of brittle materials: analytical mechanics-based models.* J. Mech. Phys. Solids 49, 1181,1208.

Espinosa H.D., Zavattieri P.D., Dwivedi S.K., 1998. *A finite deformation continuum/discrete model for the description of fragmentation and damage in brittle materials.* J. Mech. Phys. Solids 46 (10), 1909-1942.

Fourney W.L., Dick R.D., Wang X.J., Wei Y., 1993. *Fragmentation mechanism in crater blasting.* Int. J. Rock Mech. Min. Sci. & Geomech. Abstr. 30 (4), 413-429.

Glenn L.A., Chudnovsky A., 1986. *Strain-energy effects on dynamic fragmentation.* J. Appl. Phys. 59 (4).

Grady D.E., 1990. *Particle size statistics in dynamic fragmentation.* J. Appl. Phys. 68 (12).

Grady D.E., Kipp, M.E., 1987. *Dynamic rock fragmentation.* Fracture Mechanics of Rock by Academic Press Inc. (London).

Grady D.E., Kipp M.E., 1985. *Geometric statistics and dynamic fragmentation.* J. Appl. Phys. 58 (3).

Grady D.E., 1982. *Local inertial in dynamic fragmentation.* J. Appl. Phys. 53 (1).

Grady D.E., Kipp M.E., 1980. *Continuum modelling of explosive fracture in oil shale.* Int. J. Rock Mech. Min. Sci. & Geomech. Abstr. 17, 147-157.

Klein P.A., Foulk J.W., Chen E.P., Wimmer S.A., Gao H.J., 2001. *Physics-based modeling of brittle fracture: cohesive formulations and the application of meshfree methods.* Theo. Appl. Frac. Mechanis 37, 99-166.

Latham J.P., Munjiza A., Lu A., 1999. *Rock fragmentation by blasting - a literature study of research in the 1980's and 1990's.* FRAGBLAST-Int. J. Blas. Fragmentation 3, 193-212.

Melosh H.J., Ryan E.V., Asphaug E., 1992. *Dynamic fragmentation in impacts: Hydrocode simulation of laboratory impacts.* J. Geoph. research 97 (E9), 735-759.

Munjiza A., Latham J.P., Andrews K.R.F., 1999. *Challenges of a coupled combined finite-discrete element approach to explosive induced rock fragmentation.* FRAGBLAST-Int. J. Blas. Fragmentation 3, 237-250.

Munjiza A., Owen R.J., Bicanic N., 1995. *A combined finite-discrete element method in transient dynamics of fracturing solids.* Eng. computations 12, 145-174.

Ortiz R., 2000. *Mise au point d'une loi de comportement et de fragmentation dynamique du béton soumis à une énergie explosive.* Thèse de doctorat, Ecole des Mines de Paris, France.

Potyondy D.O., Cundall P.A., 1996. *Modeling of shock-and gas-driven fractures induced by a blast using bonded assemblies of spherical particles.* Rock Fragmentation by blasting. A.A. Balkema/Rotterdam, Brookfield.

Preece D., Thore B.J., Baer M.R., Swegle J.W., 1994. *Computer simulation of rock blasting: a summary of work from 1987 through 1993.* SAND29-1027, Unlimited Release.

Repetto E.A., Radovitzky R., Ortiz M., 2000. *Finite elment simulation of dynamic fracture and fragmentation of glass rods.* Comput. Methodes Appl. Mech. Engrg. 183, 3-14.

Seaman L., Curran D.R., Shockey D.A., 1976. *Computational models for ductile and brittle fracture.* J. Appl. Phys. 47 (11).

Whittaker B.N., Singh R.N., Sun G., 1992. *Rock Fracture Mechanics, Principles, Design and Applications.* Elsevier science publishers B.V.

Xu, X.P., Needleman, A., 1994. *Numerical simulations of fast crack growth in brittle solids.* J. Mech. and Phys. Solids 42, 1397-1434.

Yew C.H., Taylor P.A., 1994. *A thermodynamic theory of dynamic fragmentation.* Int. J. Impact Engng 15 (4), 385-394.

Chapter II

Constitutive modelling

Le processus de la fragmentation est une extension naturelle du processus de la rupture: un fragment est le résultat de l'intersection d'un certain nombre de fissures. Par conséquent, pour comprendre la fragmentation, on doit, tout d'abord, comprendre les critères qui conditionnent l'apparition des fissures et la cinétique par laquelle ces dernières passent.
Depuis une trentaine d'années, à partir des travaux pionniers de Griffith et Irwin, la Mécanique de la Rupture a connu un développement important. Les mécanismes de rupture ont été bien compris et bien modélisés en rupture fragile dans le cas d'un milieu contenant initialement une seule fissure macroscopique susceptible de se propager suite à des chargements extérieurs. Dans le cas d'un grand nombre de fissures, cette approche a montré ses limites et se trouve incapable de traiter un problème de fragmentation d'un milieu initialement intact. Pour combler cette limitation, plusieurs autres approches mathématiques ont été développées (micro-statistiques, phénoménologiques, ... etc).
Dans ce chapitre, il s'agit pas d'analyser toutes ces approches mais plutôt de présenter notre propre modèle.
Notre approche, basée sur la thermodynamique des milieux continus, a pour objectif de reproduire le comportement macroscopique des matériaux quasi-fragiles de type roches et béton, et ce pour différents types de sollicitations. Pour cette raison, le présent chapitre sera organisé de la manière suivante: dans un premier temps, nous présentons le cadre général de notre modélisation et quelques éléments de base de la thermodynamique des milieux continus. Deuxièmement, nous décrivons les observations expérimentales faites sur des éléments représentatifs afin d'identifier qualitativement le comportement des matériaux quasi-fragiles. Ensuite, nous présentons l'ensemble du modèle développé et les éléments de base de son implémentation numérique. Enfin, nous présentons une discussion sur le phénomène de localisation en rupture dynamique et un exemple 1D est donné comme illustration de ce problème.

II.1 Introduction

The fragmentation process is a natural extension of the fracture process: a fragment is produced by the intersection of a number of cracks, each crack forming surfaces on two adjacent fragments. Therefore, to understand fragmentation one must firstly understand both the threshold conditions that trigger the fracture process and the kinetics by which it proceeds. The response of a single crack to both static and dynamic loadings has received considerable attention over the past several decades and it is reasonably well understood. The first and hitherto the most successful approach dealing with fracture is that pioneered by Griffith and Irwin, in which a macroscopic crack is treated as a stress-free boundary in a boundary value problem. The threshold condition for crack instability is assumed to be a critical energy density, stress intensity factor, or other measure of the stress and strain fields near the crack tip. This approach, termed fracture mechanics, has been extremely successful in cases where the behaviour of a single, large crack in brittle material is of prime interest.
However, the response of a system of cracks under stress-wave loading is less well understood: treatment of each crack individually becomes forbidding. For such cases other mathematical approaches have been developed, among them one can find the micro-statistical fracture

mechanics. In this approach the micro-crack and micro-void concentration as well as orientation and size distributions are specified in the description of the material's thermodynamic state. They are considered as internal variables in the constitutive relations for the material. Difficulties related to accurate data for the formulation of evolution laws of such internal variables makes this approach unrealized especially for rock materials. Other approaches, based on continuum phenomenological models, are used extensively in sophisticated design computer codes to model quasi-brittle phenomena. It is outside the scope of this chapter to discuss all the models available in literature.
In this work, our main objective is to develop a macroscopic constitutive model for analyzing deformation and failure of quasi-brittle materials including load-induced anisotropy due to cracking. The developed constitutive relations will be able to reproduce the macroscopic stress-strain relations for different loading conditions, neglecting the microscopic mechanism of the behaviour. Time-dependence is also taken into account in our model. In fact, from a physical point of view, time-dependence arises naturally from the finite propagation velocity of cracks. If loading of a quasi-brittle material is imposed at a relatively slow rate then a single crack or a small number of cracks, which relieve the stresses induced by the applied loading, is formed leading to catastrophic failure before the growth of any other potential fracture site is activated. On the other hand, if a body of quasi-brittle material is subjected to high rate of deformation, large stresses are achieved in a relatively short time, then a higher density of fractures can be activated and can grow to a significant size without arresting each other. Such processes can be the origin of the apparent increase of the fracture resistance. This is why the fracture process is often viewed as rate dependent on the macroscopic scale. In our work, the rate dependence is exhibited through an overstress approach.
The remainder of this chapter is organized in the following way. In section II.2 we review the basic formulation of the Initial Boundary-Value Problem and we give the thermodynamic restrictions to be considered during the development of the constitutive equations. Section II.3 describes some typical experimental results characterizing the static and the dynamic behaviour of quasi-brittle materials. In section II.4 we present the developed constitutive model. Section II.5 deals with basic principles of the numerical implementation and some uniaxial computational results. Finally, in section II.6 we discuss the localization problem in dynamic fracture and a one-dimensional example is treated as illustration of this problem.

Notation

Throughout this chapter, the number of underlines beneath a symbol indicates the tensorial order of that variable. Superscript ^{t} indicates the transpose operation, while "tr" is the trace operator. Symbol ' : ' denote the inner product with double contraction, e.g. $\underline{\sigma} : \underline{\epsilon} = \sigma_{ij}\epsilon_{ji}$, $(\underline{\underline{\underline{\underline{\mathrm{H}}}}} : \epsilon)_{ij} = \mathrm{H}_{ijkl}\epsilon_{lk}$ where indexes denote cartesian components and repeated indexes imply summation unless otherwise indicated. Symbol ' . ' denote the outer product with single contraction, e.g. $(\underline{\sigma} \,.\, \underline{\epsilon})_{ij} = \sigma_{ik}\epsilon_{kj}$. The dyadic or tensor product is indicated with ' $\otimes$ ', e.g. $(\underline{\sigma} \otimes \underline{\epsilon})_{ijkl} = \sigma_{ij}\epsilon_{kl}$, whereas ' $\overline{\otimes}$ ' denotes the symmetrized dyadic product defined as $\underline{\underline{\mathrm{A}}} \,\overline{\otimes}\, \underline{\underline{\mathrm{B}}} : \underline{\underline{\mathrm{C}}} = \underline{\underline{\mathrm{A}}}.\underline{\underline{\mathrm{C}}}^s.\underline{\underline{\mathrm{B}}}$, for any arbitrary second-order tensors $\underline{\underline{\mathrm{A}}}$, $\underline{\underline{\mathrm{B}}}$, $\underline{\underline{\mathrm{C}}}$, where $\underline{\underline{\mathrm{C}}}^s = (\underline{\underline{\mathrm{C}}} + \underline{\underline{\mathrm{C}}}^t)/2$ is the symmetric part of $\underline{\underline{\mathrm{C}}}$. $\underline{\mathrm{I}}$ and $\underline{\underline{\underline{\underline{\mathrm{I}}}}}^s$ are respectively the second-order and symmetric fourth-order identity tensors.

II.2 Continuum problem formulation

Let us consider a continuous body $\Omega \subset \mathbb{R}^3$ undergoing a deformation process whose events are ordered by a scalar parameter t that will be referred as *time*. The reference configuration is denoted by Ω_0 and $\partial\Omega_0$ denotes the boundary of Ω_0. Points in Ω_0 are labeled by

their position vectors $\overrightarrow{X}$ relative to some origin. Let $[0,\ T] \subset \mathbb{R}_+$ be the time interval of interest. At each instant $t \in [0,\ T]$ the body occupies a new configuration, denoted $\Omega_t \subset \mathbb{R}^3$, with boundary $\partial\Omega_t$. This is the current or deformed configuration of the body. Let $\chi(\overrightarrow{X},\ t) : \Omega_0 \times [0,\ T] \longmapsto \Omega_t$ be the non-linear map of material points $\overrightarrow{X} \in \Omega_0$ onto spatial points $\overrightarrow{x} = \chi(\overrightarrow{X},\ t) \in \Omega_t$.

In what follows we shall be exclusively concerned with small transformations for which the gradient of the displacement field $\overrightarrow{u}(\overrightarrow{X},\ t) : \Omega_0 \times [0,\ T] \longmapsto \Omega_t$ remain small. For the sake of simplicity, let denote Ω as the reference configuration of our body.
The small strain tensor is defined as $\underline{\underline{\epsilon}} = \underline{\underline{\nabla}}^s(\overrightarrow{u})$, where ∇^s is the symmetric part of the gradient operator. We denote the stress tensor by $\underline{\underline{\sigma}} = \sigma_{ij}\overrightarrow{e_i} \otimes \overrightarrow{e_j}$, where $\sigma_{ij} \in \mathbb{R}$ denotes the component of $\underline{\underline{\sigma}}$ relative to the standard basis $(\overrightarrow{e_1},\ \overrightarrow{e_2},\ \overrightarrow{e_3})$ of $\mathbb{R}^3$. Second-order symmetric tensors are linear transformations in $\mathbf{S}$, defined as

$$\mathbf{S} := \left\{ \underline{\underline{x}} :\ \mathbb{R}^3 \longmapsto \mathbb{R}^3 \mid \underline{\underline{x}} \text{ is linear, and } \underline{\underline{x}} = \underline{\underline{x}}^t \right\} \tag{II.1}$$

In what follows, we assume that $\overline{\partial\Omega} = \overline{\partial_u\Omega \cup \partial_\sigma\Omega}$ and $\partial_u\Omega \cap \partial_\sigma\Omega = \emptyset$, where $\partial_u\Omega$ is the part of $\partial\Omega$ where displacements are prescribed as

$$\overrightarrow{u}|_{\partial_u\Omega} = \overrightarrow{u}_g(\text{given}) \tag{II.2}$$

whereas $\partial_\sigma\Omega$ is the part of $\partial\Omega$ where forces are prescribed as

$$\underline{\underline{\sigma}}|_{\partial_\sigma\Omega}.\overrightarrow{n} = \overrightarrow{\mathrm{T}}_g(\text{given}) \tag{II.3}$$

Here $\overrightarrow{n}$ is the vector normal to $\partial_\sigma\Omega$.
Let $\overrightarrow{f}(\overrightarrow{x},\ t)$ be the body force par unit of mass, a given vector field, and denote the mass density by $\rho(\overrightarrow{x},\ t)$. The local forms of the momentum equations are

$$\left.\begin{array}{l} \overrightarrow{\mathrm{div}}\underline{\underline{\sigma}} + \rho\overrightarrow{f} = \rho\frac{\partial^2\overrightarrow{u}}{\partial t^2} \\ \underline{\underline{\sigma}} = \underline{\underline{\sigma}}^t \end{array}\right\} \text{ in } \Omega \times [0,\ T] \tag{II.4}$$

This system of partial differential equations is supplemented by the boundary conditions, specified by (II.2) and (II.3), and the initial data

$$\left.\begin{array}{l} \overrightarrow{u}(\overrightarrow{x},\ 0) = \overrightarrow{u}_0(\overrightarrow{x}) \\ \frac{\partial\overrightarrow{u}}{\partial t}(\overrightarrow{x},\ 0) = \overrightarrow{v}_0(\overrightarrow{x}) \end{array}\right\} \text{ in } \Omega \tag{II.5}$$

where $\overrightarrow{u}_0$ and $\overrightarrow{v}_0$ are prescribed functions in Ω. Equations (II.4) and (II.5), together with the boundary conditions (II.2) and (II.3), yield an Initial Boundary-Valued Problem for the displacement field $\overrightarrow{u}(\overrightarrow{x},\ t)$, when the stress field $\underline{\underline{\sigma}}(\overrightarrow{x},\ t)$ is related to the displacement field $\overrightarrow{u}$ through a **constitutive equation**.

II.2.1 Constitutive equations: Thermodynamic approach

According to the principles of **determinism** and **local action**, the most general expression for the constitutive equation of an homogeneous **simple** material can be given by:

$$\underline{\underline{\sigma}}(\overrightarrow{x},\ t) = \mathscr{F}_{\tau \le t}\left[\underline{\underline{\nabla}}\overrightarrow{\chi}\left(\overrightarrow{X},\ \tau\right),\ \mathbf{T}\left(\overrightarrow{X},\ \tau\right)\right] \tag{II.6}$$

where $\mathscr{F}$ is a **functional** of the history up to time t of the deformation gradient associated with the motion $\overrightarrow{x} = \overrightarrow{\chi}(\overrightarrow{X},\ t)$ carrying the material point $\overrightarrow{X}$ in the reference configuration

to its position $\overrightarrow{x}$ in the current configuration at time t and $\mathbf{T}$ is the absolute temperature. Eq. (II.6) essentially states that the stress tensor $\underline{\underline{\sigma}}$ is a function of the entire deformation history, i.e., that the knowledge of the state of strain at a given time t is in general not sufficient to determine the stress state.
However, working with such a functional poses formidable experimental problems, even in the simplest cases. An alternative strategy, which overcomes this difficulty and is commonly adopted to formulate constitutive equations, is the method of **local state**.

The method of local state postulates that the thermodynamic state of a continuum at a given point and instant is completely defined by several **state variables** (also known as thermodynamic or independent variables). The time derivatives of those variables are not involved is the definition of the state, this postulate implies that any evolution can be considered as a succession of equilibrium states (therefore ultra rapid phenomena are excluded). They should result from observations at a micro-scale and from a homogenization process. The number of the state variables is determined by the number of phenomena taken into consideration. They can be observable (i.e. which can be measured in an experiment) or internal (or hidden). For plastic and viscoplastic material behaviour, the hypothesis of small transformations allows to additively split the total strain into the elastic and inelastic parts, respectively denoted by $\underline{\underline{\epsilon}}^e$ and $\underline{\underline{\epsilon}}^{in}$:

$$\underline{\underline{\epsilon}} = \underline{\underline{\epsilon}}^e + \underline{\underline{\epsilon}}^{in} \tag{II.7}$$

Thus, two state variables, related by the above decomposition equation, are identified. Other phenomena, such as softening, damage and fracture, call for the introduction of additional internal variables which will complete the description of the thermodynamic internal state of the continuum.
Finally, in order to establish a thermodynamic admissible process, the **Clausius-Duhem inequality** must be fulfilled.

II.2.2 Clausius-Duhem inequality

II.2.2.1 Energy balance law

The energy equation (first law of thermodynamics) states that the energy is conserved, which for a part Π of Ω with boundary $\partial\Pi$ at the time t, can be written as

$$\dot{\mathrm{E}}(\Pi) + \dot{\mathrm{K}}(\Pi) = \mathrm{P}(\Pi) + \mathrm{Q}(\Pi) \tag{II.8}$$

with

$$\mathrm{E}(\Pi) := \int_\Pi \rho e d\Pi, \qquad \mathrm{K}(\Pi) = \frac{1}{2}\int_\Pi \rho \dot{\overrightarrow{u}}.\dot{\overrightarrow{u}} d\Pi \tag{II.9}$$

$$\mathrm{P}(\Pi) = \int_\Pi \rho \overrightarrow{f}.\dot{\overrightarrow{u}} d\Pi + \int_{\partial\Pi} (\underline{\underline{\sigma}}.\overrightarrow{n}).\dot{\overrightarrow{u}} d(\partial\Pi) \tag{II.10}$$

$$\mathrm{Q}(\Pi) = \int_\Pi r d\Pi - \int_{\partial\Pi} \overrightarrow{q}.\overrightarrow{n} d(\partial\Pi) \tag{II.11}$$

Here, a dot denotes the rate with respect to time. E and K are the internal and the kinetic energy, respectively, of the part Π at the time t. Whereas P and Q represent mechanical and thermal power supply. Moreover, e is the specific internal energy (energy per unit mass), r is a volumetric heat source, $\overrightarrow{q}$ is the heat flux and $\overrightarrow{n}$ is the normal on $\partial\Pi$. Since (II.8) must hold for any arbitrary chosen part Π of Ω and using the equilibrium equation, one can easily obtain the local form of the first law of thermodynamics called also energy balance law:

$$\rho\dot{e} = \underline{\underline{\sigma}} : \dot{\underline{\underline{\epsilon}}} + r - \mathrm{div}(\overrightarrow{q}) \quad \text{in } \Omega \times [0,\ T] \tag{II.12}$$

II.2.2.2 Entropy inequality

The entropy inequality (second law of thermodynamics) states that the entropy (disorder) of a thermodynamic system can not decrease. This law can be stated as:

$$\dot{\mathrm{S}}(\Pi) - \Gamma(\Pi) \geq 0 \tag{II.13}$$

with

$$\mathrm{S}(\Pi) := \int_{\Pi} \rho s d\Pi, \qquad \Gamma(\Pi) = \int_{\Pi} \frac{r}{\mathbf{T}} d\Pi - \int_{\partial\Pi} \frac{\overrightarrow{q}.\overrightarrow{n}}{\mathbf{T}} d(\partial\Pi) \tag{II.14}$$

Here, S is the entropy of the part Π at the time t, s is the specific entropy, whereas Γ is the "entropy flux". Since (II.13) must hold for any arbitrary chosen part Π of Ω, one can easily obtain the local form of the second law of thermodynamics:

$$\rho\dot{s} - \frac{r}{\mathbf{T}} + \mathrm{div}\left(\frac{\overrightarrow{q}}{\mathbf{T}}\right) \geq 0 \quad \text{in } \Omega \times [0,\ T] \tag{II.15}$$

II.2.2.3 Clausius-Duhem inequality

We introduce the Helmholtz specific free energy function ψ:

$$\psi = e - \mathbf{T}s \tag{II.16}$$

Combining Eq. (II.12) and (II.15), one can obtain the inequality:

$$\underline{\underline{\sigma}} : \underline{\underline{\dot{\epsilon}}} - \rho\left(\dot{\psi} + s\dot{\mathbf{T}}\right) - \frac{\overrightarrow{q}}{\mathbf{T}}.\overrightarrow{\nabla}(\mathbf{T}) \geq 0 \quad \text{in } \Omega \times [0,\ T] \tag{II.17}$$

This is the Clausius-Duhem inequality, which corresponds to the positiveness of the dissipated energy and which has to be fulfilled by any model for all possible evolutions.

II.2.2.4 State potential, state laws

The state potential allows for the derivation of the state laws and the definition of the associate variables or driving forces associated with the state variables to define the energy involved in each phenomenon. In this study we choose the Helmholtz specific free energy function as the state potential. Irreversible changes of internal structures can be described by a set of internal state variables:

$$\{\boldsymbol{\xi}_k;\ k = 1,\ 2,\ ...\} \tag{II.18}$$

where $\boldsymbol{\xi}_k$ may be scalars, vectors, or higher order tensors. Among such internal variables one can find the inelastic strain tensor $\underline{\underline{\epsilon}}^{in}$. In this case, ψ, which depends on the observable and the internal variables, can be written formally as

$$\psi = \psi\left(\underline{\underline{\epsilon}},\ \mathbf{T},\ \boldsymbol{\xi}_k\right) \tag{II.19}$$

By differentiating Eq. (II.19) with respect to time and substituting the resulting expression into Eq. (II.17), the Clausius-Duhem inequality becomes

$$\left(\underline{\underline{\sigma}} - \rho\frac{\partial\psi}{\partial\underline{\underline{\epsilon}}}\right) : \underline{\underline{\dot{\epsilon}}} - \rho\left(s + \frac{\partial\psi}{\partial\mathbf{T}}\right)\dot{\mathbf{T}} - \rho\frac{\partial\psi}{\partial\boldsymbol{\xi}_k}\dot{\boldsymbol{\xi}}_k - \frac{\overrightarrow{q}}{\mathbf{T}}.\overrightarrow{\nabla}(\mathbf{T}) \geq 0 \quad \text{in } \Omega \times [0,\ T] \tag{II.20}$$

Thermoelasticity state laws are derived from this inequality which must be fulfilled for any state $\left(\underline{\underline{\epsilon}},\ \mathbf{T},\ \boldsymbol{\xi}_k\right)$ and any rates of the observable variables $\underline{\underline{\epsilon}}$ and $\mathbf{T}$.

$$\underline{\underline{\sigma}} = \rho \frac{\partial \psi}{\partial \underline{\underline{\epsilon}}} \tag{II.21}$$

$$s = -\frac{\partial \psi}{\partial \mathbf{T}} \tag{II.22}$$

Therefore, Clausius-Duhem inequality becomes

$$-\rho \frac{\partial \psi}{\partial \boldsymbol{\xi}_k} \dot{\boldsymbol{\xi}}_k - \frac{\overrightarrow{q}}{\mathbf{T}} . \overrightarrow{\nabla}(\mathbf{T}) \geq 0 \quad \text{in } \Omega \times [0,\ T] \tag{II.23}$$

This inequality define the volumetric dissipation which is the sum of an intrinsic dissipation (or mechanical dissipation) and a thermal dissipation due to heat conduction.
Finally, for the establishment of the inelastic strain and the internal variables evolution laws, the only restriction that must be fulfilled is the dissipation inequality given by (II.23).

II.3 Experimental characterization

The predictive capability of any mathematical constitutive relationship formulated to describe rocks and concrete behaviour during deformation depends critically on the data on which it is based. However, designing and performing a sequence of experiments, which will provide such useful constitutive data, is not a trivial task.
From the mathematical point of view, strains and stresses are defined in a material point, but the real materials are not continuous. Physically, strains and stresses represent averages on a fictitious volume element called the representative volume element (RVE). To give a subjective order of magnitude of a characteristic length, it can be equal to 100 mm for concrete and rocks. Thus, our discussion will be restricted to the stress-strain behaviour of a representative volume element.
Concrete and rocks exhibit non-linear behaviour in tension and compression. The response prior to the attainment of the material's ultimate strength is similar to that of any moderately strain hardening metals. However, the response past the ultimate strength is characterized by increased deformation with decreasing stress as a result of localization of damage (strain localization). Such materials may therefore be regarded as quasi-brittle. The non-linear response is a result of the nucleation, growth and coalescence of microscopic flaws.

II.3.1 Non-linear stress-strain behaviour

Concrete and rocks contain defects, such as pores and cracks even in the virgin state. These defects reduce their resistance capacity even under compression. The dominant failure mode of these materials under compression is the formation of shear bands. Its characteristic feature is shear displacement along the surface of fracture. A typical stress-strain curve in a uniaxial compression test is shown in Fig. II.1. As can be seen, past the elastic stage, the material exhibit moderate strain hardening prior to the attainment of the ultimate capacity. However, the response past the ultimate strength is characterized by an increase in deformation with decreasing stress. Such a response is called softening. Under uniaxial tension, another type of fracture occurs. Its characteristic is a clean separation with no shear offset between the surfaces.
Therefore, for model development, behaviour of quasi-brittle materials may be simplified

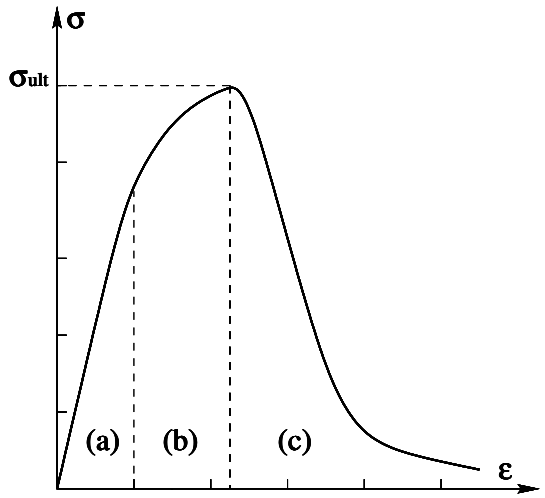

Figure II.1: Typical uniaxial loading stress-strain curve of a quasi-brittle material showing (a) the elastic zone, (b) the pre-peak non-linear zone and (c) the post-peak softening zone

into three levels of response: the linear elastic stage, the inelastic stage, and the softening stage. It should be emphasized that, in the last few years, researchers have started to realize that the softening in quasi-brittle materials and the associated localization of deformations cannot be regarded as a pure material property, but rather represents the response of the structure formed by the specimen together with its complete loading system. This argument can be supported by compression tests of specimens with different heights. In literature, one can find tests done by Van Mier (1984) on cylindrical cross section specimens and other done by Rokugo and Koyanagi (1992) on square cross section ones. The tests results in terms of stress and strain are shown in Fig. II.2. As can be seen, the descending branches of stress-

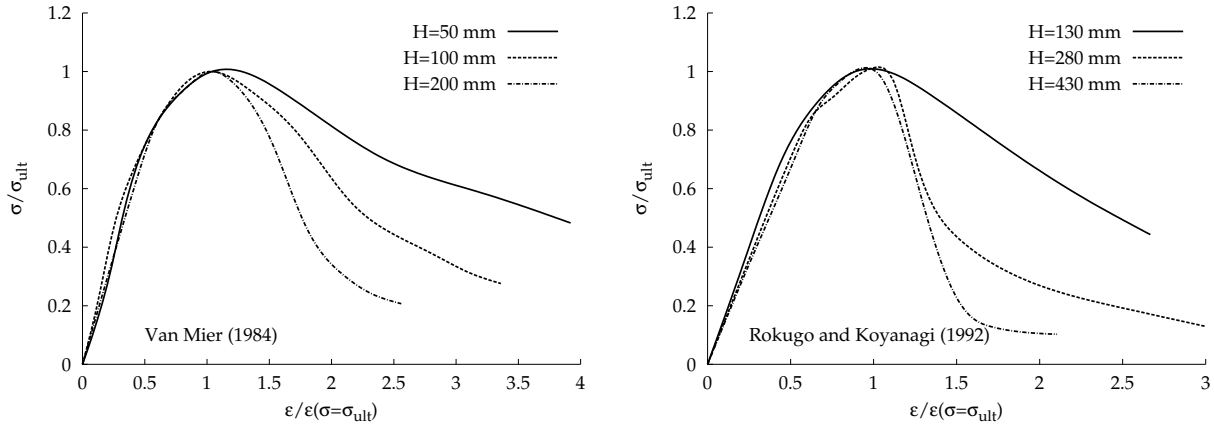

Figure II.2: Influence of specimen height on uniaxial stress-strain curve (after Van Mier, 1984; Rokugo and Koyanagi, 1992)

strain curves are not identical but have slopes decreasing with increasing specimen heights. Therefore, this specimen size dependance, can lead to conclude that the stress-strain curve of the considered material does not reflect a material property, but it has to be referred to as a structural property.

II.3.2 Factors affecting rock strength

Two of the most important factors influencing the behaviour of rocks and concrete are confining pressure and strain-rate.

II.3.2.1 Confining pressure effect

A basic principle of the laboratory testing of rock to obtain data for use in design analyses, is that the boundary conditions applied to the test specimen should simulate those imposed on the rock element in situ. This can rarely be achieved. General practice is to study the behaviour of the rock under known uniform applied stress systems. An important feature of the concrete material behaviour in triaxial compression is illustrated by Fig. II.3. These, and similar data for rocks, show that, with increasing confining pressure, the peak strength increases and there is a transition from brittle to fully ductile behaviour. The confining pressure at which the post-peak reduction in strength disappears and the behaviour becomes fully ductile is known as the brittle-ductile transition pressure (Brady and Brown, 1999). The overall strengthening effect can be represented in a $(\sigma_1 - \sigma_3)$-σ_1 diagram such as Fig. II.4 for amphibolite and sandstone meterials.

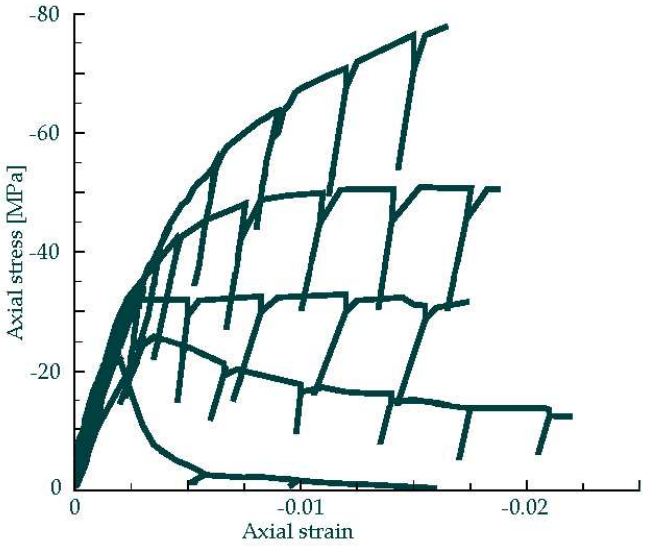

Figure II.3: Triaxial compression tests with increasing confining pressure on concrete material (after Pivonka et al, 2000)

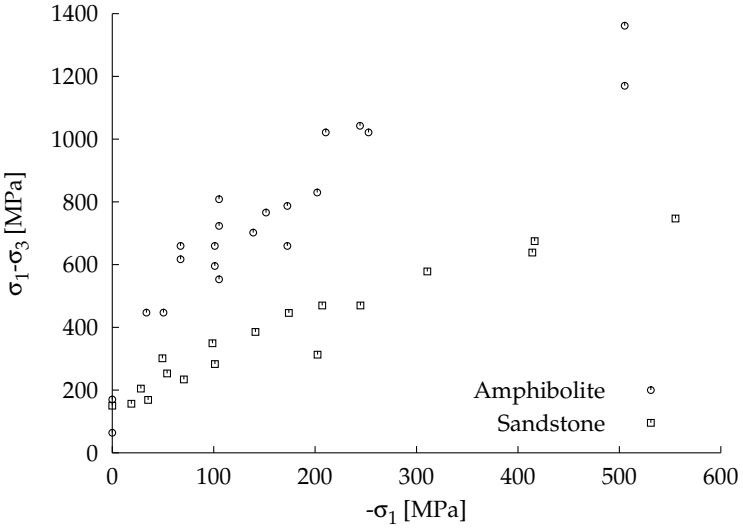

Figure II.4: $(\sigma_1 - \sigma_3)$-σ_1 diagram for amphibolite and sandstone (after Lockner, 1995)

It is of interest to note that the majority of strength measurements have been conducted under uniaxial or triaxial stress conditions. A limited number of true triaxial ($\sigma_1 > \sigma_2 > \sigma_3$) measurements have been performed to explore the effect of intermediate principal stress on failure mode. While the most commonly used failure criteria (e.g., Mohr Coulomb) assume that failure is independent of the intermediate stress, experimental evidence demonstrates that this assumption is not strictly true (Lockner, 1995).

II.3.2.2 Strain rate effect

Dynamic loads are usually associated with high amplitude and short duration. For exemple, in rock blasting, a blast stress wave is generated and propagates through the rock mass; the rock mass and rock strcuture are subjected to blast shock loads at different loading strain rates (from about $10^0 s^{-1}$ to $10^3 s^{-1}$). Under highly dynamic conditions, the strain-rate dependence of concrete and rocks response causes the material behaviour to be significantly different from what is observed under quasi-static conditions.
Techniques for experiments at high strain rates are not well developed and, in general, leave questions with respect to interpretation of data when the material behaves in a quasi-brittle manner. On the other hand, experimental results are usually obtained under the assumption of homogeneous stress and strain fields in the specimen, even in the high dynamic range where transient loadings are heterogeneous by nature.
The most reliable data at high strain rates are found by using the Split Hopkinson Pressure Bar (SHPB)Technique. The common conclusion of the majority of researchers found in literature indicates that rocks and concrete exhibit a viscous effect which is reflected in a strength increase with increasing strain rate (Perkins et al, 1970; Peng, 1973; Chong et al, 1980; Sierakowski, 1984; Gran et al, 1989; Yalun, 1990; Reinhardt et al, 1990 Olsson, 1991; Gary and Bailly, 1998; Malvar and Crawford, 1998; Tedesco and Ross, 1998; Zhao et al, 1999; Frew et al, 2001; Grote et al, 2001; to cite only a few).
The Dynamic Increase Factor (DIF), i.e. the ratio of the dynamic to static strength, for the tensile strength is plotted in Fig. II.5 versus the strain rate for concrete (Malvar and Crawford, 1998). Fig. II.6 shows the compressive Dynamic Increase Factor of Indiana limestone versus the strain rate for different size of the tested samples (Frew et al, 2000). Unlike much of rocks and concrete data, Fig. II.6 shows that the Indiana limestone does not present a size effect.
Zhao et al (1999) show that the dynamic uniaxial compression test for the Bukit Timah granite in Singapore increases from 205 MPa to 235 MPa with loading rate increasing from 10^0 to 10^5 MPa/s.
On the other hand, Blanton (1981) affirms that inertial forces play an important role at strain rates between 10^{-1} and 10 s^{-1}, and the findings of his study on three rocks (Charcoal Granodiorite, Berea Sandstone and Indiana Limestone) suggest that the apparent sudden increase in failure stress above a strain rate of about 1 s^{-1} is due to machine inertia and does not reflect a real increase in material strength. The same idea can be supported by Nikolaevskiy (1996) who indicates that the dynamic measured strength, which is interpreted as the *dynamic strength*, depends on the condition of the shock, sample geometry, etc., and it does not reflect a material property, but a function of the dynamical process.

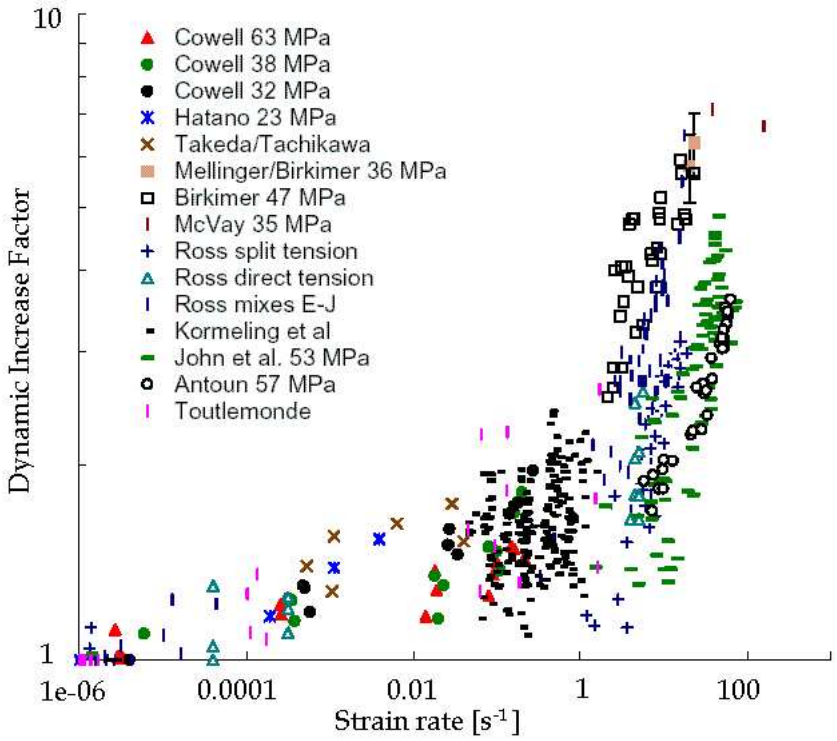

Figure II.5: DIF for concrete in tension (after Malvar and Crawford, 1998)

II.4 Constitutive modelling

It is not a trivial task to derive proper material law for quasi-brittle materials in the 3-dimensional stress state and which can be used in the hole range of loadings (from quasi-static to dynamic). Materials such as concrete and rocks undergo elastic, plastic and viscous behaviour, they are anisotropic, brittle in tension as well as in shear and ductile under high pressure.
In recent years there has been a tremendous effort aimed at developing accurate models that predict the response of such materials under various loading conditions. Most of them are of the phenomenal type. The aim of a phenomenal model is to reproduce mathematically the macroscopic stress-strain relations for different loading conditions, neglecting the microscopic mechanism of the behaviour. The plasticity/viscoplasticity and the damage approaches falls into this category.
In order to estimate stress wave induced fracturing, a coupled elasto-viscoplastic and rate dependent damage model has been developed. Within the regime of load application, an isotropic elasticity tensor is used to govern the elastic material behaviour. A pressure dependent elasto-viscoplastic model is used for compressive regime. A second order tensor measure of damage is used to represent the anisotropic degradation of the elasticity tensor under tensile regime. Only the isothermal case will be considered.

II.4.1 Plasticity theory applied to modelling quasi-brittle materials behaviour under Compressive loading

The classical theory of plasticity was originally developed for metals which have deformational mechanisms quite different from those of concrete and rocks. However, from a macroscopic point of view, they still have some similarities, particularly in the prefailure regime and under compressive loading with high confining pressure.

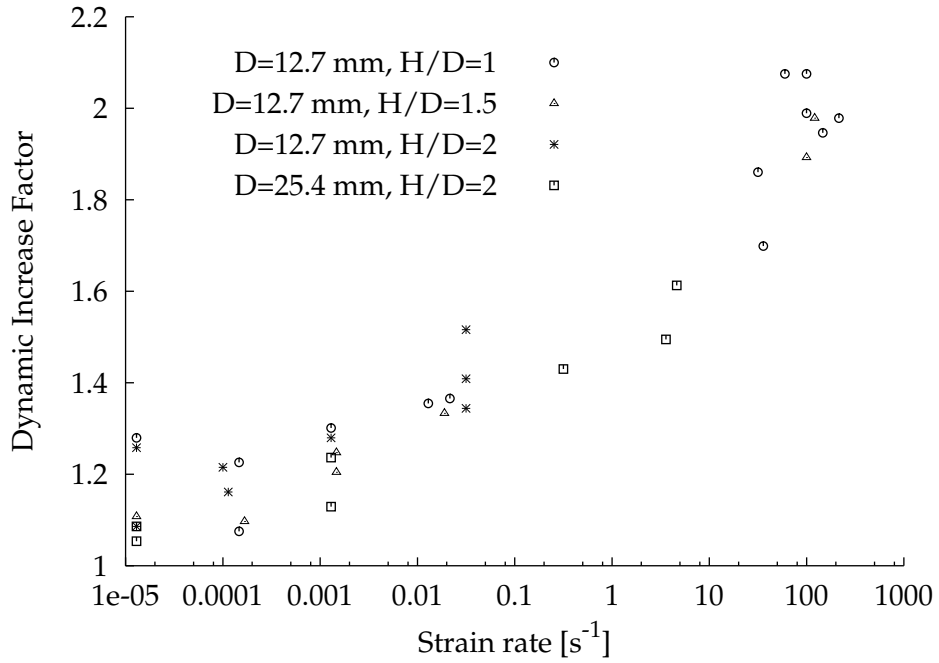

Figure II.6: DIF of Indiana limestone in compression (after Frew et al, 2000)

II.4.1.1 Problem formulation

In this work, we assume that the softening behaviour of quasi-brittle materials is a purely material property. Therefore, both hardening and softening effects can be introduced as hidden internal variables in the thermodynamic state potential. The Helmholtz specific free energy is considered here as the thermodynamic state potential depending on both observable and internal state variables. The form of this potential is given by Eq. (II.19) where $\boldsymbol{\xi}_k$, in this case, are the inelastic strain tensor $\underline{\underline{\epsilon}}^{in}$ and scalars variables characterizing the isotropic hardening/softening in plasticity/viscoplasticity.
Addressing the isothermal case, a commonly used assumption is to decompose the Helmholtz specific free energy into elastic strain dependent potential ψ^e and internal variable dependent potential ψ^ξ (Lemaitre and Chaboche, 1985)

$$\psi\left(\underline{\underline{\epsilon}},\ \boldsymbol{\xi}_k\right) = \psi^e\left(\underline{\underline{\epsilon}}^e\right) + \psi^\xi\left(\boldsymbol{\xi}_k\right) \tag{II.24}$$

In this study we assume that $\psi^\xi = 0$. For linearized elasticity, ψ is a quadratic form in the elastic strain

$$\psi\left(\underline{\underline{\epsilon}},\ \boldsymbol{\xi}_k\right) = \psi^e\left(\underline{\underline{\epsilon}}^e\right) = \frac{1}{2\rho}\underline{\underline{\epsilon}}^e : \underline{\underline{\underline{\underline{\mathrm{H}}}}} : \underline{\underline{\epsilon}}^e \tag{II.25}$$

where $\underline{\underline{\underline{\underline{\mathrm{H}}}}}$ is the elasticity tensor which, in the case of isotropic behaviour, is given by

$$\underline{\underline{\underline{\underline{\mathrm{H}}}}} = \lambda \underline{\underline{\mathrm{I}}} \otimes \underline{\underline{\mathrm{I}}} + 2\mu \underline{\underline{\mathrm{I}}} \,\overline{\otimes}\, \underline{\underline{\mathrm{I}}} \tag{II.26}$$

where λ and μ are the Lamé elastic parameters.
Then Eq. (II.7), Eq. (II.21) and Eq. (II.25) imply

$$\underline{\underline{\sigma}} = \underline{\underline{\underline{\underline{\mathrm{H}}}}} : \left(\underline{\underline{\epsilon}} - \underline{\underline{\epsilon}}^{in}\right) \quad \text{in } \Omega \times [0,T] \tag{II.27}$$

The definition of the plastic/viscoplastic model is completed with the introduction of the

evolution equations for the internal variables $(\boldsymbol{\xi}_k)$. These evolution equations read in general form

$$\dot{\boldsymbol{\xi}}_k = \dot{\gamma}\boldsymbol{\ell}_k\left(\underline{\underline{\sigma}},\ \boldsymbol{\xi}_k\right) \tag{II.28}$$

Here $\boldsymbol{\ell}_k : \mathbf{S} \times \mathbb{R}^k \longmapsto \mathbb{R}^k$ are functions which define the direction of plastic flow and the hardening/softening evolution laws. The parameter $\dot{\gamma} \geq 0$ is the plastic consistency parameter.
In order to determine $\dot{\gamma}$ we need, in a first time, to define a function $\mathbf{F} : \mathbf{S} \times \mathbb{R}^k \longmapsto \mathbb{R}$ called the **yield criterion** and constrain the admissible states $\left(\underline{\underline{\sigma}},\ \boldsymbol{\xi}_k\right) \in \mathbf{S} \times \mathbb{R}^k$ in stress space to lie in the set $\mathbb{E}$ defined as

$$\mathbb{E} = \left\{\left(\underline{\underline{\sigma}},\ \boldsymbol{\xi}_k\right) \in \mathbf{S} \times \mathbb{R}^k \mid \mathbf{F}\left(\underline{\underline{\sigma}},\ \boldsymbol{\xi}_k\right) \leq 0\right\} \tag{II.29}$$

One refers to the interior of $\mathbb{E}$, denoted by $int(\mathbb{E})$ and given by

$$int(\mathbb{E}) = \left\{\left(\underline{\underline{\sigma}},\ \boldsymbol{\xi}_k\right) \in \mathbf{S} \times \mathbb{R}^k \mid \mathbf{F}\left(\underline{\underline{\sigma}},\ \boldsymbol{\xi}_k\right) < 0\right\} \tag{II.30}$$

as the **elastic domain**; whereas the boundary of $\mathbb{E}$, denoted by $\partial\mathbb{E}$ and defined as

$$\partial\mathbb{E} = \left\{\left(\underline{\underline{\sigma}},\ \boldsymbol{\xi}_k\right) \in \mathbf{S} \times \mathbb{R}^k \mid \mathbf{F}\left(\underline{\underline{\sigma}},\ \boldsymbol{\xi}_k\right) = 0\right\} \tag{II.31}$$

is called the **yield surface** in stress space. Note that $\mathbb{E} = int(\mathbb{E}) \cup \partial\mathbb{E}$ and $\left(\underline{\underline{\sigma}},\ \boldsymbol{\xi}_k\right)$ outside $\mathbb{E}$ are non-admissible.

For the plastic multiplier $\dot{\gamma}$, we will distinguish, in the sequel, the rate-independent plasticity from the rate-dependent plasticity.

1. **Rate-independent plasticity**
   For rate-independent plasticity $\dot{\gamma}$ is assumed to obey the following Kuhn-Tucker complementary conditions:

$$\dot{\gamma} \geq 0, \quad \mathbf{F}\left(\underline{\underline{\sigma}},\ \boldsymbol{\xi}_k\right) \leq 0, \text{ and } \dot{\gamma}\mathbf{F}\left(\underline{\underline{\sigma}},\ \boldsymbol{\xi}_k\right) = 0 \tag{II.32}$$

   If $\left(\underline{\underline{\sigma}},\ \boldsymbol{\xi}_k\right) \in \partial\mathbb{E}$ which implies that $\mathbf{F}\left(\underline{\underline{\sigma}},\ \boldsymbol{\xi}_k\right) = 0$, then, the time derivative of $\dot{\gamma}\mathbf{F}\left(\underline{\underline{\sigma}},\ \boldsymbol{\xi}_k\right) = 0$ gives the consistency condition

$$\dot{\gamma}\dot{\mathbf{F}}\left(\underline{\underline{\sigma}},\ \boldsymbol{\xi}_k\right) = 0 \tag{II.33}$$

   Condition (II.32) characterize the loading/unloading conditions while Eq. (II.33) define the persistency of the plastic state during plastic flow.

   Remarks: interpretation of the Kuhn-Tucker complementarity conditions

   – Consider the case in which $\left(\underline{\underline{\sigma}},\ \boldsymbol{\xi}_k\right) \in int(\mathbb{E})$ so that, according to (II.30) $\mathbf{F}\left(\underline{\underline{\sigma}},\ \boldsymbol{\xi}_k\right) < 0$. Therefore, from condition (II.32) we conclude that

$$\dot{\gamma}\mathbf{F}\left(\underline{\underline{\sigma}},\ \boldsymbol{\xi}_k\right) = 0 \ \text{ and } \mathbf{F} < 0 \ \Rightarrow \ \ \dot{\gamma} = 0 \tag{II.34}$$

     Then from (II.28) it follows that $\dot{\boldsymbol{\xi}}_k = 0$. Thus $\underline{\underline{\dot{\epsilon}}} = \underline{\underline{\dot{\epsilon}}}^e$, and the rate form of (II.27) leads to

$$\dot{\underline{\underline{\sigma}}} = \underline{\underline{\underline{\underline{\mathrm{H}}}}} : \underline{\underline{\dot{\epsilon}}} \tag{II.35}$$

     This type of response is called *instantaneously elastic*.

– Now suppose that $\left(\underline{\underline{\sigma}},\ \boldsymbol{\xi}_k\right) \in \partial\mathbb{E}$ which, in view of (II.31), implies that $\mathbf{F}\left(\underline{\underline{\sigma}},\ \boldsymbol{\xi}_k\right) = 0$. Then condition (II.32) is automatically satisfied even if $\dot{\gamma} > 0$. Whether $\dot{\gamma}$ is actually positive or zero is concluded from (II.33). Three situations can arise.

(a) If $\dot{\mathbf{F}}\left(\underline{\underline{\sigma}},\ \boldsymbol{\xi}_k\right) < 0$, from condition (II.33) we conclude that

$$\dot{\gamma}\dot{\mathbf{F}} = 0 \text{ and } \dot{\mathbf{F}} < 0 \quad \Rightarrow \dot{\gamma} = 0 \tag{II.36}$$

Thus, again from (II.28) it follows that $\dot{\boldsymbol{\xi}}_k = 0$. Since (II.35) holds and $\left(\underline{\underline{\sigma}},\ \boldsymbol{\xi}_k\right)$ is on $\partial\mathbb{E}$, this type of response is called *unloading from a plastic state.*

(b) If $\dot{\mathbf{F}}\left(\underline{\underline{\sigma}},\ \boldsymbol{\xi}_k\right) = 0$, condition (II.33) is automatically satisfied. If $\dot{\gamma} > 0$, then $\dot{\boldsymbol{\xi}}_k \neq 0$. This type of response is called plastic loading. The case $\dot{\gamma} = 0$ (and $\dot{\mathbf{F}} = 0$) is termed *neutral loading*

(c) If $\dot{\mathbf{F}}\left(\underline{\underline{\sigma}},\ \boldsymbol{\xi}_k\right) > 0$ for $\left(\underline{\underline{\sigma}},\ \boldsymbol{\xi}_k\right) \in \partial\mathbb{E}$ at some time t, then condition $\mathbf{F} \leq 0$ would be violated at a neighboring subsequent time. Therefore, this possibility is excluded.

2. **Rate-dependent plasticity (viscoplasticity)**
In order to account for the loading rate dependency, a viscous mechanism needs to be introduced. Such consideration accounts for the retardation of the mico-crack growth at higher strain rates.
As in rate-independent plasticity, in classical formulations of viscoplasticity, one also introduces an elastic range which is defined, in terms of a loading function $\mathbf{F}\left(\underline{\underline{\sigma}},\ \boldsymbol{\xi}_k\right)$ by the same set given by Eq. (II.29). The basic difference between viscoplasticity and rate-independent plasticity is that in the former model states $\left(\underline{\underline{\sigma}},\ \boldsymbol{\xi}_k\right)$, such that $\mathbf{F}\left(\underline{\underline{\sigma}},\ \boldsymbol{\xi}_k\right) > 0$ that is, stress outside the closure of the elastic range, are permissible, whereas in the latter constitutive model such states are not allowed.
Among the various constitutive theories for rate-dependent plastic deformation appropriate for high rates of deformation, the Perzyna-type viscoplastic models (1966) appear well suited for modelling dynamic fracture. In such models, the viscoplasticity is recovered from the previous expressions by replacing the relations (II.32) by the explicit definition

$$\dot{\gamma} = \frac{1}{\eta}\varphi(\mathbf{F}) \tag{II.37}$$

where $\eta \in]0,\ +\infty[$ denotes a given material parameter called fluidity or viscosity parameter, while φ denotes a general scalar function satisfying the conditions

$$\varphi(\mathbf{F}) = 0 \text{ for } \mathbf{F} \leq 0, \quad \text{and } \varphi'(\mathbf{F}) > 0 \text{ for } \mathbf{F} > 0 \tag{II.38}$$

for its first derivative $\varphi'(.)$, that is, monotonically increasing function $\varphi(\mathbf{F})$ of the loading function for $\mathbf{F} > 0$ (no longer restricted to non-positive values).

II.4.1.2 Failure surface

To reproduce the above experimental observations, the overall concrete and rocks response can be divided into three regions: an initial linear elastic regime, a non-linear hardening pre-peak, and a non linear softening post-peak regime. The elastic response is bounded by an initial yield surface, which grows with the increasing inelastic deformations (hardening). During hardening, the loading surface expands and changes its shape from the initial yield surface to the final shape that matches with the **failure surface**. In the low-confined compression regime there is a transition point that separates ductile hardening behaviour from

brittle softening regime. In the softening regime, the yield surface is gradually weakened, from the failure surface, until reaching a **residual strength yield surface**.
The yield surface of concrete and rocks in the stress space is not easy to be measured experimentally. For this reason it is usually assumed on the basis of the known **failure surface**. It should be emphasized that failure surface can be fromulated in stress, strain or energy space. The strain-based or energy-based failure descriptions involve elastic material properties, while failure description in stress space constrains the stress state independently of elastic material description. As a consequence, the stress-based failure surface infers that the strength is independent of the stiffness, thus there is no correlation between the elastic modulus and the uniaxial compressive strength. In contrast, the strain and energy-based limit models correlate stiffness and strength.
In what follows we will consider only the failure surface formulated in the stress space.

The general form of a failure surface can be expressed by the scalar-valued function $\mathbf{F}\left(\underline{\underline{\sigma}}\right) = 0$, which describes the failure envelope in six-dimensional stress space. This function must respect the *material symmetry*: for isotropic materials, $\mathbf{F}$ can only depend on the set of the three independent scalar invariants, e.g., in the form of three principal stresses, $\mathbf{F}(\underline{\underline{\sigma}}) = \mathbf{F}\left(\sigma_1,\ \sigma_2,\ \sigma_3\right) = 0$. Alternatively, $\mathbf{F}$ can be written as

$$\mathbf{F}\left(p,\ q,\ \theta\right) = 0 \tag{II.39}$$

where p, q and θ are three stress invariants given by

$$p = -\frac{\mathrm{tr}(\underline{\underline{\sigma}})}{3} \tag{II.40}$$

$$q = \sqrt{\frac{3}{2}\underline{\underline{s}} : \underline{\underline{s}}} \tag{II.41}$$

$$\theta = \arccos\left(\frac{3}{2}\frac{s_1}{q}\right) \quad \text{for} \quad \theta \in [0,\ \frac{\pi}{3}] \tag{II.42}$$

Here $s_1 = \sigma_1 + p$ and $\underline{\underline{s}}$ denotes the deviatoric stress tensor:

$$\underline{\underline{s}} = \underline{\underline{\sigma}} + p\underline{\underline{\mathrm{I}}} \tag{II.43}$$

and θ is the deviatoric polar angle.
For $\theta \in [0,\ \frac{\pi}{3}]$ and consequently for $\sigma_1 \geq \sigma_2 \geq \sigma_3$ we have the following relationship between $(\sigma_1,\ \sigma_2,\ \sigma_3)$ and $(p,\ q,\ \theta)$

$$\begin{cases} \sigma_1 = -p + \frac{2}{3}q\cos\theta \\ \sigma_2 = -p + \frac{2}{3}q\sin(\theta - \frac{\pi}{6}) \\ \sigma_3 = -p - \frac{2}{3}q\sin(\theta + \frac{\pi}{6}) \end{cases} \tag{II.44}$$

A particular class of failure surface functions is introduced for pressure-sensitive materials. In the most cases, this class of functions is illustrated by Mohr-Coulomb and Drucker-Prager models. The objective of the present section is to propose a formulation which accounts for a larger response spectrum of stress states and loading paths. Before doing that, we shall start with a discussion of the Mohr-Coulomb and the Drucker-Prager failure surfaces.

The Mohr-Coulomb failure surface

Let $\overrightarrow{n}$ be a unit vector normal to an arbitrary plan passing through a point $\overrightarrow{x}$. The magnitude of the normal stress and the shear stress components at the point $\overrightarrow{x}$ can be expressed as

$$\sigma = \overrightarrow{n}\ .\ \underline{\underline{\sigma}}\ .\ \overrightarrow{n}\ ; \quad \tau = ||\underline{\underline{\sigma}}\ .\overrightarrow{n} - \sigma\,\overrightarrow{n}|| \tag{II.45}$$

Mohr's failure criterion considers that, at a point, the limiting shear stress in a plane is a function of the normal stress in the same plane, i.e.,

$$|\tau| = \mathcal{M}(\sigma) \tag{II.46}$$

where $\mathcal{M}$ is an experimentally determined function. The simplest form of the Mohr function $\mathcal{M}$ is known as Coulomb's equation defined as

$$|\tau| = c - \sigma \tan\phi \tag{II.47}$$

where c is the cohesion and ϕ is the angle of internal friction; both are material constants determined by experiments. The failure surface associated with Eq. (II.47) will be referred to as the Mohr-Coulomb surface. Since (II.47) must hold for any arbitrary vector $\overrightarrow{n}$, the principal stresses must verify

$$\frac{\sigma_1 - \sigma_3}{2}\cos\phi = c - \left[\frac{\sigma_1 + \sigma_3}{2} + \frac{\sigma_1 - \sigma_3}{2}\sin\phi\right]\tan\phi \tag{II.48}$$

If we define

$$K = \frac{1 + \sin\phi}{1 - \sin\phi} \tag{II.49}$$

and

$$R_c = \frac{2c\cos\phi}{1 - \sin\phi} \tag{II.50}$$

Eq. (II.48) is reduced to

$$K\sigma_1 - \sigma_3 = R_c \quad \text{for } \sigma_1 \geq \sigma_2 \geq \sigma_3 \tag{II.51}$$

It is clear from Eq. (II.51) that R_c is the strength in the uniaxial compression.
According to Eq. (II.44), (II.51) can also be rewritten, in terms of variables $p,\ q$ and θ, as follows

$$\mathbf{F}(p,\ q,\ \theta) = q - g(\theta)f(p) = 0 \tag{II.52}$$

with

$$g(\theta) = \frac{1}{K\cos\theta + \sin\left(\theta + \frac{\pi}{6}\right)} \quad \text{for } \theta \in [0,\ \frac{\pi}{3}] \tag{II.53}$$

$$f(p) = \frac{3}{2}\left[R_c + (K-1)p\right] \tag{II.54}$$

It is of interest to note that the ratio $q|_{(\theta=0,\ p)}/q|_{(\theta=\pi/3,\ p)}$, corresponding to the ratio of the tensile meridian to the compression meridian, is only internal friction angle dependent

$$\frac{q|_{(\theta=0,\ p)}}{q|_{(\theta=\frac{\pi}{3},\ p)}} = \frac{3 - \sin\phi}{3 + \sin\phi} \quad \forall\ p\ \in\ ]\frac{R_c}{1-K},\ +\infty[\tag{II.55}$$

In principal stress space, the Mohr-Coulomb envelope is an irregular hexagonal pyramid. Its meridians are straight lines (Fig. II.7), and its cross section in the π-plane ($p = 0$) is an irregular hexagon (Fig. II.8). The hexagons shown in Fig. II.9 are the intersections of the pyramid with the coordinate plane $\sigma_3 = 0$. When $\phi = 0$, the hexagons become identical with Tresca's hexagons as shown in Fig. II.8 and II.9. In Fig. II.9 the axes Σ_1, Σ_2, and Σ_3 are the projections of the axes σ_1, σ_2, and σ_3 on the deviatoric plane.

The Drucker-Prager failure surface

In the principal stress space, the Drucker-Prager surface is a cone with a circular deviatoric section centered on the hydrostatic axis

$$\mathbf{F}(p,\ q,\ \theta) = \mathbf{F}(p,\ q) = q - f(p) \tag{II.56}$$

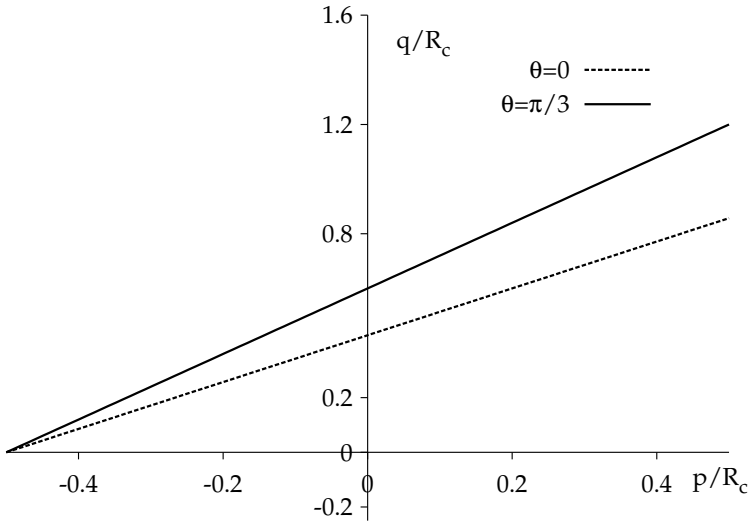

Figure II.7: Meridians of the Mohr-Coulomb failure surface

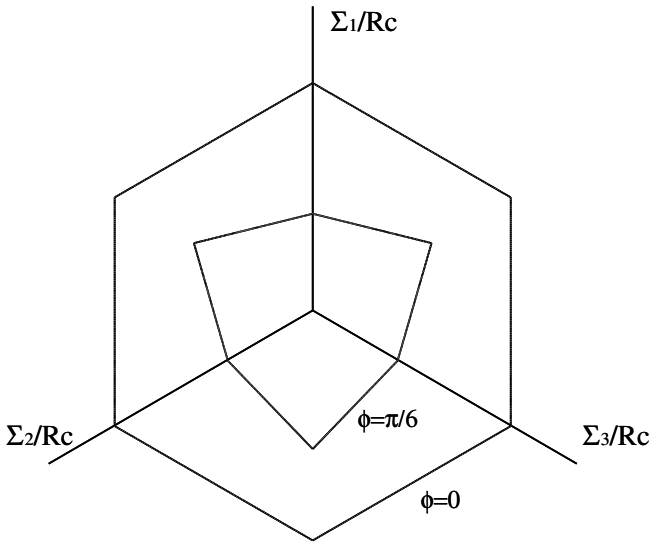

Figure II.8: Mohr-Coulomb failure surface in the deviatoric plane

where $f(p)$ is a linear function of the mean stress p

$$f(p) = \alpha_1 p + \alpha_2 \tag{II.57}$$

where α_1 and α_2 are material parameters. Obviously, when $\alpha_1 = 0$, the Drucker-Prager failure surface becomes identical with the Von Mises's surface.
α_1 and α_2 may be calibrated such that the Mohr-Coulomb surface and the Drucker-Prager surface are made to coincide along the compression meridain ($\theta = \pi/3$). In this case α_1 and α_2 can be related to the constants c and ϕ by

$$\alpha_1 = \frac{6\sin(\phi)}{3 - \sin(\phi)}, \quad \alpha_2 = \frac{6c\cos(\phi)}{3 - \sin(\phi)} \tag{II.58}$$

The cone corresponding to the constants given by Eq. (II.58) circumscribes the Mohr-Coulomb hexagonal pyramid (Fig. II.10). On the other hand, the inner cone passes through the tension meridian ($\theta = 0$) will be characterised by the constants

$$\alpha_1 = \frac{6\sin(\phi)}{3 + \sin(\phi)}, \quad \alpha_2 = \frac{6c\cos(\phi)}{3 + \sin(\phi)} \tag{II.59}$$

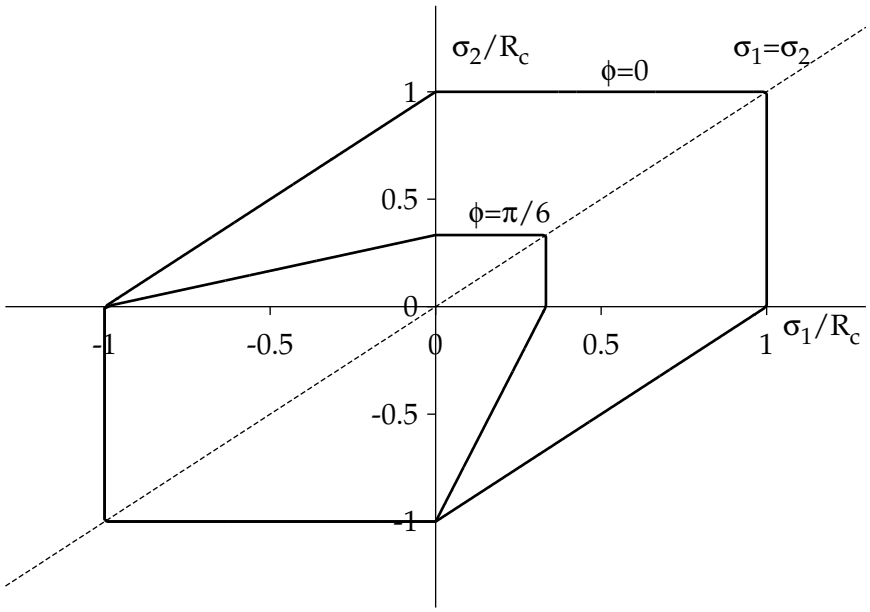

Figure II.9: Mohr-Coulomb failure surface in the coordinate plane $\sigma_3 = 0$

However, the approximation given by either the inner or the outer cone to the Mohr-Coulomb failure surface can be poor for certain stress states as can be seen in Fig. II.10b for the plan stress state ($\sigma_3 = 0$).
The use of Mohr-Coulomb and Drucker-Prager models for the description of rocks and concrete is restricted to moderately stresses. However, because of their relatively simple formulation, these models are commonly used in numerical analysis beyond their original range of applicability. The need for realistic material models covering a larger response spectrum of stress states and loading paths is evident when we try to consider the blasting problem which involves, amongst other things, high hydrostatic pressures.

It's well known that failure envelopes for rocks are, in general, concave towards the mean stress p. At high pressures, strength eventually becomes insensitive to pressure (Lockner, 1995) and the material behaviour becomes fully ductile. Because the classic strength theories used for other engineering materials have been found not to apply to quasi-brittle materials over a wide range of applied compressive stress conditions, a number of empirical strength criterion have been introduced for practical use. Among them one can find the empirical strength criterion that was developed by Hoek and Brown (1980) for rock masses. For such criterion, the failure surface can be expressed in terms of the maximum principal stress σ_1 and the minimum principal stress σ_3 as

$$\left[\frac{\sigma_1 - \sigma_3}{R_c}\right]^2 + m\frac{\sigma_1}{R_c} - c = 0 \tag{II.60}$$

where m, c and R_c are material parameters.
In what follows we will propose a formulation, based on the Hoek and Brown failure surface, which accounts for a large spectrum of stress states. The formulation aims at taking into account the effect of the third stress invariant and the high hydrostatic pressure.
To overcome the fact that Eq. (II.60) does not account for the intermediate principal stress, one can use Eq. (II.44) to exchange principal stresses ($\sigma_1,\ \sigma_3$) by the description using ($p,\ q,\ \theta$) invariants

$$\left[\frac{2}{3}\frac{q}{R_c}\left(\cos\theta + \sin(\theta + \frac{\pi}{6})\right)\right]^2 - \frac{2}{3}m\frac{q\cos\theta}{R_c} - m\frac{p}{R_c} - c = 0 \tag{II.61}$$

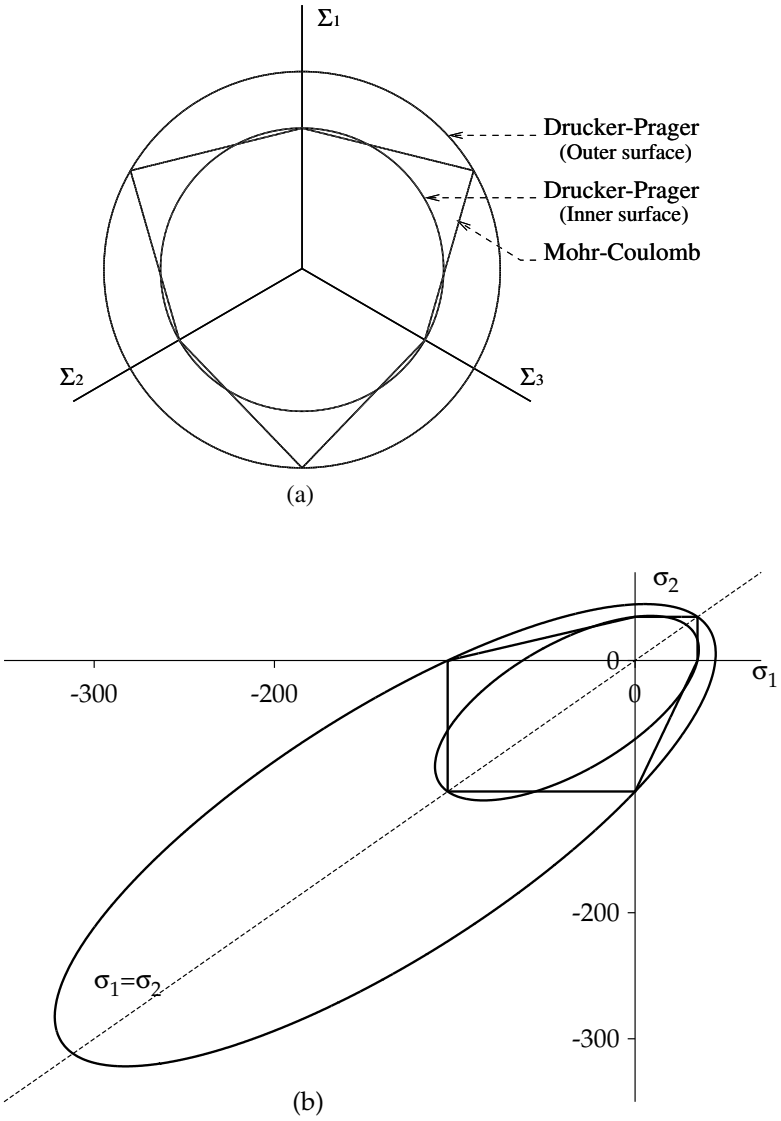

Figure II.10: The Mohr-Coulomb and the Drucker-Prager failure surfaces matched along the compressive and the tensile meridians: (a) in the deviatoric plane; (b) in the coordinate plane $\sigma_3 = 0$.

In particular, for $\theta = \pi/3$, Eq. (II.61) becomes

$$\left[\frac{q_c}{R_c}\right]^2 + \frac{m}{3}\frac{q_c}{R_c} - m\frac{p}{R_c} - c = 0 \tag{II.62}$$

where $q_c = q|_{(\theta=\pi/3,\ p)}$. In order to consider a smooth deviatoric section, Klisinski (1985) proposed to replace the stress components q_c by the polar coordinate $q/\boldsymbol{\ell}(\theta)$, where $\boldsymbol{\ell}$ is a smooth elliptic function given by

$$\boldsymbol{\ell}(\theta) = \frac{2(1-\beta^2)\cos\theta + (2\beta-1)\sqrt{4(1-\beta^2)\cos^2\theta + 5\beta^2 - 4\beta}}{4(1-\beta^2)\cos^2\theta + (2\beta-1)^2}, \qquad \beta \in [\frac{1}{2},\ 1] \tag{II.63}$$

in which the parameter $\beta = q|_{(\theta=0,\ p)}/q|_{(\theta=\pi/3,\ p)}$ is referred to as eccentricity. Along the tensile ($\theta = 0$) and the compressive ($\theta = \pi/3$) meridians, the elliptic function takes the following values

$$\begin{cases} \boldsymbol{\ell}(0) = \beta \\ \boldsymbol{\ell}(\frac{\pi}{3}) = 1 \end{cases} \tag{II.64}$$

Since the isotropy is assumed, the cross section of the failure surface in the deviatoric plane have a $2\pi/3$ period and $\pi/3$ symmetry. Therefore, although it is only defined in the sector

$\theta \in [0,\ \frac{\pi}{3}]$, $\boldsymbol{\ell}$ extends, by symmetry, to all polar directions $\theta \in [0,\ 2\pi]$.
To preserve the convexity, the eccentricity must satisfy the condition $\beta \in [1/2,\ 1]$. At the upper limit, $\beta = 1$, the influence of the ploar angle θ disappears, and the deviatoric shape of the failure surface becomes circular. At the lower limit, $\beta = 1/2$, the deviatoric shape becomes a triangle.
Thus, the resulting failure surface, expressed in terms of the three stress invariants p, q, and θ, can be defined as

$$\mathbf{F}(p,\ q,\ \theta) = \left[\frac{1}{\boldsymbol{\ell}(\theta)}\frac{q}{R_c}\right]^2 + \frac{m}{3}\left[\frac{1}{\boldsymbol{\ell}(\theta)}\frac{q}{R_c}\right] - m\frac{p}{R_c} - c = 0 \tag{II.65}$$

Alternatively, Eq. (II.65) can be reduced to

$$\mathbf{F}(\bar{p},\ \bar{q},\ \theta) = \bar{q} - \boldsymbol{\ell}(\theta) f(\bar{p}) = 0 \tag{II.66}$$

with

$$\bar{p} = \frac{p}{R_c},\quad \bar{q} = \frac{q}{R_c},\qquad f(\bar{p}) = -\frac{m}{6} + \frac{1}{2}\sqrt{\frac{m^2}{9} + 4\,(m\bar{p} + c)}, \tag{II.67}$$

In order to ensure the concavity of the meridians of the failure surface at high pressures, we can introduce an additional parameter $n \leq 1$ in such a way that the failure surface becomes

$$\mathbf{F}(\bar{p},\ \bar{q},\ \theta) = \bar{q} - \boldsymbol{\ell}(\theta) f(\bar{p})^n = 0 \tag{II.68}$$

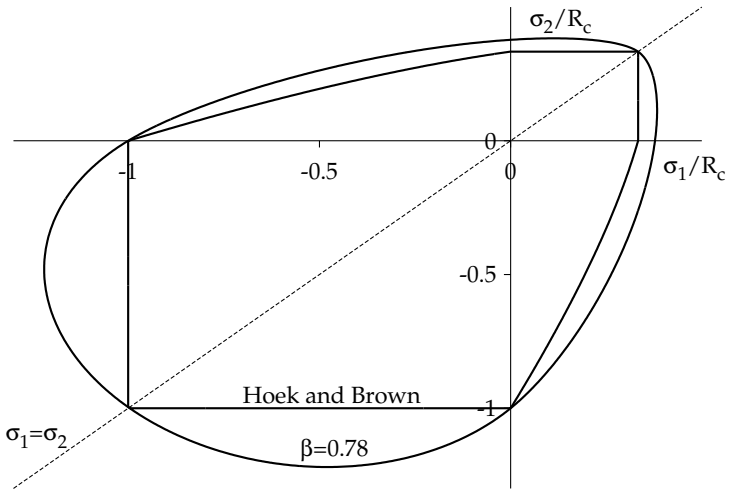

Figure II.11: Failure locus on $\sigma_1 - \sigma_2$ plane ($\sigma_3 = 0$) of the smooth and the Hoek & Brown failure surfaces.

The difference between the smooth failure surface as compared to the original Hoek and Brown surface is best appreciated if one considers the failure locus in the principal stress plane $\sigma_1 - \sigma_2$ (Fig. II.11) and in the deviatoric plane (Fig. II.12). These figures show both failure surfaces for $n = 1$ and $\beta = 0.78$. The elliptic variation of the deviatoric strength exhibits the effect of the intermediate principal stress that is missing in the original strength proposals by Hoek and Brown.
Fig. II.13 shows the compressive meridian of the new failure surface for different value of n. At high pressures, the pressure sensitivity decreases when $n \to 0$, it disappears completely for $n = 0$.
The influence of the eccentricity β is best illustrated in plane stress when the failure surface intersects the $\sigma_3 = 0$ plane. Fig. II.14 shows the trace of the failure surface for different

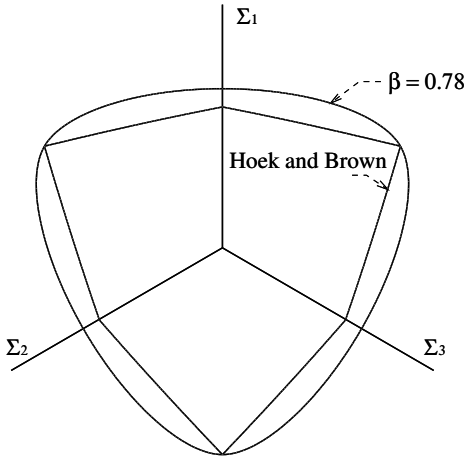

Figure II.12: The smooth and the Hoek & Brown failure surfaces in the deviatoric plane.

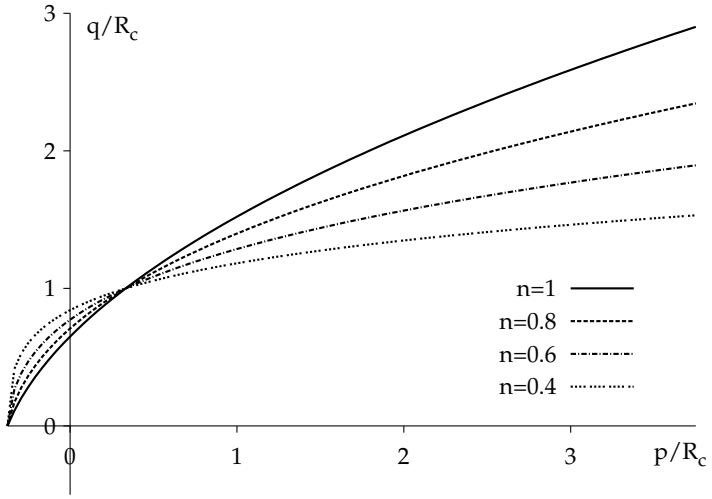

Figure II.13: The compression meridian of the smooth failure surface for different n.

values of the β. It can be seen that the eccentricity strongly affects the biaxial compression region.
Fig. II.15 shows the failure surface defined by Eq. (II.68) in the principal stress space.

Now, if we consider the compressive meridian, we can by curve fitting on triaxial tests data, calculate R_c, m, c, and n. Fig. II.16 shows the fitting results for the amphibilite and the sandstone defined in section II.3.

Finally, from experimental investigations found in literature, it is shown that the ratio $q|_{(\theta=0)}/q|_{(\theta=\pi/3)}$ can be a pressure dependent parameter. In fact, as indicated by Chen and Han (1987), it may increases with increasing hydrostatic pressure: it is about 1/2 near the π-plane and reaches a high of about 1 for high hydrostatic pressure. To account for this pressure dependency, one possibility is to choose the eccentricity β as a pressure dependent function

$$\beta = \beta(p) \tag{II.69}$$

subjected to the restrictions

$$\lim_{p\to+\infty} \beta(p) = 1 \quad \text{and} \quad \lim_{p\to-p_0} \beta(p) = \frac{1}{2} \tag{II.70}$$

Here, p_0 denotes the intersection point of the failure surface with the hydrostatic axis.

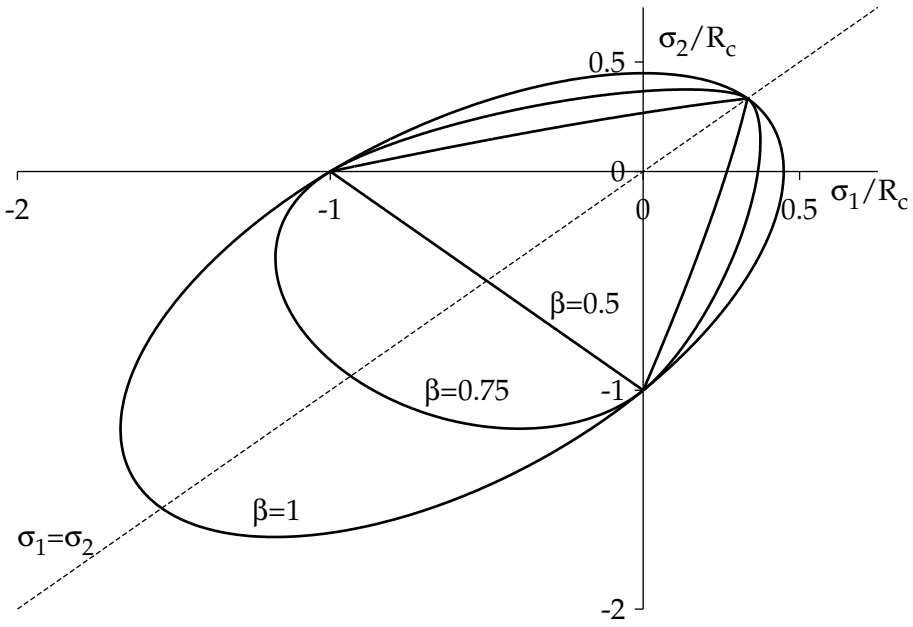

Figure II.14: Plane stress sections of the smooth failure surface for different β.

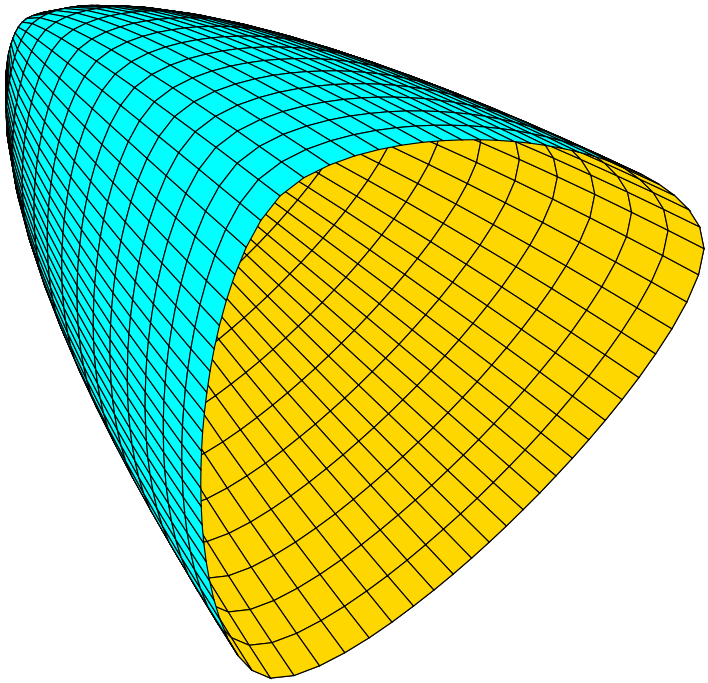

Figure II.15: Failure surface in principal stress space.

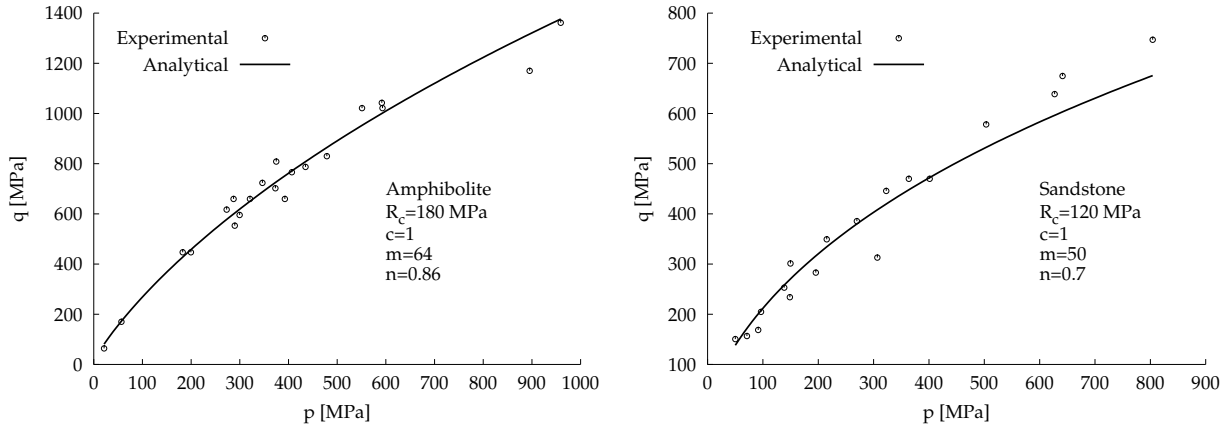

Figure II.16: The new failure surface compared to experimental data

II.4.1.3 Internal variables evolution laws

In what follows $\boldsymbol{\xi}_k$ will denote only hardening/softening internal variables.

Inelastic strain evolution law

If we admit that the rate effect on failure surface reflect a material property rather than a structural one, then, in this case, the natural way to take into account, this rate effect, is to consider rate-dependent models such as viscoplasticity. In the opposite case, rate-independent models seem to be the most appropriate. However, when strain softening is introduced, the last type of models may induce localization problem (we will discus this problem in section II.6). To overcome this problem, one possibility consists of using rate-dependent models. In such case, the fluidiy parameter, introduced in section II.4, will not referred as a material parameter, but it will be used only in order to regularize the localization problem.
In this study, we will restrict ourselves to the rate-dependent plasticity, in particular that of Perzyna-type. In this case, $\underline{\underline{\epsilon}}^{vp}$ will denotes the inelastic strain tensor ($\underline{\underline{\epsilon}}^{in} = \underline{\underline{\epsilon}}^{vp}$).
In classical plasticity/viscoplasticity, $\dot{\underline{\underline{\epsilon}}}^{vp}$ always denotes a vector parallel to the normal of a smooth scalar potential function $Q = Q\left(\underline{\underline{\sigma}},\ \boldsymbol{\xi}_k\right)$

$$\dot{\underline{\underline{\epsilon}}}^{vp} = \dot{\gamma}\underline{\underline{m}}\left(\underline{\underline{\sigma}},\ \boldsymbol{\xi}_k\right) = \dot{\gamma}\frac{\partial Q}{\partial \underline{\underline{\sigma}}}\left(\underline{\underline{\sigma}},\ \boldsymbol{\xi}_k\right) \tag{II.71}$$

Q differs from the yield function $\mathbf{F}$ in the non-associated case.
With the Helmholtz specific free energy given by Eq. (II.25), the Clausius- Duhem inequality (II.23) leads to

$$\underline{\underline{\sigma}} : \dot{\underline{\underline{\epsilon}}}^{vp} = \dot{\gamma}\underline{\underline{\sigma}} : \underline{\underline{m}} \geq 0 \tag{II.72}$$

Since $\dot{\gamma}$ is a positive function, inequality (II.72) is further reduced to

$$\underline{\underline{\sigma}} : \underline{\underline{m}} \geq 0 \tag{II.73}$$

When $\mathbf{F} \equiv Q$, the specification of a smooth scalar yield function which is convex with respect to $\underline{\underline{\sigma}}$ and satisfying $\mathbf{F}\left(\underline{\underline{\sigma}},\ \boldsymbol{\xi}_k\right) \leq 0$ is a sufficient condition to respect the preceding inequality.

For the plastic multiplier, it is defined by Eq. (II.37), where $\varphi(\mathbf{F})$ is a monotonically increasing function of the loading function for $\mathbf{F} > 0$. At this stage, it is essential to introduce the following additional assumption: the viscoplastic strain rate must be bounded, i.e., does

not increase indefinitely. In fact, stress states propagate in materials with the elastic wave velocities, but fracturing has its own limit velocity that is essentially smaller. The limit velocity is explained by the growth of the material toughness when the velocity is close to the Rayleigh wave velocity or by the dynamic instability of cracks at high-velocity growth (Nikolaevskiy, 1996). An elementary treatment leading to a prediction of maximum crack velocity is given by Meyers (1994). More rigorous solutions to this problem were given by Freund(1990). This assumption will be introduced through the following plastic multiplier

$$\dot{\lambda}_c(\underline{\underline{\sigma}},\ \boldsymbol{\xi}_k) = v_c \left[1 - \exp\left(-\left\langle \frac{\mathbf{F}\left(\underline{\underline{\sigma}},\ \boldsymbol{\xi}_k\right)}{R(\boldsymbol{\xi}_k)} \right\rangle^{n_c}\right)\right] \tag{II.74}$$

where $\langle x \rangle = (x + |x|)/2$ denotes McAuley brackets, $v_c,\ n_c$ are material parameters. v_c represents the maximum viscoplastic rate and R is the uniaxial compressive strength which is assumed to be function of the hardening/softening variables $\boldsymbol{\xi}_k$.

Non-Linear isotropic softening law

The material behaviour is assumed to be isotropic during the entire deformation history. Inelastic deformations occur when the elastic limit, which is defined by the initial yield surface, is exceeded. In consequence of strain-hardening, the compressive strength may increase, until the failure surface is reached. The evolution of the yield surface from its initial location to the failure surface can be controlled by strain-hardening internal variable. However, since the initial yield surface has a different shape than the failure surface, both the size and shape of the subsequent yield surfaces must vary continuously during hardening from the initial yield shape to the final failure shape. This is why the hardening is relatively complicated and the complexity will increase if we also consider the rate-dependent plasticity.
For this reason, in this study, we will restrict ourselves to the softening behaviour, i.e. the initial yield surface will be confused with the failure surface. As discussed above, the softening can be considered as a structural phenomenon rather than a material property, but in this work we assume also that it will be the case.
The principal task when developing such a formulation is to link the evolution of the yield surface with the degradation of the compressive strength and identify the internal variables which control the process. Isotropic softening will be assumed and the softening of the yield surface will be controlled by the change of the uniaxial compressive strength, thereby translating the failure surface along the hydrostatic axis (away from the tensile region) to finally arrive at a residual state. Like many other models, we introduce the following internal variable

$$\boldsymbol{\xi}_k = \xi(\overrightarrow{x},\ t) = \int_0^t ||\underline{\underline{\dot{\varepsilon}}}^{vp}(\overrightarrow{x},\ \tau)||d\tau \tag{II.75}$$

The reduction of the compressive strength is assumed to be given by the following relationship

$$R(\xi) = R_c\left[\alpha + (1-\alpha)\exp\left(-\omega_c \xi^2\right)\right],\quad \alpha \in [0,\ 1],\quad \omega_c \geq 0 \tag{II.76}$$

where R_c, α and ω_c are material parameters.

II.4.2 Damage theory applied to modelling quasi-brittle materials behaviour under tensile loading

On the phenomenological level, it's widely accepted that the failure of quasi-brittle materials under compressive loading can be modelled by means of classical plasticity theory. In this case, we can, as introduced earlier, use a scalar internal variable to describe the isotropic softening process. However, when we deal with tensile loading, the formation of cracks induces a

directional bias to the material structure. In fact, tensile loading in one direction leaves the tensile capacity intact in the transverse direction, the evolution of the corresponding yield surface in the stress space by an isotropic softening rule is questionable. To overcome this difficulty, several approaches have been investigated. Among them, one can find the use of a kinematic softening rule (Feenstra and De Borst, 1995). Nevertheless, this formulation, which was used only in 2D, was not able to take into account the crack-closure-reopening effect. Another approach which can be used in a particularly convenient manner to model both the load-induced anisotropy and the unilateral condition due to crack-closure-reopening effect is the so-called damage theory. The pioneering work of Kachanov (1958) furnishes the first example of a damage theory, restricted in principle to either one-dimensional or isotropic theories, via the *effective stress* concept. Since the introduction of this concept, models involving damage become progressively more popular and are nowadays often used for the constitutive description of quasi-brittle materials, such as rocks, concrete, ceramics, etc.
Damage in materials is usually induced by nucleation, growth and coalescence of certain microscopic cracks and cavities. Since the development of these cracks and cavities is governed by the action of applied stress and strain, material damage is essentially anisotropic. This feature is especially important in quasi-brittle materials damaged by the development of distributed and oriented microscopic cracks. Thus, a scalar damage variable often has a serious limitation to the description of material damage, and a number of theories have been developed to model the anisotropic damage state by means of damage variables ranging from a vector to higher order tensor.
The second-order symmetric damage tensors are the most commonly employed because they are mathematically simpler than the higher order tensors, and yet can describe most essential features of anisotropic damage. Though this second-order damage tensor cannot describe more complicated damage state than orthotropy, it has been often employed in the development of anisotropic damage theories (Cordebois and Sidoriff, 1982; Murkami and Kamiya, 1997; Halm and Dragon, 1998; Carol et al, 2001; to cite only a few).
In what follows, we will use the following damage tensor

$$\underline{\underline{\Theta}} = \sum_{i=1}^{3} \Theta_i \, \vec{n}_i \otimes \vec{n}_i \tag{II.77}$$

where Θ_i and $\vec{n}_i$ are respectively the principal values and the unit vectors of principal directions of the tensor $\underline{\underline{\Theta}}$.

II.4.2.1 Effective stress and strain, energy equivalence

Degradation may be understood as the average effect of distributed micocracks. **Effective stress** and **effective strain** are defined as stress and strain to which the material skeleton between micro-cracks is subjected. In this context, the relation between effective stress $\underline{\underline{\tilde{\sigma}}}$ and effective strain $\underline{\underline{\tilde{\epsilon}}}$ describes the constitutive behaviour of the undamaged material, which for the sake of simplicity, is assumed to be linear elastic and isotropic

$$\underline{\underline{\tilde{\sigma}}} = \underline{\underline{\underline{\underline{\mathrm{H}}}}}_0 : \underline{\underline{\tilde{\epsilon}}} = 2\mu \underline{\underline{\tilde{\epsilon}}} + \lambda \mathrm{tr}(\underline{\underline{\tilde{\epsilon}}}) \tag{II.78}$$

where $\underline{\underline{\underline{\underline{\mathrm{H}}}}}_0$ is the Hook isotropic elasticity tensor of the undamaged material.
Damage variables must relate the effective quantities to their **nominal** counterparts, which are the ones that are measured externally (observable variables) and satisfy equilibrium and compatibility at structural level. The relation between nominal stress $\underline{\underline{\sigma}}$ and nominal strain $\underline{\underline{\epsilon}}$ describes the constitutive behaviour of the damaged material

$$\underline{\underline{\sigma}} = \underline{\underline{\underline{\underline{\mathrm{H}}}}} \left(\underline{\underline{\Theta}} \right) : \underline{\underline{\epsilon}} \tag{II.79}$$

where $\underline{\underline{\underline{\underline{\mathrm{H}}}}}$ is the Hook elasticity tensor for the damaged material.
In a general state of deformation and damage, the nominal stress tensor $\underline{\underline{\sigma}}$ can be related to the effective stress tensor $\underline{\underline{\tilde{\sigma}}}$ by the following linear transformation

$$\underline{\underline{\sigma}} = \underline{\underline{\underline{\underline{\mathrm{M}}}}} : \underline{\underline{\tilde{\sigma}}} \tag{II.80}$$

where $\underline{\underline{\underline{\underline{\mathrm{M}}}}}$ is a fourth-order linear transformation operator. Depending on the form used for $\underline{\underline{\underline{\underline{\mathrm{M}}}}}$, it is very clear from Eq. (II.80) that the nominal stress tensor $\underline{\underline{\sigma}}$ is generally non-symmetric. Using a non-symmetric effective stress tensor as given by Eq.(II.80) to formulate a constitutive model will result in the introduction of the Cosserat and micropolar continua. However, the use of such complicated mechanics can easily avoided by symmetrizing the effective stress. One of the symmetrization methods is given by Cordebois and Sidoroff (1982) and is expressed as follows:

$$\underline{\underline{\sigma}} = \underline{\underline{\Theta}}^{-\frac{1}{2}} \,.\, \underline{\underline{\tilde{\sigma}}} \,.\, \underline{\underline{\Theta}}^{-\frac{1}{2}} \tag{II.81}$$

The fourth-order damage effect tensor corresponding to Eq. (II.80) can be defined such that

$$\underline{\underline{\underline{\underline{\mathrm{M}}}}} = \underline{\underline{\Theta}}^{-\frac{1}{2}} \,\overline{\otimes}\, \underline{\underline{\Theta}}^{-\frac{1}{2}} \tag{II.82}$$

where advantage has been taken of the symmetry of $\underline{\underline{\tilde{\sigma}}}$ to obtain a fourth-order tensor $\underline{\underline{\underline{\underline{\mathrm{M}}}}}$ with major symmetry

$$\mathrm{M}_{ijkl} = \mathrm{M}_{klij} = \mathrm{M}_{jikl} = \mathrm{M}_{ijlk} \tag{II.83}$$

For undamaged state, $\underline{\underline{\Theta}} = \underline{\underline{\mathrm{I}}}$, which corresponds to the identity transformation $\left(\underline{\underline{\sigma}} = \underline{\underline{\tilde{\sigma}}}\right)$.
In literature, one can find the damage tensor denoted by $\underline{\underline{D}}$ and defined such that

$$\underline{\underline{\Theta}} = \left(\underline{\underline{\mathrm{I}}} - \underline{\underline{D}}\right)^{-1} \tag{II.84}$$

The two tensors $\underline{\underline{\Theta}}$ and $\underline{\underline{D}}$ share principal axes and their principal values are related according to

$$\Theta_i = \frac{1}{1 - D_i} \tag{II.85}$$

D_i can be interpreted as the ratio of the area reduction in the plane perpendicular to $\overrightarrow{n}_i$ caused by the development of cracks (Murkami and Kamiya, 1997). D_i varies between 0 and 1 while Θ_i varies between 1 (no damage) and $+\infty$ (full damage).
$\underline{\underline{\Theta}}$ is considered as an internal state variable which characterises the anisotropic phenomenon of micro-crack distribution in the material.
In order to find the relation between nominal strain tensor and effective strain tensor, in literature, one can find three approaches: strain equivalence, stress equivalence and energy equivalence. In contrast to the strain and stress equivalence, energy equivalence induces symmetry in the secant stiffness and compliance tensors. For this reason we have made the choice of energy equivalence. In this approach, the stored elastic energy is the same in terms of effective quantities or in terms of nominal quantities:

$$\frac{1}{2}\underline{\underline{\sigma}} : \underline{\underline{\epsilon}} = \frac{1}{2}\underline{\underline{\tilde{\sigma}}} : \underline{\underline{\tilde{\epsilon}}} \tag{II.86}$$

Using Eqs. (II.81) and (II.86) we can easily obtain

$$\underline{\underline{\epsilon}} = \underline{\underline{\Theta}}^{\frac{1}{2}} \,.\, \underline{\underline{\tilde{\epsilon}}} \,.\, \underline{\underline{\Theta}}^{\frac{1}{2}} \tag{II.87}$$

Combining Eqs. (II.81) and (II.87) with Eq. (II.78), Eq. (II.79) becomes

$$\underline{\underline{\sigma}} = 2\mu\underline{\underline{\Theta}}^{-1} \,.\, \underline{\underline{\epsilon}} \,.\, \underline{\underline{\Theta}}^{-1} + \lambda(\underline{\underline{\epsilon}} : \underline{\underline{\Theta}}^{-1})\underline{\underline{\Theta}}^{-1} \tag{II.88}$$

Where $\underline{\underline{\Theta}}^{-\frac{1}{2}}$, $\underline{\underline{\Theta}}^{\frac{1}{2}}$ and $\underline{\underline{\Theta}}^{-1}$ can be expressed as

$$\underline{\underline{\Theta}}^{-\frac{1}{2}} = \sum_{i=1}^{3} \frac{1}{\sqrt{\Theta_i}} \overrightarrow{n}_i \otimes \overrightarrow{n}_i, \quad \underline{\underline{\Theta}}^{\frac{1}{2}} = \sum_{i=1}^{3} \sqrt{\Theta_i} \overrightarrow{n}_i \otimes \overrightarrow{n}_i, \quad \underline{\underline{\Theta}}^{-1} = \sum_{i=1}^{3} \frac{1}{\Theta_i} \overrightarrow{n}_i \otimes \overrightarrow{n}_i \tag{II.89}$$

Finally, Eq. (II.88) together with Eq. (II.79) lead to the following expression of the stiffness tensor:

$$\underline{\underline{\underline{\underline{\mathrm{H}}}}}\left(\underline{\underline{\Theta}}\right) = \lambda \underline{\underline{\Theta}}^{-1} \otimes \underline{\underline{\Theta}}^{-1} + 2\mu \underline{\underline{\Theta}}^{-1} \,\overline{\otimes}\, \underline{\underline{\Theta}}^{-1} \tag{II.90}$$

The compliance tensor can also be expressed as:

$$\underline{\underline{\underline{\underline{\mathrm{H}}}}}^{-1}\left(\underline{\underline{\Theta}}\right) = -\frac{\nu}{E} \underline{\underline{\Theta}} \otimes \underline{\underline{\Theta}} + \frac{1+\nu}{E} \underline{\underline{\Theta}} \,\overline{\otimes}\, \underline{\underline{\Theta}} \tag{II.91}$$

Notice that Eq. (II.90) and Eq. (II.91) presents the orthotropic structure of the stiffness and the compliance tensors in which $\underline{\underline{\Theta}}^{-1}$ and $\underline{\underline{\Theta}}$ simply replace the second-order identity tensor $\underline{\underline{\mathrm{I}}}$ in the undamaged state.

II.4.2.2 Damage evolution law

In this context, the thermodynamic state can be described by the total strain tensor $\underline{\underline{\epsilon}}$ and the damage tensor $\underline{\underline{\Theta}}$. Thus, the Helmholtz specific free energy function can take the following form

$$\psi = \psi\left(\underline{\underline{\epsilon}},\ \underline{\underline{\Theta}}\right) \tag{II.92}$$

In order to establish a thermodynamically consistent damage evolution law, the only thermodynamic restriction to be fulfilled is the Claussius-Duhem dissipation inequality (Eq. (II.23)) which, in this case, can be written as

$$-\rho \frac{\partial \psi}{\partial \underline{\underline{\Theta}}} : \dot{\underline{\underline{\Theta}}} = \underline{\underline{\mathrm{w}}} : \dot{\underline{\underline{\Theta}}} \geq 0 \tag{II.93}$$

where $\underline{\underline{\mathrm{w}}} = -\rho \frac{\partial \psi}{\partial \underline{\underline{\Theta}}}$ is the thermodynamic conjugate force associated to the state variable $\underline{\underline{\Theta}}$. The conjugate force associated to the state variable $\underline{\underline{\epsilon}}$ is

$$\underline{\underline{\sigma}} = \rho \frac{\partial \psi}{\partial \underline{\underline{\epsilon}}} \tag{II.94}$$

Using Eq. II.79 and II.94 we can easily obtain

$$\psi\left(\underline{\underline{\epsilon}},\ \underline{\underline{\Theta}}\right) = \frac{1}{2\rho} \underline{\underline{\epsilon}} : \underline{\underline{\underline{\underline{\mathrm{H}}}}}\left(\underline{\underline{\Theta}}\right) : \underline{\underline{\epsilon}} + \psi^{\Theta}\left(\underline{\underline{\Theta}}\right) \tag{II.95}$$

In what follows we assume that $\psi^{\Theta} = 0$. In view of Eq. (II.95), the thermodynamic conjugate force corresponding to $\underline{\underline{\Theta}}$ becomes

$$\underline{\underline{\mathrm{w}}} = -\frac{1}{2} \underline{\underline{\epsilon}} : \partial_{\underline{\underline{\Theta}}} \underline{\underline{\underline{\underline{\mathrm{H}}}}} : \underline{\underline{\epsilon}} \tag{II.96}$$

On the other hand, stiffness and compliance tensors are inverse to each other, i.e.,

$$\underline{\underline{\underline{\underline{\mathrm{H}}}}} : \underline{\underline{\underline{\underline{\mathrm{H}}}}}^{-1} = \underline{\underline{\underline{\underline{\mathrm{I}}}}}^{s} \tag{II.97}$$

where $\underline{\underline{\underline{\underline{\mathrm{I}}}}}^{s} = \underline{\underline{\mathrm{I}}} \,\overline{\otimes}\, \underline{\underline{\mathrm{I}}}$ is the symmetric fourth-order identity tensors. By differentiation, Eq. (II.97) leads to

$$\partial_{\underline{\underline{\Theta}}} \underline{\underline{\underline{\underline{\mathrm{H}}}}} = -\underline{\underline{\underline{\underline{\mathrm{H}}}}} : \partial_{\underline{\underline{\Theta}}} \underline{\underline{\underline{\underline{\mathrm{H}}}}}^{-1} : \underline{\underline{\underline{\underline{\mathrm{H}}}}} \tag{II.98}$$

The thermodynamic conjugate force $\underline{\underline{\mathrm{w}}}$ is then rewritten as

$$\underline{\underline{\mathrm{w}}} = \frac{1}{2}\underline{\underline{\sigma}} : \partial_{\underline{\underline{\Theta}}}\, \underline{\underline{\underline{\underline{\mathrm{H}}}}}^{-1} : \underline{\underline{\sigma}} \tag{II.99}$$

Making use of Eq. (II.91), one can obtain the following convenient expression of $\underline{\underline{\mathrm{w}}}$

$$\underline{\underline{\mathrm{w}}} = \frac{1+\nu}{E}\underline{\underline{\sigma}} \cdot \underline{\underline{\Theta}} \cdot \underline{\underline{\sigma}} - \frac{\nu}{E}\left(\underline{\underline{\sigma}} : \underline{\underline{\Theta}}\right)\underline{\underline{\sigma}} \tag{II.100}$$

This force has no clear physical meaning, which makes it difficult to propose and interpret damage rules (Chaboche, 1992). This reason motivates Carol et al (2001) to suggest a new internal state variable $\underline{\underline{\mathrm{L}}}$. This variable is a function of the history up to time t of the damage tensor $\underline{\underline{\Theta}}$ and is given by the following differential equation

$$\dot{\underline{\underline{\mathrm{L}}}} = 2\, \underline{\underline{\Theta}}^{-\frac{1}{2}} \cdot \dot{\underline{\underline{\Theta}}} \cdot \underline{\underline{\Theta}}^{-\frac{1}{2}} \tag{II.101}$$

with

$$\underline{\underline{\mathrm{L}}}(t=0) = \underline{\underline{0}} \tag{II.102}$$

Thus, the new thermodynamic conjugate force corresponding to $\underline{\underline{\mathrm{L}}}$ can be simply expressed as

$$\underline{\underline{a}} = \frac{1}{2}\underline{\underline{\Theta}}^{\frac{1}{2}} \cdot \underline{\underline{\mathrm{w}}} \cdot \underline{\underline{\Theta}}^{\frac{1}{2}} = \frac{1}{2}\tilde{\underline{\underline{\sigma}}} \cdot \tilde{\underline{\underline{\epsilon}}} \tag{II.103}$$

Note that, this conjugate force has the same principle axes as $\tilde{\underline{\underline{\sigma}}}$ and $\tilde{\underline{\underline{\epsilon}}}$. Its principal values are equal to

$$a_i = \frac{1}{2}\tilde{\sigma}_i\, \tilde{\epsilon}_i \text{ (no summation)}, \quad i = 1,2,3 \tag{II.104}$$

In addition, its first invariant is equal to the elastic stored energy

$$\mathrm{tr}(\underline{\underline{a}}) = \frac{1}{2}\tilde{\underline{\underline{\sigma}}} : \tilde{\underline{\underline{\epsilon}}} = \frac{1}{2}\underline{\underline{\sigma}} : \underline{\underline{\epsilon}} \tag{II.105}$$

It is noteworthy that for isotropic damage $\dot{\underline{\underline{\mathrm{L}}}} = \dot{\ell}\, \underline{\underline{\mathrm{I}}}$, the thermodynamic force conjugated to ℓ is the stored energy $\mathrm{tr}(\underline{\underline{a}})$.

With these considerations, inequality (II.93) becomes

$$\underline{\underline{\mathrm{w}}} : \dot{\underline{\underline{\Theta}}} = \underline{\underline{a}} : \dot{\underline{\underline{\mathrm{L}}}} \geq 0 \tag{II.106}$$

As mentioned above, the only restriction to formulate evolution laws is that the second law of thermodynamics must be fulfilled, i.e. that the dissipation inequality (II.106) must be fulfilled.
As given by Eq. (II.103), $\underline{\underline{a}}$ does not distinguish between tension and compression, which is a fundamental aspect of quasi-brittle material's behaviour. In order to handle this restriction, Carol et al (2001) propose to redefine the conjugate force as follows

$$\underline{\underline{a}} = \frac{1}{2}\langle\, \tilde{\underline{\underline{\sigma}}}\, \rangle . \langle\, \tilde{\underline{\underline{\epsilon}}}\, \rangle \tag{II.107}$$

It is clear from Eq. II.107 that the principal values a_k of $\underline{\underline{a}}$ are positive.

Finally, with these considerations, we introduce the following damage evolution law

$$\dot{\underline{\underline{\mathrm{L}}}} = \sum_{k=1}^{3} \dot{\lambda}_d(a_k)\, \tilde{\vec{n}}_k \otimes \tilde{\vec{n}}_k \tag{II.108}$$

where $\tilde{\vec{n}}_k$ are the principal directions of $\underline{\underline{a}}$. For the plastic multiplier, we will use a similar definition of that used in the viscoplastic compression model

$$\dot{\lambda}_d(a_k) = v_d \left[1 - \exp\left(-\left\langle \frac{a_k}{R_d} - 1 \right\rangle^{n_d}\right)\right] \tag{II.109}$$

where v_d, R_d and n_d are material parameters. v_d represents the maximum damage rate associated with the material microcracking.
Using evolution law given by Eq. (II.108), and noting that $x\dot{\lambda}_d(x) \geq 0 \quad \forall x \in \mathbb{R}^+$, we can prove easily that inequality (II.106) is satisfied:

$$\underline{\underline{a}} : \dot{\underline{\underline{\mathrm{L}}}} = \sum_{k=1}^{3} a_k \tilde{\vec{n}}_k \otimes \tilde{\vec{n}}_k : \sum_{k=1}^{3} \dot{\lambda}_d(a_k) \tilde{\vec{n}}_k \otimes \tilde{\vec{n}}_k = \sum_{k=1}^{3} a_k \dot{\lambda}_d(a_k) \geq 0 \tag{II.110}$$

II.4.3 Coupled response of the elasto-viscoplastic and the rate dependent damage models

In this section, we try to link the independent models developed earlier. As the first step, we assume the additive decomposition of the total nominal strain tensor

$$\underline{\underline{\epsilon}} = \underline{\underline{\epsilon}}^e + \underline{\underline{\epsilon}}^{vp} \tag{II.111}$$

Since the elasto-viscoplastic response of the damaged material is considered here, the Helmholtz specific free energy can be given as follows

$$\psi = \psi\left(\underline{\underline{\epsilon}},\ \underline{\underline{\Theta}},\ \xi,\ \underline{\underline{\epsilon}}^{vp}\right) \tag{II.112}$$

where ξ characterize the isotropic softening in viscoplasticity and $\underline{\underline{\Theta}}$ characterize the anisotropic damage. Once again, we assume that ψ is independent of the internal scalar variable ξ and is supposed to be written in the following form

$$\psi\left(\underline{\underline{\epsilon}},\ \underline{\underline{\Theta}},\ \xi,\ \underline{\underline{\epsilon}}^{vp}\right) = \frac{1}{2\rho}\underline{\underline{\epsilon}}^e : \underline{\underline{\underline{\underline{\mathrm{H}}}}}\left(\underline{\underline{\Theta}}\right) : \underline{\underline{\epsilon}}^e \tag{II.113}$$

On the other hand, the relation between effective stress $\underline{\underline{\tilde{\sigma}}}$ and effective elastic strain $\underline{\underline{\tilde{\epsilon}}}^e$, which describes the constitutive behaviour of the undamaged material, is assumed to be expressed as

$$\underline{\underline{\tilde{\sigma}}} = \underline{\underline{\underline{\underline{\mathrm{H}}}}}_0 : \underline{\underline{\tilde{\epsilon}}}^e = 2\mu\underline{\underline{\tilde{\epsilon}}}^e + \lambda \mathrm{tr}(\underline{\underline{\tilde{\epsilon}}}^e)\underline{\mathrm{I}} \tag{II.114}$$

The relation between nominal stress $\underline{\underline{\sigma}}$ and nominal elastic strain $\underline{\underline{\epsilon}}^e$ describes the constitutive behaviour of the damaged material

$$\underline{\underline{\sigma}} = \underline{\underline{\underline{\underline{\mathrm{H}}}}}\left(\underline{\underline{\Theta}}\right) : \underline{\underline{\epsilon}}^e \tag{II.115}$$

The effective stress tensor is related to the nominal stress tensor by Eq. (II.81). The energy equivalence approach allows us to find the relationship between the effective elastic strain tensor and the nominal elastic strain tensor

$$\underline{\underline{\tilde{\epsilon}}}^e = \underline{\underline{\Theta}}^{-\frac{1}{2}} \,.\, \underline{\underline{\epsilon}}^e \,.\, \underline{\underline{\Theta}}^{-\frac{1}{2}} \tag{II.116}$$

Finally, the Claussius-Duhem dissipation inequality (II.23) becomes, in this case

$$\underline{\underline{\sigma}} : \dot{\underline{\underline{\epsilon}}}^{vp} + \underline{\underline{a}} : \dot{\underline{\underline{\mathrm{L}}}} \geq 0 \tag{II.117}$$

where $\underline{\underline{a}}$ can take the following new from

$$\underline{\underline{a}} = \frac{1}{2} \langle\, \underline{\underline{\tilde{\sigma}}} \,\rangle . \langle\, \underline{\underline{\tilde{\epsilon}}}^{e} \,\rangle \tag{II.118}$$

It is noteworthy that the last inequality is the sum of the viscoplastic dissipation (II.72) and the damage dissipation (II.110). Thus, if we consider the evolution laws of $\underline{\underline{\epsilon}}^{vp}$ and $\underline{\underline{L}}$ given respectively by Eq. (II.71) and Eq. (II.108), inequality (II.117) will be respected.

Let us now reintroduce the inelastic strain tensor $\underline{\underline{\epsilon}}^{in}$ such that

$$\underline{\underline{\sigma}} = \underline{\underline{\underline{\underline{H}}}}_0 : \left(\underline{\underline{\epsilon}} - \underline{\underline{\epsilon}}^{in} \right) \tag{II.119}$$

Using Eq. (II.111) together with Eq. (II.115) and Eq. (II.119), one can easily obtain

$$\underline{\underline{\epsilon}}^{in} = \underline{\underline{\epsilon}} - \underline{\underline{\underline{\underline{H}}}}_0^{-1} : \underline{\underline{\underline{\underline{H}}}} \left(\underline{\underline{\Theta}} \right) : \left(\underline{\underline{\epsilon}} - \underline{\underline{\epsilon}}^{vp} \right) \tag{II.120}$$

II.4.4 Stiffness recovery

The previous model presumes that damage is always active, i.e. damage continues to grow whether the micro-cracks are open or closed. However, it is obvious that damage is promoted mainly in the tensile stress regime, whereas compressive stresses tend to close the micro-cracks. This scenario motivates the introduction of a unilateral condition, i.e. the active/passive condition, due to the micro-crack-closure-reopening effect.
A common approach in literature for discerning the different response in tension and compression is to extract the tensile stresses or strains by introducing projection operators (Ortiz, 1985). In this study, we select a second-order projection operator defined as

$$\underline{\underline{P}} = \sum_{k=1}^{3} \mathscr{H}(\sigma_k) \overrightarrow{n}_k \otimes \overrightarrow{n}_k \tag{II.121}$$

where $\mathscr{H}$ is the Heaviside function. σ_k are the principal values of the stress tensor and $\overrightarrow{n}_k$ are its principal directions.
Using this projection operator, we define an active damage tensor as follows

$$\underline{\underline{\Theta}}^{ac} = \underline{\underline{I}} + \underline{\underline{P}} \left[\, \underline{\underline{\Theta}} - \underline{\underline{I}} \, \right] \underline{\underline{P}} \tag{II.122}$$

After this definition, three basic properties of $\underline{\underline{\Theta}}^{ac}$ can be mentioned

1. For undamaged state: $\underline{\underline{\Theta}}^{ac} = \underline{\underline{\Theta}} = \underline{\underline{I}}$
2. For triaxial compression $\left(\underline{\underline{P}} = \underline{\underline{0}} \right)$: $\underline{\underline{\Theta}}^{ac} = \underline{\underline{I}}$
3. For triaxial tension $\left(\underline{\underline{P}} = \underline{\underline{I}} \right)$: $\underline{\underline{\Theta}}^{ac} = \underline{\underline{\Theta}}$

In order to avoid computational difficulties associated with the use of the Heaviside function, we suggest to replace $\mathscr{H}$ by the following smooth function

$$h(x) = \frac{1}{2} + \frac{1}{\pi} \arctan \left(\frac{x - x_0}{\kappa} \right), \quad \kappa > 0 \tag{II.123}$$

where x_0 and κ are monitoring parameters.

II.5 Integration of constitutive equations

Let $\overrightarrow{x} \in \Omega$ be a given point of interest in the body. At this point, the local state of the body can be described by the rate dependent constitutive model which can be written as the following

$$\begin{cases} \underline{\underline{\sigma}} = \underline{\underline{\underline{\underline{H}}}}\left(\underline{\underline{\Theta}}^{ac}\right)\left(\underline{\underline{\epsilon}} - \underline{\underline{\epsilon}}^{vp}\right) = \sum_{k=1}^{3} \sigma_k \overrightarrow{n}_k \otimes \overrightarrow{n}_k \\ \underline{\underline{\Theta}}^{ac} = \underline{\underline{I}} + \underline{\underline{P}}\left[\ \underline{\underline{\Theta}} - \underline{\underline{I}}\ \right]\underline{\underline{P}}, \quad \underline{\underline{P}} = \sum_{k=1}^{3} h(\sigma_k)\overrightarrow{n}_k \otimes \overrightarrow{n}_k \\ \dot{\underline{\underline{\Theta}}} = \underline{\underline{f}}\left(\underline{\underline{\sigma}},\ \underline{\underline{\Theta}}\right) \\ \dot{\underline{\underline{\epsilon}}}^{vp} = \underline{\underline{g}}\left(\underline{\underline{\sigma}},\ \xi\right) \\ \dot{\xi} = \hbar\left(\underline{\underline{\sigma}},\ \xi\right) \end{cases} \tag{II.124}$$

Here, $\underline{\underline{f}},\ \underline{\underline{g}},\ \hbar$ are known functions.

II.5.1 Numerical integration: basic principles

The solution of the constitutive problem is carried out by subdividing the time interval into a finite number of time steps

$$[0,\ T] = \bigcup_{n=0}^{N} [t_n,\ t_{n+1}] \tag{II.125}$$

The unknown functions are substituted by the algorithmic values assumed at the beginning and at the end of the time steps so that the original problem is reduced to subsequent solutions of finite step problems.
At time t_n, we assume that the local state of the body at point $\overrightarrow{x}$ is completely defined. By this statement we mean that the value of

$$\left\{\underline{\underline{\epsilon}}_n,\ \underline{\underline{\Theta}}^{ac}_n,\ \xi_n,\ \underline{\underline{\epsilon}}^{vp}_n\right\} \tag{II.126}$$

are known and, therefore, the stress state

$$\underline{\underline{\sigma}}_n = \underline{\underline{\underline{\underline{H}}}}\left(\underline{\underline{\Theta}}^{ac}_n\right) : \left(\underline{\underline{\epsilon}}_n - \underline{\underline{\epsilon}}^{vp}_n\right) \tag{II.127}$$

is also known. The basic problem we shall be concerned with is the update of the fields (II.126) to time $t_{n+1} = t_n + \Delta t$ in a manner consistent with the constitutive model.

Before writing the discrete form of the evolution laws, let us firstly review a classical family of schemes for numerical integration of ordinary differential equations.

Let $\chi : \mathbb{R} \to \mathbb{R}$ be a smooth function, and consider the initial-value problem

$$\left.\begin{array}{l} \dot{x}(t) = \chi\left(x(t)\right) \\ x(0) = x_0 \end{array}\right\} \quad \text{in } [0,\ T] \tag{II.128}$$

We shall be concerned with the following one-parameter class of integration algorithms called the generalized midpoint rule

$$\begin{cases} x_{n+1} = x_n + \Delta t \chi(x_{n+\vartheta}) \\ x_{n+\vartheta} = \vartheta x_{n+1} + (1-\vartheta)x_n; \qquad \vartheta \ \in\ [0,\ 1] \end{cases} \tag{II.129}$$

Here, $x_{n+1} \cong x(t_{n+1})$ denotes the algorithmic approximation of the exact value $x(t_{n+1})$ at time $t_{n+1} = t_n + \Delta t$. We note that this family of algorithms contains well-known integrative shemes, in particular,

$$\begin{cases} \vartheta = 0 & \Rightarrow \text{ explicit integration sheme (forward Euler)} \\ \vartheta = \frac{1}{2} & \Rightarrow \text{ midpoint integration sheme} \\ \vartheta = 1 & \Rightarrow \text{ implicit integration sheme (backward Euler)} \end{cases} \tag{II.130}$$

Given the complexity of the constitutive relations and their aim which is to model quasi-brittle materials in fast dynamics, we have chosen to implement an explicit sheme because time integration needs to be extremely fast in 3D transient dynamics where time increments are very small and where the number of degree of freedom is very high. In addition, we assume that the strain tensor can be kept constant within an increment. This method, referred to as *relaxation method*, was tested and it was shown that it gives accurate results.
The stress state used in the numerical calculations is that given by Eq. (II.119). Therefore, by using relaxation method, the inelastic strain tensor given by Eq. (II.120) can be expressed at time t_{n+1} as

$$\underline{\underline{\epsilon}}^{in}_{n+1} = \underline{\underline{\epsilon}}_n - \underline{\underline{\underline{\underline{\mathrm{H}}}}}_0^{-1} : \underline{\underline{\underline{\underline{\mathrm{H}}}}} \left(\underline{\underline{\Theta}}^{ac}_{n+1} \right) : \left(\underline{\underline{\epsilon}}_n - \underline{\underline{\epsilon}}^{vp}_{n+1} \right) \tag{II.131}$$

where $\left\{ \underline{\underline{\Theta}}^{ac}_{n+1},\ \xi_{n+1},\ \underline{\underline{\epsilon}}^{vp}_{n+1} \right\}$ can be given by

$$\begin{cases} \underline{\underline{\Theta}}^{ac}_{n+1} = \underline{\underline{\Theta}}^{ac}_n + \Delta t\ \underline{\underline{f}} \left(\underline{\underline{\sigma}}_n,\ \underline{\underline{\Theta}}^{ac}_n \right) \\ \underline{\underline{\epsilon}}^{vp}_{n+1} = \underline{\underline{\epsilon}}^{vp}_n + \Delta t\ \underline{\underline{g}} \left(\underline{\underline{\sigma}}_n,\ \xi_n \right) \\ \xi_{n+1} = \ \xi_n + \Delta t\ \hbar \left(\underline{\underline{\sigma}}_n,\ \xi_n \right) \end{cases} \tag{II.132}$$

Finally, this present algorithm has been implemented in a transient dynamic finite element code VIPLEF3D. In this numerical tool, the time derivative, arising in the local form of the momentum equations, is replaced by the well-known Newmark algorithm. Large strain computation was taken into account by decomposing the body motion into small steps and by updating not only the body's geometry but also the stress state.

II.5.2 Uniaxial computational results

Due to the lack of data for material behaviour under high hydrostatic pressure, we will use, for the sake of simplicity, a Mohr coulomb failure criterion and a Drucker-Prager potential function in the elasto-viscoplastic model.
Values of material parameters are given in chapter III.

II.5.2.1 Uniaxial tension test

Fig. II.17 shows the response of the model in uniaxial tension test carried out at constant strain rate. Upon unloading, the material returns to its initial stress and strain free state; no permanent (plastic) strain occurs. Fig. II.18 shows the response of the model in uniaxial tension tests carried out at various strain rates. As can be seen, the response is dependent upon the strain rate.
In Fig. II.19 the Dynamic Increase Factor (DIF), i.e. the ratio of the dynamic to static strength, is reported, in a semi-log plot, as a function of strain rate. These results are in agreement with experiments.

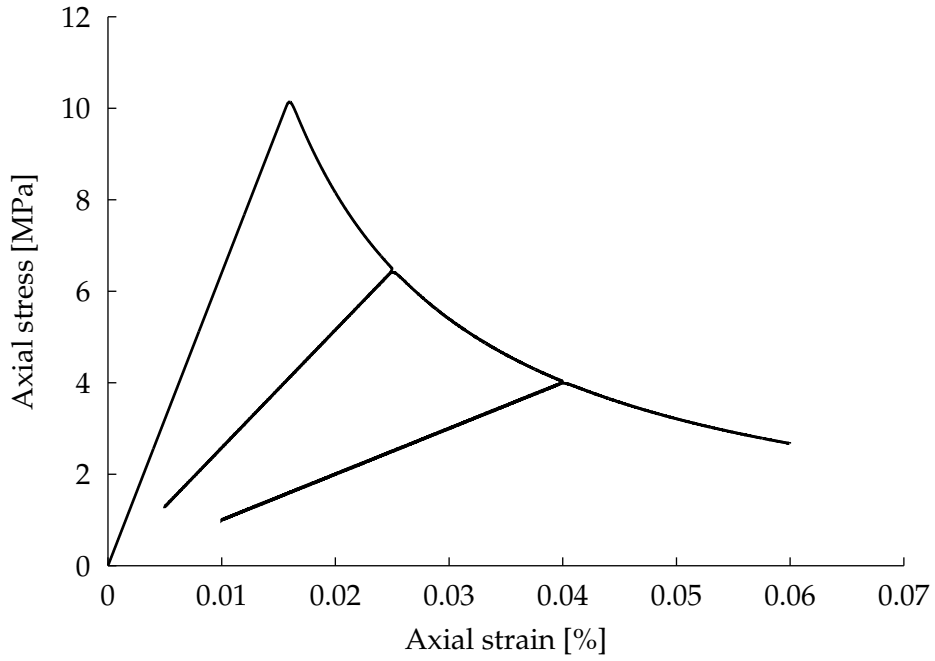

Figure II.17: Model response for uniaxial tension test

II.5.2.2 Uniaxial compression test

Fig. II.20 shows the response of the present model in a uniaxial compression test carried out at a constant strain rate. The unloading-reloading line does not change with plastic deformation. Fig. II.21 shows the response of the model in uniaxial compression tests carried out at various strain rates. In Fig. II.22 the Dynamic Increase Factor (DIF) is reported, in a semi-log plot, as function of strain rate. These results are also in agreement with experiments.

II.5.2.3 Cyclic uniaxial tension/compression test

Fig. II.23 illustrates the applied strain-time curve. The result of this loading is reported in Fig. II.24. As shown, damage controls the response under tension, while plasticity is active under compression. Under tension regime the material unloads at the degraded secant stiffness. Under compressive regime the elastic stiffness is recovered simulating the closing of micro-cracks. Once the compressive stress exceeds the yield stress, the material exhibits softening plastic response. Upon reversing the strain path, the stress follows the elastic response with the undamaged secant stiffness. When the loading cycle is back to tension, the degraded secant stiffness is recovered, simulating the re-opening of the micro-cracks.

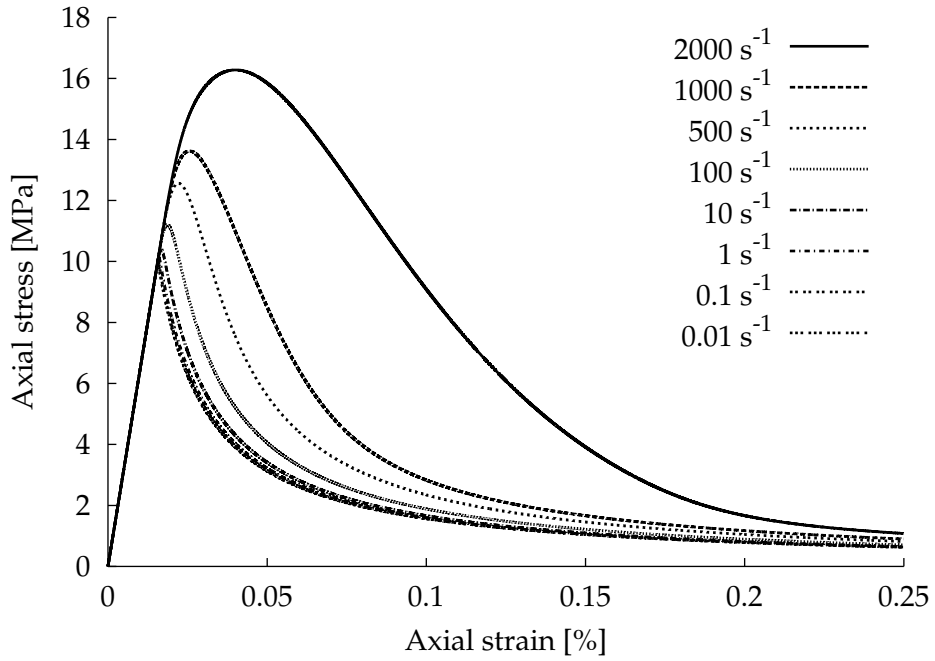

Figure II.18: Model response for several strain rates in uniaxial tension test

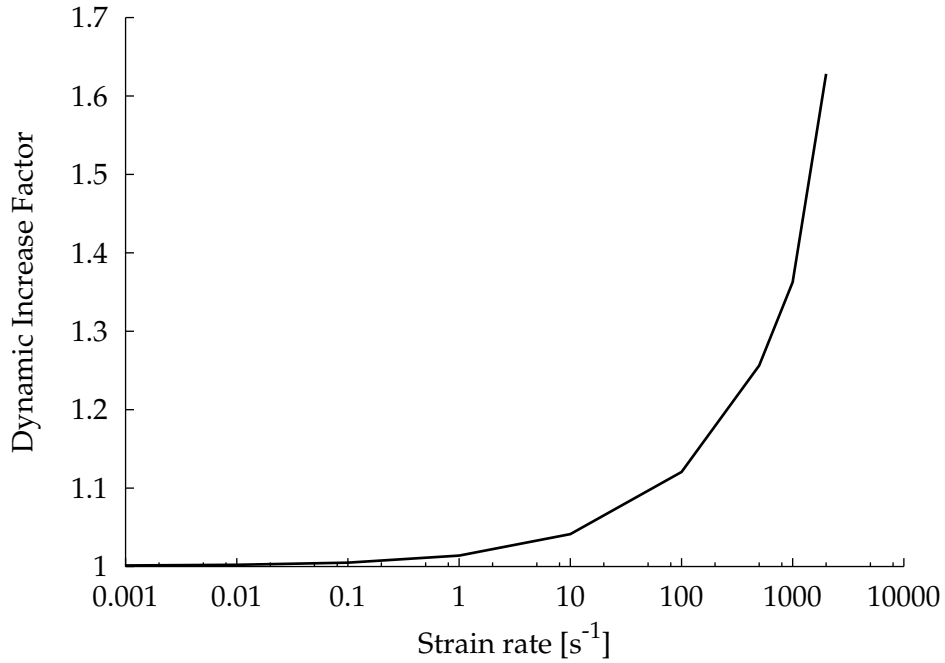

Figure II.19: Dynamic increase factor in tension

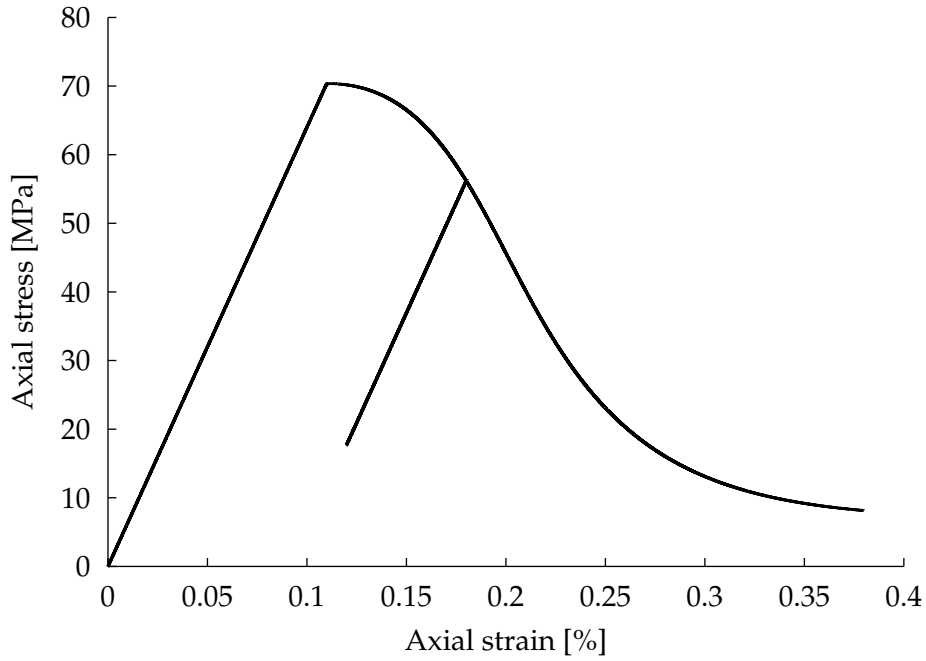

Figure II.20: Model response for uniaxial compression test

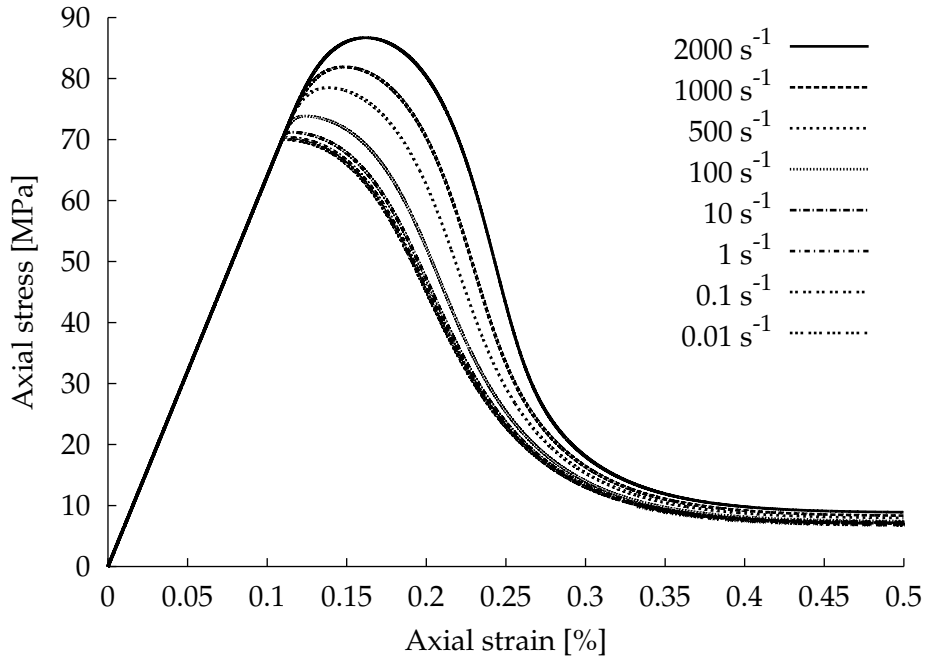

Figure II.21: Model response for several strain rates in uniaxial compression test

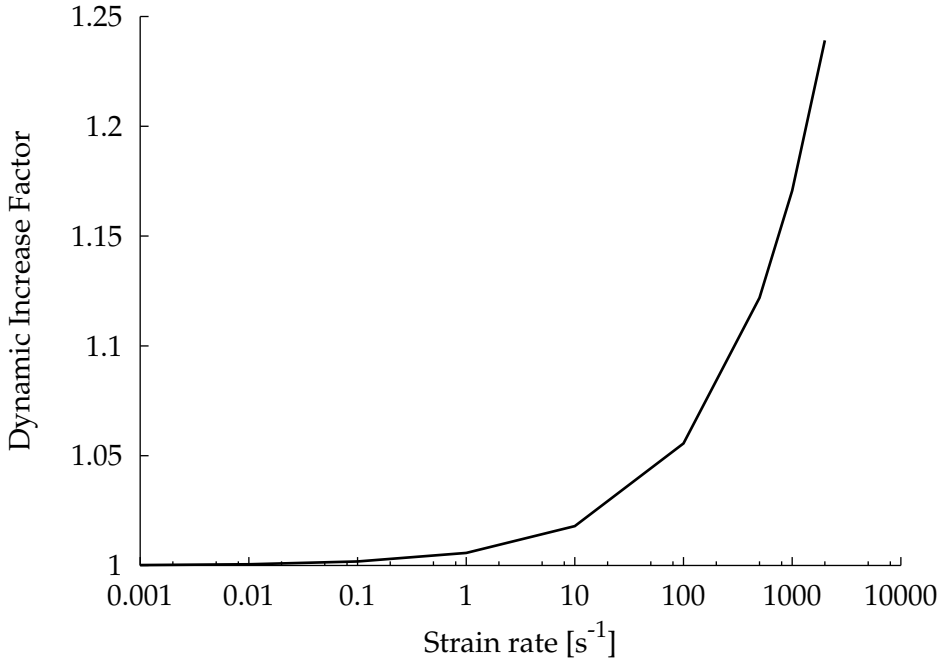

Figure II.22: Dynamic increase factor in compression

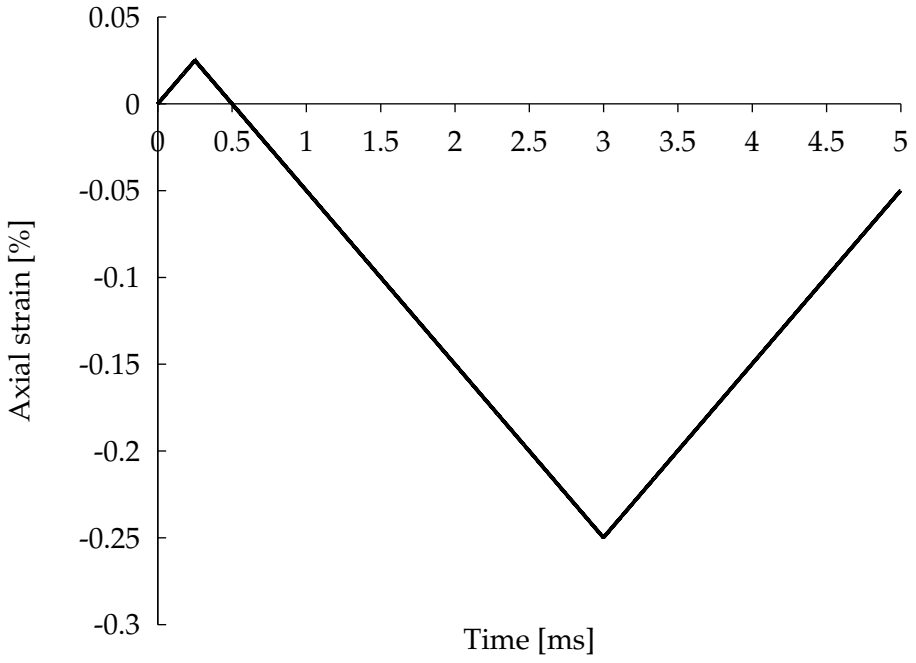

Figure II.23: Applied strain in cyclic uniaxial tension/compression

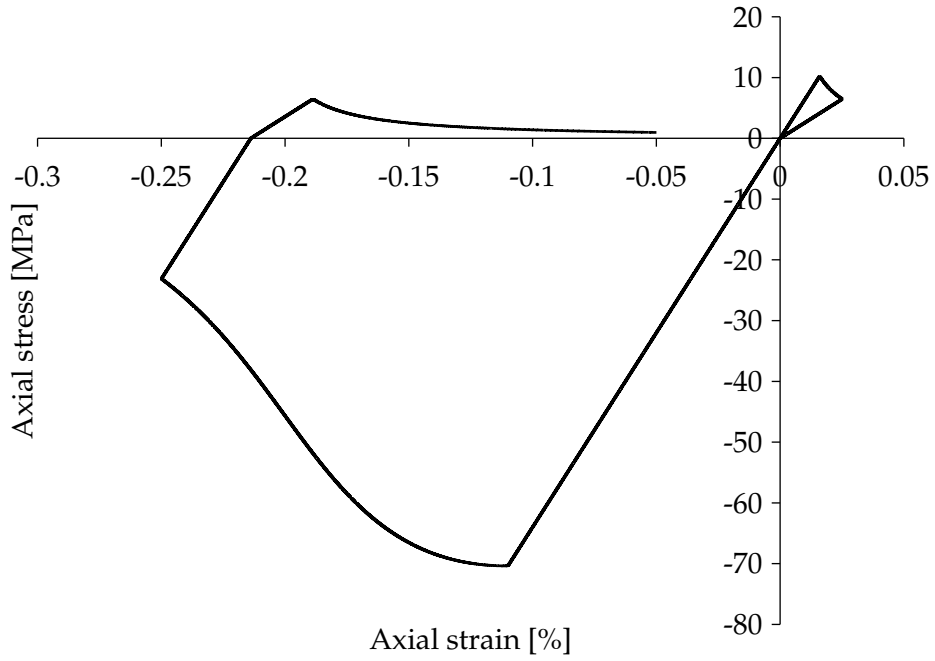

Figure II.24: Model response for cyclic uniaxial tension/compression

II.6 Localisation problem in dynamic fracture

In many structures subjected to extreme loading conditions, the initially smooth distribution of strain changes into a highly localized one. Typically, the deformation is trapped in narrow band in which the strain can grow unboundedly. Nonlocal models (Engelen et al, 2003; Peerlings et al, 2001) and rate-dependent models are among the continuous approaches proposed to regularize the localization problems. Here our attention will be focused on the second class of models. Failure predictions of rate-independent plasticity are analysed and compared with the rate-dependent one.

The mechanical response of quasi-brittle material such as rocks and concrete is strongly non-linear. As consequence, the constitutive functional $\mathscr{F}$ used in section II.2 to define the stress state must be non linear. However, working with non linear functionals poses formidable problems, even in the simplest cases. An alternative strategy, which overcomes this difficulty and is commonly used in the non-linear mechanics, is to adopt an incrimental (or rate-type) formulation in which the stress state is given as a function of the deformation rate and the current thermodynamic state of the material. For small deformation theory, $\dot{\underline{\underline{\sigma}}}$ can be written as

$$\dot{\underline{\underline{\sigma}}} = \mathscr{G}\left(\underline{\underline{\sigma}},\ \boldsymbol{\xi}_k,\ \dot{\underline{\underline{\epsilon}}}\right) \tag{II.133}$$

If the constitutive function $\mathscr{G}$ is linear in $\dot{\underline{\underline{\epsilon}}}$, then the material is said to be incrementaly linear. In this case, $\dot{\underline{\underline{\sigma}}}$ can be expressed as

$$\dot{\underline{\underline{\sigma}}} = \underline{\underline{\underline{\underline{\mathrm{E}}}}}\left(\underline{\underline{\sigma}},\ \boldsymbol{\xi}_k\right) : \dot{\underline{\underline{\epsilon}}} \tag{II.134}$$

Here, $\underline{\underline{\underline{\underline{\mathrm{E}}}}}$ is the tangent stiffness tensor. We will see below that we can identify its expression for both rate-independent and rate-dependent plasticity theory [1].

[1] For rate-independent formulation, a change in the time scale does not affect the material response, which implies

$$\forall\ \lambda \in \mathbb{R}^+\ : \mathscr{G}\left(\underline{\underline{\sigma}},\ \boldsymbol{\xi}_k,\ \lambda\dot{\underline{\underline{\epsilon}}}\right) = \lambda\mathscr{G}\left(\underline{\underline{\sigma}},\ \boldsymbol{\xi}_k,\ \dot{\underline{\underline{\epsilon}}}\right)$$

If we assume that $\underline{\underline{\underline{\underline{\mathrm{E}}}}}$ obey the minor symmetry conditions

$$\mathrm{E}_{ijkl} = \mathrm{E}_{jikl} = \mathrm{E}_{ijlk}, \tag{II.135}$$

then, Eq. (II.134) can also be expressed as

$$\dot{\underline{\underline{\sigma}}} = \underline{\underline{\underline{\underline{\mathrm{E}}}}} \left(\underline{\underline{\sigma}},\ \boldsymbol{\xi}_k \right) : \dot{\underline{\underline{\epsilon}}} = \underline{\underline{\underline{\underline{\mathrm{E}}}}} \left(\underline{\underline{\sigma}},\ \boldsymbol{\xi}_k \right) : \underline{\underline{\nabla}} \overrightarrow{v} \tag{II.136}$$

Now, with Eq. (II.136) in hand, we will focus on the condition for localization. From Eq. (II.4), the equation of motion takes the form

$$\overrightarrow{\mathrm{div}} \dot{\underline{\underline{\sigma}}} = \rho \frac{\partial^2 \overrightarrow{v}}{\partial t^2} \quad \text{in } \Omega \times [0,\ T] \tag{II.137}$$

Here, the body force $\overrightarrow{f}$ is assumed to be time independent.
Thus, the use of Eq. (II.136) and (II.137) renders

$$\overrightarrow{\mathrm{div}} \left[\underline{\underline{\underline{\underline{\mathrm{E}}}}} : \underline{\underline{\nabla}} \overrightarrow{v} \right] = \rho \frac{\partial^2 \overrightarrow{v}}{\partial t^2} \quad \text{in } \Omega \times [0,\ T] \tag{II.138}$$

To carry our analysis further we need to make an additional assumption about the stiffness tensor. We assume that it is independent of the position vector $\overrightarrow{x}$ and can be given at a homegeneous reference state $\left(\underline{\underline{\sigma}}^0,\ \boldsymbol{\xi}_k^0 \right)$, i.e.,

$$\underline{\underline{\underline{\underline{\mathrm{E}}}}} \left(\underline{\underline{\sigma}}(\overrightarrow{x},\ t),\ \boldsymbol{\xi}_k(\overrightarrow{x},\ t) \right) = \underline{\underline{\underline{\underline{\mathrm{E}}}}} \left(\underline{\underline{\sigma}}^0(t),\ \boldsymbol{\xi}_k^0(t) \right) \quad \forall \overrightarrow{x} \in \Omega \tag{II.139}$$

With such an assumption in hand, one of general forms of the solution to Eq. (II.138) can be written as

$$\overrightarrow{v}(\overrightarrow{x},\ t) = \overrightarrow{v}_0\ f\left(\overrightarrow{n}.\overrightarrow{x} - ct \right) \tag{II.140}$$

where $\overrightarrow{v}_0$ is the velocity at $\overrightarrow{x} = \overrightarrow{0}$ and $t = 0$, c the wave speed, $\overrightarrow{n}$ the unit normal to the wave front, and f is a scalar function. Substituting Eq. (II.140) into (II.138), we obtain

$$\underline{\underline{\mathscr{C}}}(\overrightarrow{n}) \overrightarrow{v}_0 = \rho c^2 \overrightarrow{v}_0 \tag{II.141}$$

with

$$\underline{\underline{\mathscr{C}}}(\overrightarrow{n}) = \overrightarrow{n}.\ \underline{\underline{\underline{\underline{\mathrm{E}}}}}\ .\overrightarrow{n} \tag{II.142}$$

$\underline{\underline{\mathscr{C}}}(\overrightarrow{n})$ is the so-called accoustic tensor. It can be seen from Eq. (II.141) that the wave speed is proportional to the eigenvalues of the acoustic tensor. As consequence, a spatial discontinuity will be formed when the acoustic tensor becomes singular in some direction. Thus, the condition for localization can be given by

$$\det \underline{\underline{\mathscr{C}}}(\overrightarrow{n}) = 0 \tag{II.143}$$

From a numerical point of view, a singularity of the acoustic tensor corresponds to the lost of the hyperbolicity of the Initial Boundary-Value Problem which causes severe mesh-dependence.

In what follows, our attention will be focused on the formulation of the tangent stiffness tensor for both elasto-plastic and the Perzyna viscoplasticity formulations.
For this purpose, we will use the linear elasticity framework,

$$\dot{\underline{\underline{\sigma}}} = \underline{\underline{\underline{\underline{\mathrm{H}}}}} : \dot{\underline{\underline{\epsilon}}}^e \tag{II.144}$$

where $\underline{\underline{\underline{\underline{\mathrm{H}}}}}$ is the constant elasticity tensor obeying the major symmetry conditions

$$\mathrm{H}_{ijkl} = \mathrm{H}_{klij} = \mathrm{H}_{jikl} = \mathrm{H}_{ijlk} \tag{II.145}$$

In other words, the function $\mathscr{G}$ is homogeneous of degree one in $\dot{\underline{\underline{\epsilon}}}$ (in a way restricted to the positive value of λ).

II.6.1 The elasto-plastic tangent stiffness tensor

Irreversibility is introduced by requiring that the state of the material $\left(\underline{\underline{\sigma}},\ \boldsymbol{\xi}_k\right) \in \mathbb{E}$. If $\mathbf{F}\left(\underline{\underline{\sigma}},\ \boldsymbol{\xi}_k\right) < 0$, the response is instantaneously elastic:

$$\dot{\underline{\underline{\sigma}}} = \underline{\underline{\underline{\underline{\mathrm{H}}}}} : \dot{\underline{\underline{\epsilon}}} \tag{II.146}$$

Now, suppose that $\left(\underline{\underline{\sigma}},\ \boldsymbol{\xi}_k\right) \in \partial\mathbb{E}$ which implies that $\mathbf{F}\left(\underline{\underline{\sigma}},\ \boldsymbol{\xi}_k\right) = 0$. According to the consistency condition (II.33) and to the expression (II.28) and (II.71), one can find, when using the chain rule, that

$$\dot{\mathbf{F}}(\underline{\underline{\sigma}},\ \boldsymbol{\xi}_k) = \frac{\partial \mathbf{F}}{\partial \underline{\underline{\sigma}}} : \underline{\underline{\underline{\underline{\mathrm{H}}}}} : \dot{\underline{\underline{\epsilon}}} - \dot{\gamma}\left[\frac{\partial \mathbf{F}}{\partial \underline{\underline{\sigma}}} : \underline{\underline{\underline{\underline{\mathrm{H}}}}} : \underline{\underline{m}} - \frac{\partial \mathbf{F}}{\partial \boldsymbol{\xi}_k}\boldsymbol{\ell}_k\right] \leq 0 \tag{II.147}$$

Introducing the scalar hardening/softening modulus of the material

$$\bar{\mathrm{H}}\left(\underline{\underline{\sigma}},\ \boldsymbol{\xi}_k\right) = -\frac{\partial \mathbf{F}}{\partial \boldsymbol{\xi}_k}\boldsymbol{\ell}_k \tag{II.148}$$

A positive value of $\bar{\mathrm{H}}$ denotes hardening, a negative value indicates softening, while $\bar{\mathrm{H}} = 0$ characterize perfect plasticity.
In order to carry our development further we need to assume that

$$\bar{\mathrm{K}}\left(\underline{\underline{\sigma}},\ \boldsymbol{\xi}_k\right) = \frac{\partial \mathbf{F}}{\partial \underline{\underline{\sigma}}} : \underline{\underline{\underline{\underline{\mathrm{H}}}}} : \underline{\underline{m}} + \bar{\mathrm{H}} > 0 \tag{II.149}$$

Such an assumption is crucial in the establishement of the correct formulation of the loading/unloading conditions in presence of softening [2].
With these considerations in mind, it follows from the consistency condition that

$$\dot{\gamma} = \frac{1}{\bar{\mathrm{K}}}\left(\frac{\partial \mathbf{F}}{\partial \underline{\underline{\sigma}}} : \underline{\underline{\underline{\underline{\mathrm{H}}}}} : \dot{\underline{\underline{\epsilon}}}\right) \tag{II.150}$$

Finally, according to the additive decomposition of the total strain into an elastic and plastic part, to (II.144), and to (II.71), it follows that

$$\dot{\underline{\underline{\sigma}}} = \underline{\underline{\underline{\underline{\mathrm{H}}}}} : \left(\dot{\underline{\underline{\epsilon}}} - \dot{\underline{\underline{\epsilon}}}^{in}\right) = \underline{\underline{\underline{\underline{\mathrm{H}}}}} : \left(\dot{\underline{\underline{\epsilon}}} - \dot{\gamma}\underline{\underline{m}}\right) \tag{II.151}$$

Then substituting (II.150) in (II.151), we obtain

$$\dot{\underline{\underline{\sigma}}} = \underline{\underline{\underline{\underline{\mathrm{E}}}}}^{ep} : \dot{\underline{\underline{\epsilon}}} \tag{II.152}$$

where $\underline{\underline{\underline{\underline{\mathrm{E}}}}}^{ep}$ is the elasto-plastic stiffness tensor given by

$$\underline{\underline{\underline{\underline{\mathrm{E}}}}}^{ep} = \begin{cases} \underline{\underline{\underline{\underline{\mathrm{H}}}}} & \text{if } \dot{\gamma} = 0, \\ \underline{\underline{\underline{\underline{\mathrm{H}}}}} - \frac{1}{\bar{\mathrm{K}}}\,\underline{\underline{\underline{\underline{\mathrm{H}}}}} : \underline{\underline{m}} \otimes \frac{\partial \mathbf{F}}{\partial \underline{\underline{\sigma}}} : \underline{\underline{\underline{\underline{\mathrm{H}}}}} & \text{if } \dot{\gamma} > 0 \end{cases} \tag{II.153}$$

Note that, due to the non-associativeness of the flow rule, the stiffness tensor does not possess major symmetry.

[2] For hardening or perfect plasticity, characterized by $\bar{\mathrm{H}} \geq 0$, $\bar{\mathrm{K}}$ is always > 0 when the flow rule is associative, i.e. $\underline{\underline{m}} = \frac{\partial \mathbf{F}}{\partial \underline{\underline{\sigma}}}$. This conclusion is the result of the positive definiteness of the elasticity tensor.

Following the above considerations, the acoustic tensor, in this particular case, can take the form

$$\underline{\underline{\mathscr{C}}} = \underline{\underline{\mathscr{C}}}\left(\overrightarrow{n},\ \bar{\mathrm{H}}\right) \tag{II.154}$$

In this equation, the dependence, for a given thermodynamic state, of the acoustic tensor on the normal $\overrightarrow{n}$ and the hardening/softening modulus is emphasized. In addition, let $\mathscr{Z}$ be the set of values of $\bar{\mathrm{H}}$ for which $\underline{\underline{\mathscr{C}}}$ becomes singular in some direction $\overrightarrow{n}$:

$$\mathscr{Z} = \left\{\bar{\mathrm{H}} \in \mathbb{R} \mid \exists \overrightarrow{n} \in \mathbb{R}^3\ ;\ ||\overrightarrow{n}|| = 1\ ;\ \det\left[\underline{\underline{\mathscr{C}}}\left(\overrightarrow{n},\ \bar{\mathrm{H}}\right)\right] = 0\right\} \tag{II.155}$$

If $\mathscr{Z} \neq \emptyset$, one can choose the critical hardening/softening modulus defining the localization as the maximum one belonging to $\mathscr{Z}$:

$$\bar{\mathrm{H}}_{cr} = \max\left[\bar{\mathrm{H}} \in \mathscr{Z}\right] \tag{II.156}$$

The corresponding direction $\overrightarrow{n}_{cr}$ define the possible direction of propagation of the discontinuity

$$\overrightarrow{n}_{cr} \in \left\{\overrightarrow{n} \in \mathbb{R}^3\ ;\ ||\overrightarrow{n}|| = 1\ ;\ \det\left[\underline{\underline{\mathscr{C}}}\left(\overrightarrow{n},\ \bar{\mathrm{H}}_{cr}\right)\right] = 0\right\} \tag{II.157}$$

II.6.2 The Perzyna elasto-viscoplastic tangent stiffness tensor

For deriving the tangent stiffness tensor of the Perzyna viscoplasticity, the flow rule is discretized and the solution is analysed over a finite time increment. To this purpose, we consider a typical time increment $[t,\ t+\Delta t]$. We assume that all variables are known at t. For the sake of simplicity, we also assume that the hardening/softening variables will be constant within the time increment. The quantity $\underline{\underline{\epsilon}}^{vp}(t+\Delta t)$, corresponding to the viscoplastic strain at the time $t = t + \Delta t$, is thus given by

$$\underline{\underline{\epsilon}}^{vp}(t+\Delta t) = \underline{\underline{\epsilon}}^{vp}_0 + \int_t^{t+\Delta t} \underline{\underline{\dot{\epsilon}}}^{vp} d\tau = \underline{\underline{\epsilon}}^{vp}_0 + \Delta\underline{\underline{\epsilon}}^{vp} \tag{II.158}$$

where $\underline{\underline{\epsilon}}^{vp}_0 = \underline{\underline{\epsilon}}^{vp}(t)$ and $\Delta\underline{\underline{\epsilon}}^{vp}$ is the viscoplastic strain increment. In this case, we will consider an implicit integration sheme, such that

$$\Delta\underline{\underline{\epsilon}}^{vp} = \Delta\underline{\underline{\epsilon}}^{vp}\left(\underline{\underline{\sigma}}\right) \tag{II.159}$$

where $\underline{\underline{\sigma}} = \underline{\underline{\sigma}}(t+\Delta t)$. Using Eq. (II.28) and (II.37), (II.159) reduces to

$$\underline{\underline{\epsilon}}^{vp} = \underline{\underline{\epsilon}}^{vp}_0 + \frac{\Delta t}{\eta}\varphi(\underline{\underline{\sigma}})\underline{\underline{m}}(\underline{\underline{\sigma}}) \tag{II.160}$$

Now, according to the additive decomposition of the total strain into an elastic and viscoplastic part and using Eq. (II.160), the resulting discrete equation read in stress residual form as

$$\underline{\underline{r}}\left(\underline{\underline{\sigma}},\ \underline{\underline{\epsilon}}\right) = \underline{\underline{\sigma}} - \underline{\underline{\underline{\underline{\mathrm{H}}}}} : \underline{\underline{\epsilon}} + \frac{\Delta t}{\eta}\varphi(\underline{\underline{\sigma}})\underline{\underline{\underline{\underline{\mathrm{H}}}}} : \underline{\underline{m}}(\underline{\underline{\sigma}}) + \underline{\underline{\underline{\underline{\mathrm{H}}}}} : \underline{\underline{\epsilon}}^{vp}_0 = \underline{\underline{0}} \tag{II.161}$$

Here $\underline{\underline{\epsilon}} = \underline{\underline{\epsilon}}(t+\Delta t)$. Linearization of the residual in (II.161) yields

$$\frac{\partial \underline{\underline{r}}}{\partial \underline{\underline{\sigma}}} : d\underline{\underline{\sigma}} + \frac{\partial \underline{\underline{r}}}{\partial \underline{\underline{\epsilon}}} : d\underline{\underline{\epsilon}} = \underline{\underline{0}} \tag{II.162}$$

where the individual terms in (II.162) are

$$\frac{\partial \underline{\underline{r}}}{\partial \underline{\underline{\sigma}}} = \underline{\underline{\underline{\underline{\mathrm{I}}}}}^s + \frac{\Delta t}{\eta}\underline{\underline{\underline{\underline{\mathrm{H}}}}} : \left[\frac{\partial \varphi}{\partial \underline{\underline{\sigma}}} \otimes \underline{\underline{m}} + \varphi\frac{\partial \underline{\underline{m}}}{\partial \underline{\underline{\sigma}}}\right] = \underline{\underline{\underline{\underline{\mathrm{H}}}}} : \left[\underline{\underline{\underline{\underline{\mathrm{H}}}}}^{-1} + \frac{\Delta t}{\eta}\varphi\frac{\partial \underline{\underline{m}}}{\partial \underline{\underline{\sigma}}} + \frac{\Delta t}{\eta}\frac{\partial \varphi}{\partial \underline{\underline{\sigma}}} \otimes \underline{\underline{m}}\right] \tag{II.163}$$

$$\frac{\partial \underline{\underline{r}}}{\partial \underline{\underline{\epsilon}}} = -\underline{\underline{\underline{\underline{\mathrm{H}}}}} \tag{II.164}$$

Thus, substituting (II.163) and (II.164) into (II.162) we obtain

$$d\underline{\underline{\sigma}} = \underline{\underline{\underline{\underline{\mathrm{E}}}}}^{evp} : d\underline{\underline{\epsilon}} \quad \text{with} \quad \underline{\underline{\underline{\underline{\mathrm{E}}}}}^{evp} = \left[\underline{\underline{\underline{\underline{\mathrm{H}}}}}^{-1} + \frac{\Delta t}{\eta}\varphi\frac{\partial \underline{\underline{m}}}{\partial \underline{\underline{\sigma}}} + \frac{\Delta t}{\eta}\frac{\partial \varphi}{\partial \underline{\underline{\sigma}}} \otimes \underline{\underline{m}}\right]^{-1} \tag{II.165}$$

where $\underline{\underline{\underline{\underline{\mathrm{E}}}}}^{evp}$ is the elasto-viscoplastic stiffness tensor.

Finally, by using the Woodbury formula [3], the tangent stiffness tensor of Perzyna viscoplasticity can be expressed as

$$\underline{\underline{\underline{\underline{\mathrm{E}}}}}^{evp} = \underline{\underline{\underline{\underline{\mathrm{A}}}}} - \left[\frac{\eta}{\Delta t} + \underline{\underline{m}} : \underline{\underline{\underline{\underline{\mathrm{A}}}}} : \frac{\partial \varphi}{\partial \underline{\underline{\sigma}}}\right]^{-1} \underline{\underline{\underline{\underline{\mathrm{A}}}}} : \frac{\partial \varphi}{\partial \underline{\underline{\sigma}}} \otimes \underline{\underline{m}} : \underline{\underline{\underline{\underline{\mathrm{A}}}}} \tag{II.166}$$

where

$$\underline{\underline{\underline{\underline{\mathrm{A}}}}} = \left[\underline{\underline{\underline{\underline{\mathrm{H}}}}}^{-1} + \frac{\Delta t}{\eta}\underline{\underline{\underline{\underline{\mathrm{B}}}}}\right]^{-1} \qquad \text{with} \quad \underline{\underline{\underline{\underline{\mathrm{B}}}}} = \varphi\frac{\partial \underline{\underline{\underline{m}}}}{\partial \underline{\underline{\sigma}}} \tag{II.167}$$

It is of interest to note that $\underline{\underline{\underline{\underline{\mathrm{E}}}}}^{evp}$ has the same structure as $\underline{\underline{\underline{\underline{\mathrm{E}}}}}^{ep}$ with $\underline{\underline{\underline{\underline{\mathrm{A}}}}}$ playing the role of the elasticity tensor $\underline{\underline{\underline{\underline{\mathrm{H}}}}}$.

Therefore, from (II.165) when $\eta \to \infty$, $\underline{\underline{\underline{\underline{\mathrm{E}}}}}^{evp} \to \underline{\underline{\underline{\underline{\mathrm{H}}}}}$, resulting in instantaneous elasticity. However, when $\eta \to 0$, $\underline{\underline{\underline{\underline{\mathrm{A}}}}} \to \frac{\eta}{\Delta t}\underline{\underline{\underline{\underline{\mathrm{B}}}}}^{-1}$, then, it follows from (II.166) that

$$\underline{\underline{\underline{\underline{\mathrm{E}}}}}^{evp} \to \frac{\eta}{\Delta t}\left[\underline{\underline{\underline{\underline{\mathrm{B}}}}}^{-1} - \left(\underline{\underline{m}} : \underline{\underline{\underline{\underline{\mathrm{B}}}}}^{-1} : \frac{\partial \varphi}{\partial \underline{\underline{\sigma}}}\right)^{-1} \underline{\underline{\underline{\underline{\mathrm{B}}}}}^{-1} : \frac{\partial \varphi}{\partial \underline{\underline{\sigma}}} \otimes \underline{\underline{m}} : \underline{\underline{\underline{\underline{\mathrm{B}}}}}^{-1}\right] \tag{II.168}$$

In other terms, the limiting case $\eta \to 0$ results in instantaneous zero tangent stiffness tensor. This particular behaviour may cause numerical instabilities.

II.6.3 Example: one-dimensional bar problem

A bar of quasi-brittle material with a uniform cross-sectional area is permitted to deform only in the direction of the bar's axis (Fig. II.25). The bar has a mass density $\rho = 2000$ kg/m^3,

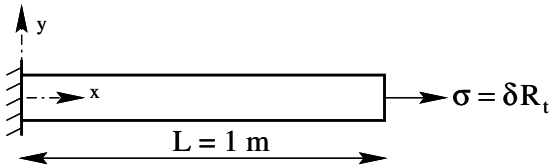

Figure II.25: One-dimensional bar problem

a Young's modulus $E = 50$ GPa and a poisson's ratio $\nu = 0$. The boundary conditions on this bar are

$$\begin{cases} u(0,\ t) = 0 & \forall\ t \geq 0 \\ \sigma(L,\ t) = \delta R_t & \forall\ t \geq 0 \end{cases} \tag{II.169}$$

[3] The Woodbury Formula: let $\mathbf{A}$ be a square $n \times n$ invertible matrix, whereas $\mathbf{U}$ and $\mathbf{V}$ are two $n \times k$ matrices with $k \leq n$ and β an arbitrary scalar. Assume that the $k \times k$ matrix $\Sigma = \mathbf{I}_k + \beta \mathbf{V}^t \mathbf{A}^{-1} \mathbf{U}$, in which $\mathbf{I}_k$ denotes the $k \times k$ identity matrix, is invertible. Then

$$\left(\mathbf{A} + \beta \mathbf{U}\mathbf{V}^t\right)^{-1} = \mathbf{A}^{-1} - \beta \mathbf{A}^{-1}\mathbf{U}\Sigma^{-1}\mathbf{V}^t\mathbf{A}^{-1}$$

This is called the Woodbury formula

where R_t is the tensile strength, δ is a positive scalar, u is the uniaxial displacement, and σ is the uniaxial stress.
The initial conditions are

$$\begin{cases} u(x,\ 0) = 0 & \forall\ x \in [0,\ L] \\ v(x,\ 0) = 0 & \forall\ x \in [0,\ L] \end{cases} \tag{II.170}$$

where v is the uniaxial velocity. If $\delta \in [1/2,\ 1]$, then the transient wave will propagate through the bar and its reflection at the fixed end will induce a tensile stress which exceed the tensile strength. Therefore, a localized softening zone emerges.

In what follows we choose $\delta = 0.75$. Our attention will be focused on the evaluation of the ability of the rate-independent and the rate-dependent plasticity models to describe the dynamic failure process. Explicitly, a rankine plasticity model will be investigated. It will be shown that, in the context of softening elasto-plasticity theory, the Rankine model bring to light an ill-posed problem. On the other hand, the introduction of a viscosity parameter can, in the context of softening elasto-viscoplasticity theory, suppress the localization problem and lead to a well-posed problem.

II.6.3.1 Elasto-plastic Rankine model

The governing equations of the elasto-plastic model are specified as follows

$$\begin{cases} \underline{\underline{\sigma}} = 2\mu\left(\underline{\underline{\epsilon}} - \underline{\underline{\epsilon}}^p\right) + \lambda \mathrm{tr}\left(\underline{\underline{\epsilon}} - \underline{\underline{\epsilon}}^p\right)\underline{\underline{\mathrm{I}}} \\ \dot{\underline{\underline{\epsilon}}}^p = \dot{\gamma}\,\overrightarrow{n} \otimes \overrightarrow{n} \\ \mathbf{F}(\underline{\underline{\sigma}},\ \xi) = \underline{\underline{\sigma}} : \overrightarrow{n} \otimes \overrightarrow{n} - R(\xi) \leq 0 \\ \dot{\xi} = ||\dot{\underline{\underline{\epsilon}}}^p|| = \sqrt{\dot{\underline{\underline{\epsilon}}}^p : \dot{\underline{\underline{\epsilon}}}^p} \\ R(\xi) = R_t\left[\alpha + (1-\alpha)\exp\left(-\omega\xi^2\right)\right], \quad \alpha \in [0,\ 1], \quad \omega \geq 0 \end{cases} \tag{II.171}$$

where R denotes the tensile strength and $\overrightarrow{n}$ the unit vector associated to the maximum principal stress direction. Fig. II.26 shows the response of the model in a uniaxial tension test. Constitutive parameters are also presented in Fig. II.26 [4].
Fig. II.27 shows, in a semi-log plot, the axial strain as a function of the distance from the bar end at $t = 0.3$ ms. As can be seen, there is an intense localisation of deformation into a narrow zone near the fixed end of the bar. The numerical solution that is obtained from finite element analyses reveals a dependence on the fineness of the mesh as shown in Fig. II.27. Furthermore, we have conducted several simulations and we have found that upon mesh refinement no physically meaningful solution can be obtained. All these results are in agreement with analytical predictions.

II.6.3.2 Elasto-viscoplastic Rankine model

The governing equations of the elasto-viscoplastic model are specified as follows

$$\begin{cases} \underline{\underline{\sigma}} = 2\mu\left(\underline{\underline{\epsilon}} - \underline{\underline{\epsilon}}^{vp}\right) + \lambda \mathrm{tr}\left(\underline{\underline{\epsilon}} - \underline{\underline{\epsilon}}^{vp}\right)\underline{\underline{\mathrm{I}}} \\ \dot{\underline{\underline{\epsilon}}}^{vp} = \dot{\gamma}\,\overrightarrow{n} \otimes \overrightarrow{n} \\ \dot{\gamma} = \frac{1}{\eta}\langle \dfrac{\underline{\underline{\sigma}} : \overrightarrow{n} \otimes \overrightarrow{n}}{R(\xi)} - 1 \rangle \\ \dot{\xi} = ||\dot{\underline{\underline{\epsilon}}}^{vp}|| = \sqrt{\dot{\underline{\underline{\epsilon}}}^{vp} : \dot{\underline{\underline{\epsilon}}}^{vp}} \\ R(\xi) = R_t\left[\alpha + (1-\alpha)\exp\left(-\omega\xi^2\right)\right], \quad \alpha \in [0,\ 1], \quad \omega \geq 0 \end{cases} \tag{II.172}$$

[4] Values of material parameters have been selected for illustrative purposes only.

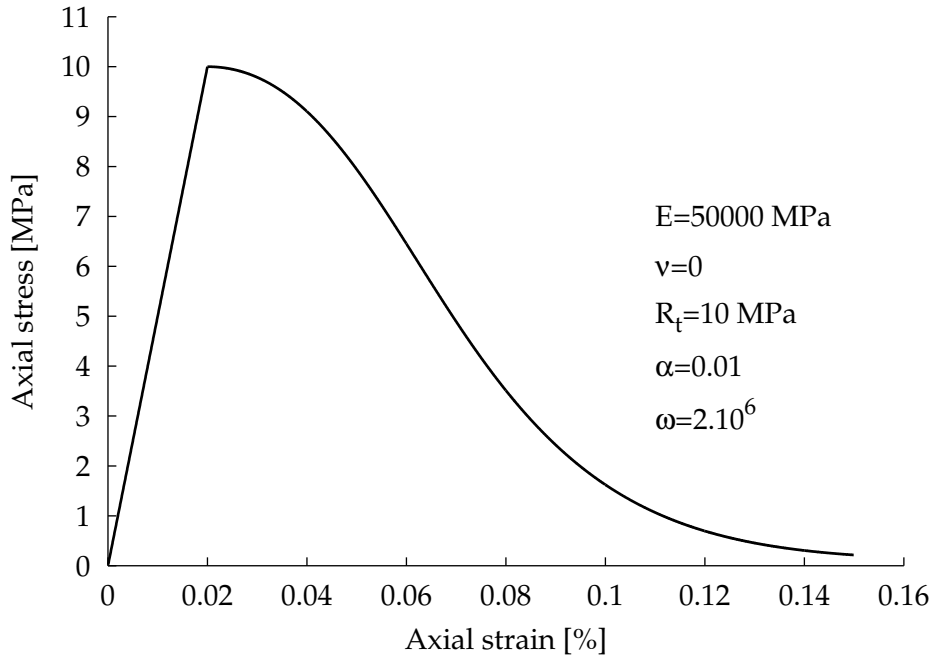

Figure II.26: Elasto-plastic Rankine model response for uniaxial tension test

where $\eta \in]0, \ +\infty[$ denotes a given viscosity parameter.
Fig. II.28 shows the response of the elasto-viscoplastic model in uniaxial tension test carried out at various strain rates. As can be seen, the response is strongly dependent upon the strain rate. For comparison, the elasto-plastic response is also presented in this figure. In this situation, the elasto-viscoplastic model, unlike plastic model, produces a regularised numerical solution, which can be concluded from Fig. II.29 which shows the axial strain as a function of the distance from the bar end. This figure reveals also the convergence towards one unique solution for several discretisations using an increasing number of elements.
The regularising effect of this rate-dependent model becomes more clear when the viscosity parameter is increased as can be seen from Fig. II.30. This observation may be explained by the fact that when the viscosity parameter increases, the material can acquire some ductility which avoid the development of a localized zone. This can be visualised by plotting the axial stress near the fixed end as shown in Fig. II.31. It can be seen that, unlike plasticity where the softening is very strong, the rate-dependent model shows moderate degradation and the softening becomes negligible when the viscosity parameter is increased. This particular behaviour will keep open the question of the wave propagation in softening material, which undergo, even under high strain rates, a stongly degradation response.

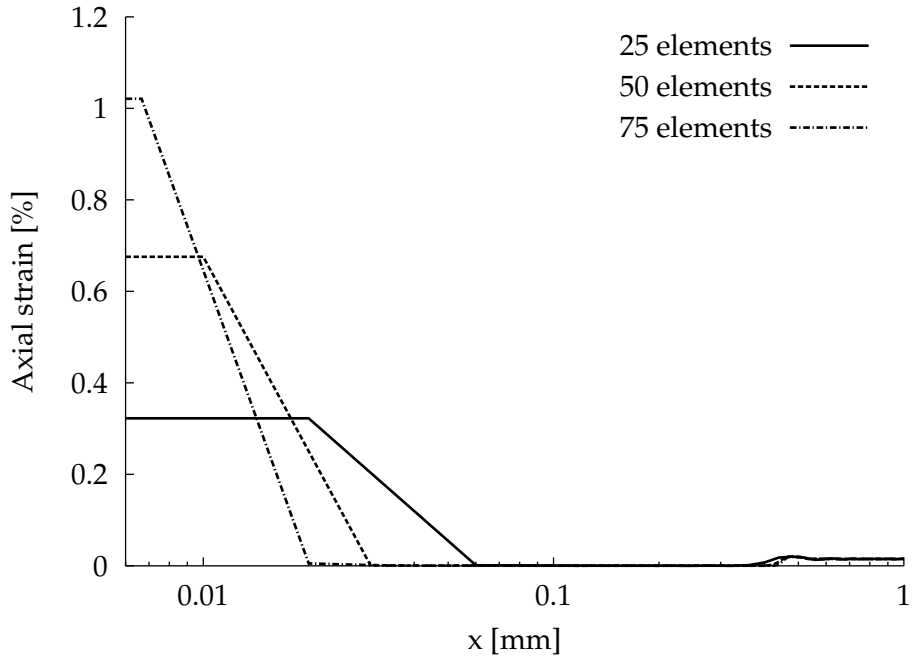

Figure II.27: Axial strain as a function of the distance from the bar end at $t = 0.3$ ms

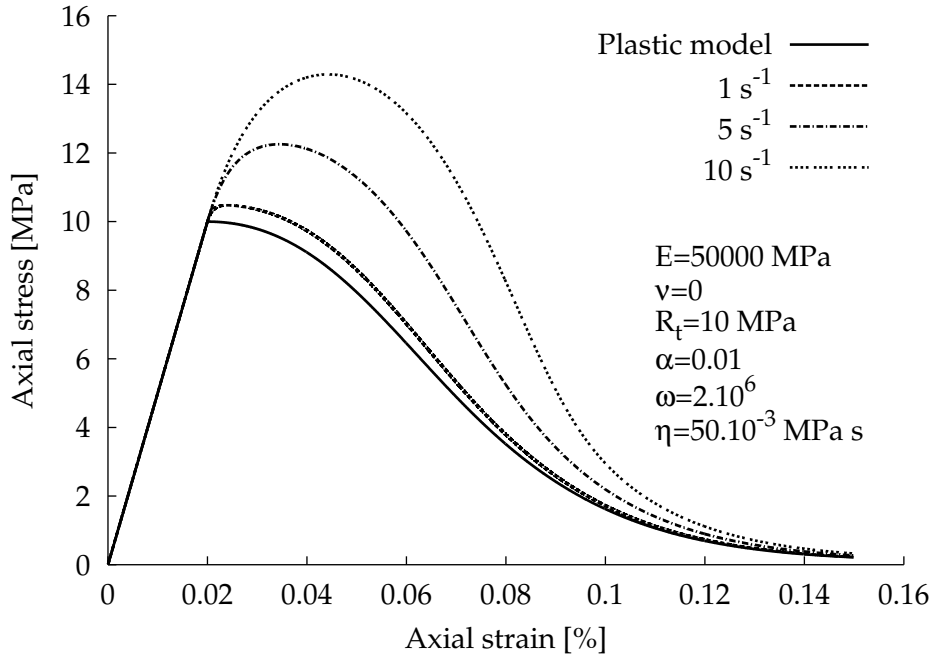

Figure II.28: Comparison of the elasto-viscoplastic model response carried out at various strain rates and the elasto-plastic response for the uniaxial tension test

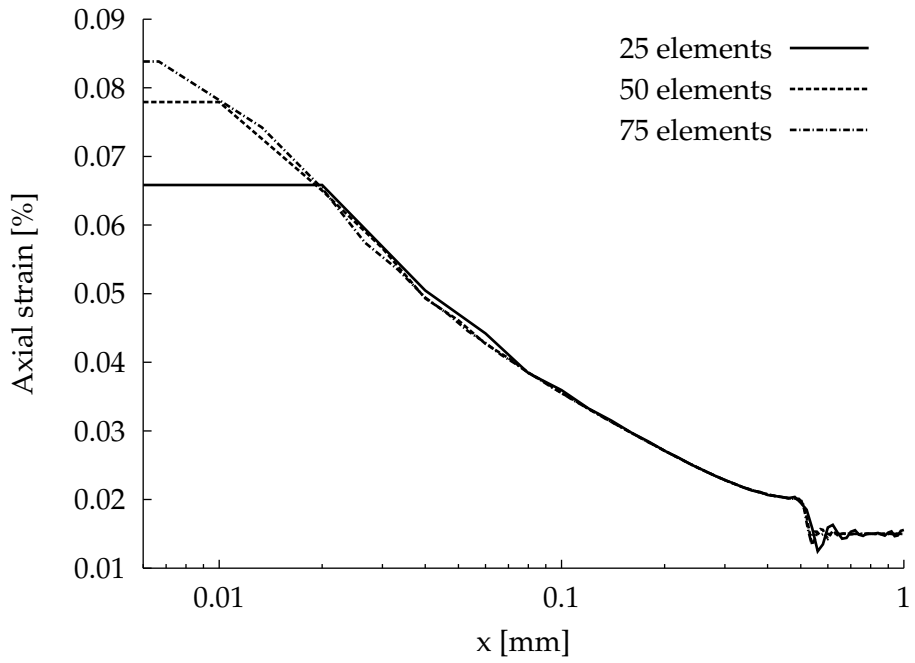

Figure II.29: Regularising effect of the elasto-viscoplastic model and mesh-independency of the numerical solution for the one-dimensional tensile bar at $t = 0.3$ ms

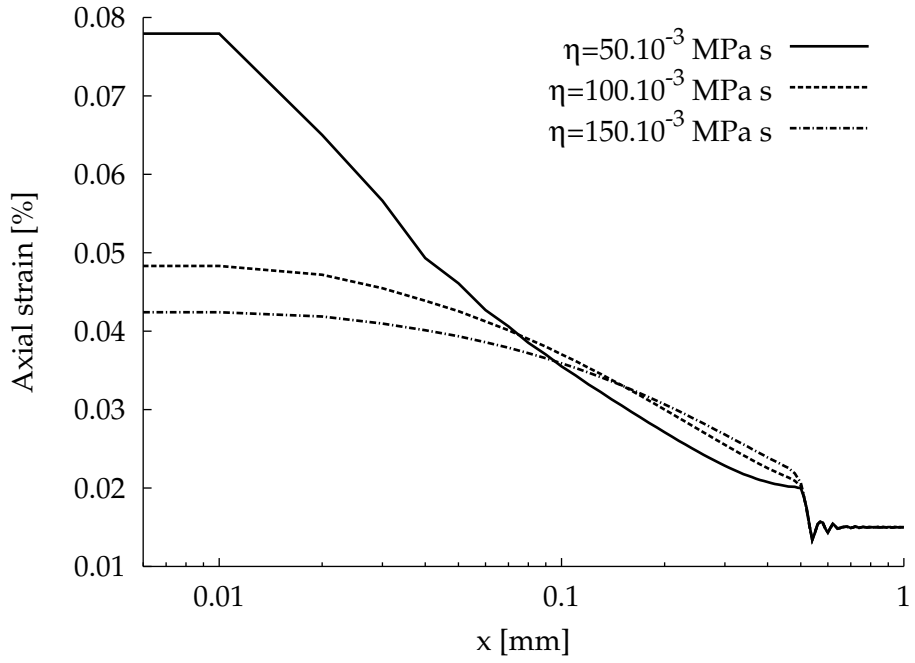

Figure II.30: Influence of the viscosity parameter on the development of the localized zone ($t = 0.3$ ms)

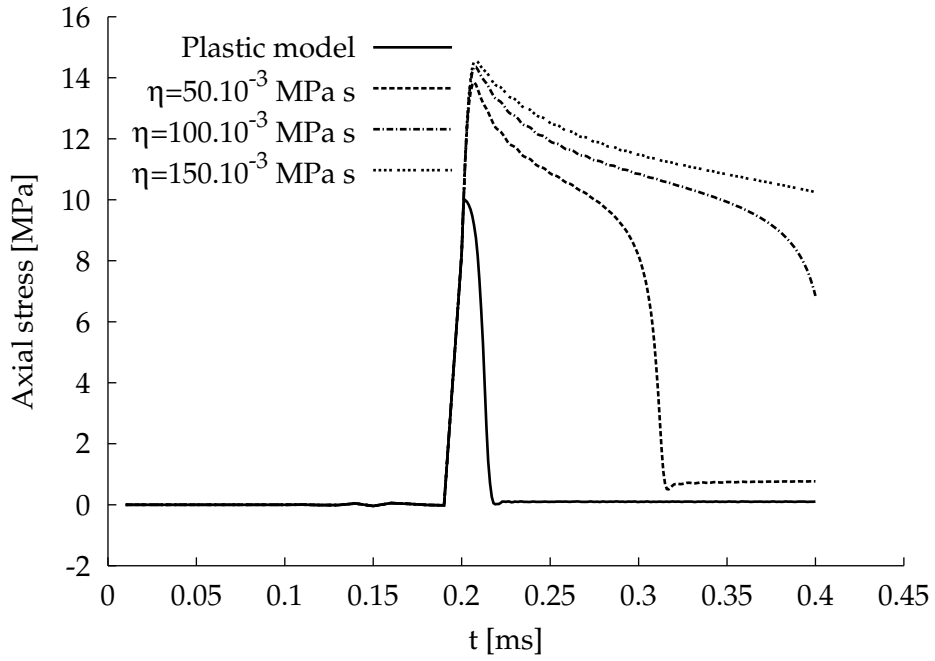

Figure II.31: Axial stress as a function of time near the fixed end of the bar

References

Addessio F.L., Johnson N., 1989. *A constitutive model for the dynamic response of brittle materials.* J. Appl. Phys. 67 (7), 3275-3286.

Bazant P.A., Bai S.P., Gettu R., 1993. *Fracture of rock: effect of loading rate.* Engrg Fracture Mechanics 45 (3) 393-398.

Blanton T.L., 1981. *Effect of strain rates from* 10^{-2} *to* 10^{-1} sec^{-1} *in triaxial compression tests on three rocks.* Int. J. Rock Mech. Min. Sci. & Geomech. Abstr. 18, 47-62.

Brady B.H.G., Brown E.T., 1999. *Rock Mechanics for underground mining.* Kluwer academic publishers.

Burlion N., Gatuingt F., Pijaudier-Cabot G., Daudeville L., *Compaction and tensile damage in concrete: constitutive modelling and application to dynamics.* Comp. Methods Appl. Mech. Engrg. 183, 291-308.

Chen W.F., Han D.J., 1988. *Plasticity for structural engineers.* Springer-Verlag New York Inc.

Carol I., Rizzi E., Willam K., 2001. *On the formulation of anisotropic elastic degradation. I. Theory on a pseudo-logarithmic damage tensor rate.* Int. J. solids and structures 38, 491-518.

Carol I., Rizzi E., Willam K., 2001. *On the formulation of anisotropic elastic degradation. II. Generalized pseudo-Rankine model for tensile damage.* Int. J. solids and structures 38, 519-546.

Chaboche J.L., 1992. *Damage-induced anisotropy: on the difficulties associated with the active-passive unilateral conditions.* Int. J. Damage Mech. 1, 148-171.

Coirier J., 2001. *Mécanique des milieux continus.* Dunod, France.

Cordebois J.P., Sidoroff F., 1982. *Endommagement anisotrope en élasticité et plasticité.* J. Méc. théorique et appliquée, numéro spécial, 45-60.

Chen Z., 2001. *Rate-dependent transition from tensile damage to discrete fracture in dynamic brittle failure.* Theo. Appl. Frac. Mechanics 35, 229-235.

Chong K.P., Hoyt P.M., Smith J.W., Paulsen B.Y., 1980. *Effects of strain rate on oil shale fracturing.* Int. J. Rock Mech. Min. Sci. & Geomech. Abstr. 17, 35-43.

Darve F., 1987. *Manuel de rhéologie des géomatériaux.* Presse de l'Ecole Nationale des Ponts et Chaussées, France.

Engelen R.A.B., Geers M.G.D., Baaijens P.T., 2003. *Nonlocal implicit gradient-enhanced elasto-plasticity for the modelling of softening behaviour.* Int. J. Plasticity 19, 403-433.

Etse G., Willam K., 1999. *Failure analysis of elastoviscoplastic material models.* J. Eng. Mechanics 125 (1), 60-69

Etse G., Willam K., 1991. *Fracture energy formulation for inelastic behavior of plan concrete.* J. Eng. Mechanics 120 (9), 1983-2011.

Feenstra P.H., De Borst R., 1995. *A plasticity model and algorithm for model-I cracking in concrete.* Int. J. Num. Meth. Engrg 38 (15), 2509-2529.

Frew D.J., Forrestal M.J., Chen W., 2001. *A split hopkinson pressure bar technique to determine compressive stress-strain data for rock materials.* Experimental mechanics 41 (1), 40-46

Freund L.B., 1990. *Dynamic fracture mechanics.* Cambridge University Press.

Gary G., Bailly P., 1998. *Behaviour of quasi-brittle material at high strain rate. Experiments and modelling.* Eur. J. Mech., A/solids 17 (3), 403-420.

Gebbeken N., Ruppert M., 1998. *On the concrete material response to explosive loading - Numerical simulations.* Int. Symposium on Structures under shock and impact, Thessaloniki, Greece.

Georgin J.F., Reynouard J.M., 2003. *Modeling of structures subjected to impact: concrete behaviour under high strain rate.* Cement & Concrete Composites 25, 131-143.

Germain P., 1986. *Mécanique tome II.* Ecole Polytechnique, France.

Govindjee S., Kay G., Simo J., 1995. *Anisotropic modelling and numerical simulation of brittle damage in concrete.* Int. J. Num. Meth. Engrg 38 (21), 3611-3633.

Gran J.K., Florence A.L., Colton J.D., 1989. *Dynamic triaxial tests of high-strength concrete.* J. Engrg Mechanics 115 (5), 891-904.

Grote D.L., Park S.W., Zhou M., 2001. *Dynamic behavior of concrete at high strain rates and pressures: I. experimental characterization.* Int. J. Imp. Engrg 25, 869-886.

Hadhri T., Zenzri H., 1997. *Mécanique des milieux continus.* Ecole Polyetchnique de Tunisie.

Halam D., Dragon A., 1998. *An anisotropic model of damage and frictional sliding for brittle materials.* Eur. J. Mech., A/solids 17 (3), 439-460.

Johnson G.R., Holmquist T.J., 1993. *A computational constitutive model for brittle materials subjected to large strains, high strain rates, and high pressures.* Constitutive model for brittle materials.

Johnson J.N., Addessio F.L., 1988. *Tensile plasticity and ductile fracture.* J. Appl. Phys. 64 (12), 6699-6712.

Lemaitre J., Chaboche J.L., 1985. *Mécanique des matériaux solides..* Dunod, France.

Lockner D.A., 1995. *Rock failure.* Published by the American Geophysical Union.

Klisinski M., 1985. *Degradation and plastic deformation of concrete.* PhD thesis, Polish Academy of Sciences.

Malvar L.J., Crawford E., 1998. *Dynamic increase factors for concrete.* Twenty-Eighth DDESB seminar, Orlando, FL.

Markeset G., Hillerborg A., 1995. *Softening of concrete in compression - Localization and size effects.* Cements and Concrete Research 25 (4), 702-708.

Meftah F., 1995. *Plasticité au gradient, approche multicouches.* Des Géomatériaux aux ouvrages, Hermès. France.

Meschke G., Lackner R., Mang A., 1998. *An anisotropic elastoplastic-damage model for plain concrete.* Int. J. Num. Meth. Engrg 42 (4), 703-727.

Meyers M.A., 1994. *Dynamic behavior of materials.* John Wiley & sons, Inc.

Mindess S., 1984. *Rate of loading effects on the fracture of cementitious materials.* Application of fracture mechanics to cementitious composites. Northwestern University, S.P. Shah Editor, U.S.A

Murakami S., Kamiya K., 1997. *Constitutive and damage evolution equations of elastic-brittle materials based on irreversible thermodynamics.* Int. J. Mech. Sci. 39 (4), 473-486.

Nguyen Q.S., 2000. *Stabilité et mécanique non linéaire.* Hermes Science Publications, France.

Nikolaevskiy V.N., 1996. *Geomechanics and fluidodynamics.* Kluwer Academic Publishers.

Olsson W.A., 1991. *The compressive strength of tuff as a function of strain rate from* 10^{-10} *to* 10^{3} sec^{-1}. Int. J. Rock Mech. Min.Sci. & Geomech. Abstr 28 (1), 115-118.

Ortiz M., 1985. *A constitutive theory for the inelastic behavior of concrete.* Mechanics of Materials 4, 67-93.

Park S.W., Xia Q., Zhou M., 2001. *Dynamic behavior of concrete at high strain rates and pressures: II. numerical simulation.* Int. J. Imp. Engrg. 25, 887-910.

Peerlings R.H.J., Geers M.G.D., De Borst R., Brekelmans W.A.M., 2001. *A critical comparison of nonlocal and gradient-enhanced softening continua.* Int. J. solids and structures 38, 7723-7746.

Peng S.S., 1973. *Time-dependent aspects of rock behaviour as measured by a servo-controlled hydraulic testing machine.* Int. J. Rock Mech. Min. Sci. & Geomech. Abstr. 10, 235-246.

Perkins R.D., Green S.J., Friedman M., 1970. *Uniaxial stress behavior of porphyritic tonalite at strain rates to* 10^3*/seconds.* Int. J. Rock Mech. Min. Sci. 7, 527-535.

Pivonka P., Lackner R., Mang H.A., 2000. *Numerical analyses of concrete subjected to traixial compressive loading.* European congress on computational methods in applied sciences and engineering ECCOMAS 2000, Barcelona.

Reinhardt H.W., Rossi P., Van Mier J.G.M, 1990. *Joint investigation of concrete at high rates of loading.* Materials and Structures 23, 213-216.

Rokugo K., Koyanagi W., 1992. *Role of compressive fracture energy of concrete on failure behaviour of reinforced concrete beams, application of fracture mechanics to reinforced concrete.* Elsevier applied science, 437-464.

Sercombe J., 1998. *Modélisation du comportement du béton en dynamique rapide - Application au calcul des conteneurs à haute intégrité.* Thèse de doctorat, Ecole Nationale des Ponts et Chaussées, France.

Sierakowski R.L., 1984. *Dynamic effect in concrete materials.* Application of fracture mechanics to cementitious composites. Northwestern University, S.P. Shah Editor, U.S.A

Simo J.C., Hughes T.J.R., 1998. *Computational inelasticity.* Springer-Verlag New York, Inc.

Tedesco J.W., Ross C.A., 1998. *Strain-rate-dependent constitutive equations for concrete.* Transactions of the ASME 120, 398-405.

Tijani M., 2000. *VIPLEF3D User's Manual, Version 001204.* Ecole des Mines de Paris, France.

Tijani M. 1978. *Résolution numérique des problèmes d'élastoviscoplasticté - Application aux cavités de stockage du gaz en couches salines profondes.* Thèse de Docteur-Ingénieur, Ecole des Mines de Paris, France.

Van Mier, J.G.M., 1984. *Complete stress-strain behaviour and damaging status of concrete under multiaxial conditions.* International conference on concrete under multiaxial conditions, Vol. 1, presses de l'université Paul Sabatier, Toulouse, France.

Vroonhoven J.C.W., De Borst, R., 1999. *Combination of fracture and damage mechanics for numerical failure analysis.* Int. J. Solids Structures 36, 1169-1191.

Yalun Y., 1990. *On the effect of dynamic fracture of rocks on the blasting.* Fragblast'90, Brisbane.

Zenzri H., 1999. *Formulation de lois de comportements dissipatifs et calcul de structures anélastiques.* Ecole Polytechnique de Tunisie.

Zhao J., 2000. *Applicability of Mohr-Coulomb and Hoek-Brown strength criteria to the dynamic strength of brittle rock.* Int. J. Rock Mech. and Mining Sci. 37, 1115-1121.

Zhao J., Li H.B., Wu M.B., Li T.J., 1999. *Dynamic uniaxial compression tests on a granite.* Int. J. Rock Mech. and Mining Sci. 36, 273-277.

Chapter III

Application: Laboratory Rock Fragmentation by Blasting

La connaissance des mécanismes de fragmentation induits par l'abattage à l'explosif est d'une importance capitale pour un abattage efficace des roches. Un meilleur résultat de tir a pour objectif une bonne qualité de fragmentation pour un coût de production minimal.

Le développement de modèles numériques capables de simuler le processus entier du tir à l'explosif représente pour la communauté scientifique, à travers le monde, un défit majeur qui reste en cours de développement. A notre connaissance, actuellement, il n'existe aucun outil numérique, basé sur des considérations physiques réalistes, qui soit en mesure de modéliser l'intégralité du processus de la fragmentation à l'explosif. Ce manque de modélisations fiables peut être expliqué, d'un point de vue mécanique, par le fait que l'abattage des roches à l'explosif réunit deux branches difficiles, à savoir la mécanique des roches et la thermodynamique des explosifs (la détonique). Pour la première, la difficulté réside dans la complexité du milieu rocheux (fissuration à l'échelle microscopique et macroscopique). Les plans de faiblesses, qu'ils soient naturels ou induits par des tirs précédents, sont très difficiles d'être pris en compte dans des outils numériques déterministes. Cependant, ces plans sont d'une importance fondamentale dans la conception d'un tir optimisé. Ainsi, la construction de modèles numériques réalistes doit intégrer, entre autres, le fait que le résultat final du tir, en termes de distribution de fragments, est une combinaison de la distribution des blocs de roche qui ont été simplement détachés sous l'effet de l'explosion et la distribution des fragments venant de la fragmentation des blocs intacts. Quant à la détonique, la difficulté réside dans l'élaboration de lois de comportement capables de tenir en compte la transformation chimique des produits de détonation et l'interaction de ces produits avec la roche environnante.

Ce chapitre ne traite ni un problème réel de tir pratique, ni les détails des opérations d'abattage à l'explosif, mais se concentre sur l'analyse du processus de rupture et la prévision de la distribution des fragments à partir des essais de fragmentation faits à petite échelle. Néanmoins, pour avoir une idée sur l'interaction roche-explosif, un modèle théorique simple a été traité. Dans notre modélisation numérique, cette interaction a été introduite par une condition aux limites donnant la pression générée par les produits de détonation en fonction du temps.

III.1 Introduction

Knowledge of fragmentation mechanisms induced by explosive loading is of engineering importance to break rock efficiently, and furthermore to control fracture extension in order to limit damage inflicted to the surrounding rock mass. Successful blasting operations can lead to the reduction of reinforcement costs and to the application of highly economic and profitable extraction techniques to recover less accessible but valuable resources.
The development of tractable computer based models to describe the entire blasting process from detonation to the particle size distribution is a great challenge which is still under development. To our knowledge, at present, it does not exist a unified numerical tool that can model the full process by using realistic physical approach. This lack of models can be

explained, from a mechanical point of view, by the fact that the blasting problem couples two difficult fields which are the rock mechanics and the detonation of explosives. Concerning rock mechanics, the difficulty is related to the material's heterogeneous nature. The weak planes, which are formed by geological structures and previous blastings are not easy to be taken into account in deterministic numerical tools. However, these weak planes are of fundamental importance in the design of an optimised blast which achieve the most suitable rock fragments distribution with a minimum mining production cost. So, construction of a realistic numerical model to simulate the physical process of the rock blasting should, among other things, take into account the fact that the final blast result, in terms of particle size distribution, is a combination of both the distribution of the natural rock fragments that have simply been loosened by the blast and the distribution of fragments coming from the fragmentation of intact blocs.
Turning to the detonation of explosives, the difficulty in this field is related firstly to the lack of an accurate description of the explosive behaviour, secondly to the interaction between the detonation gases and the surrounding fractured rock.
This chapter treats neither a complete practical blasting problem nor the details of rock-blasting operations, but focuses on the analysis of the fracture process and the prediction of the particle size distribution of laboratory blasting tests. As was mentioned in the chapter I, the experimental results that will be described were obtained from chamber blasting tests, done in Montan University of Leoben, of cylindrical or cubical samples of rock material. The blasted material was collected and in some cases a rebuilding attempt was done. Figs. III.1

Figure III.1: Rebuilt cylindrical and cubical samples

shows typical results of such rebuilding obtained from the blasting of a cylindrical and a cubical sample.
Both figures show a radial fractured region and a material missing zone which indicates that, near the blasthole, the fracture process is so intense that any rebuilding attempt was failed. It is widely accepted that this zone is the result of a crushed zone around the drill hole and an intensively fractured zone probably resulting from a compressive shear loading.

In our numerical modelling, the response of the structure was our main interest. The modelling of the blast loading is taken into account by using a defined pressure-time history on an equivalent hole wall. At present, the numerical model cannot handle the interaction between solid and fluid (detonation gases) problems. However, in order to have an idea about the stress state in the immediate vicinity of the blasthole, an analytical approach was developed. In this approach, the explosive-material interaction was taken into account. The

fragmentation is treated only with the numerical modelling.

III.2 Analytical modelling

In rock blasting operations, the rock is fragmented by using an explosive charge confined within the space of the borehole. After the ignition of the charge, the detonation propagates through the charge at the velocity of detonation. The detonation process results in a phase change of the explosive material, as a result hot detonation gases at high pressure is produced. Often, the behaviour of the explosive is represented by an equation of state and a decomposition law of the form

$$e = e(p,\ \rho_e,\ \lambda), \quad r = r(p,\ \rho_e,\ \lambda) \tag{III.1}$$

Here, e, p, ρ_e, r, λ are the specific internal energy, the pressure, the density, the reaction rate and the progress variable of the chemical reaction. When $\lambda = 0$ the explosive is unreacted; $\lambda = 1$ corresponds to a completely reacted explosive. In this study, we assume that the generation of the detonation gases occurs instantaneously ($\lambda = 1$) and that these gases are described by the polytropic equation of state

$$e(p,\ \rho_e) = \frac{1}{\gamma - 1}\frac{p}{\rho_e} \tag{III.2}$$

where γ is the polytropic gas constant.
Concerning the solid, we consider an homogeneous, isotropic and linear elastic solid. As for the borehole, both spherical and cylindrical case will be treated. Finally we assume that the detonation parameters can be given by the Chapman-Jouguet states and that the expansion of the detonating explosive from the original explosive volume to the borehole volume is an isentropic process.
In the following subsections we will firstly investigate the analytical solution of the so-called cavity problem. Secondly, we will present briefly the Chapman-Jouguet states. Following this, the explosive-material interaction problem will be treated.

III.2.1 Solution of the cavity problems

We consider the dynamic behaviour of cylindrical and spherical cavity in an infinite homogeneous, isotropic and linear elastic solid. The cylindrical cavity will be treated with the assumption of plain strain condition.
Let us consider the small displacements assumption. Thus, the deformed configuration will be the same as the reference configuration. In cylindrical coordinates (r, θ, z), the stress-displacement relations can be written as

$$\sigma_r = \hat{E}\left[\frac{\partial u}{\partial r} + k(1-\ell)\frac{u}{r}\right] \tag{III.3}$$

$$\sigma_\theta = \hat{E}\left[(1-\ell)\frac{\partial u}{\partial r} + (k(1-\ell)+\ell)\,\frac{u}{r}\right] \tag{III.4}$$

with

$$\hat{E} = \frac{E(1-\nu)}{(1+\nu)(1-2\nu)}, \qquad \ell = \frac{1-2\nu}{1-\nu} \tag{III.5}$$

where u is the radial displacement, σ_r and σ_θ are respectively the radial and the tangential stresses. k is an integer defining the studied case ($k = 1$ for cylindrical cavity, $k = 2$ for

spherical cavity).
The only nontrivial equilibrium equation is the radial one

$$\frac{\partial \sigma_r}{\partial r} + k\frac{\sigma_r - \sigma_\theta}{r} = \rho \frac{\partial^2 u}{\partial t^2} \tag{III.6}$$

where ρ is the solid density. Using Eq. III.3, III.4 and III.6, one can obtain the following wave equation

$$\frac{\partial^2 u}{\partial r^2} + \frac{k}{r}\left(\frac{\partial u}{\partial r} - \frac{u}{r}\right) - \frac{1}{c^2}\frac{\partial^2 u}{\partial t^2} = \Gamma = 0 \tag{III.7}$$

where $c = \sqrt{\hat{E}/\rho}$ is the velocity of longitudinal elastic waves in an infinite medium, and Γ is a radial volumetric weight. Eq. III.7 has to be solved with the following initial and boundary conditions

$$u(r,\ 0) = 0 \quad \forall\ r \geq a \tag{III.8}$$

$$\lim_{r \to +\infty} u(r,\ t) = 0 \quad \forall\ t \geq 0 \tag{III.9}$$

$$\sigma_r(a,\ t) = -p(t) \quad \forall\ t \geq 0 \tag{III.10}$$

where a is the original cavity radius and $p(t)$ is the pressure on the borehole wall. By using the isentropic process expansion assumption, the borehole pressure can be expressed as the following

$$p(t) = P_0\left(\rho_e/\rho_e^0\right)^\gamma = P_0\left(1 + \frac{u(a,\ t)}{a}\right)^{-(k+1)\gamma} \tag{III.11}$$

where P_0 is the initial shock pressure on the borehole wall, and ρ_e^0 is the initial density of the explosive.
Eq. III.11 is obtained with the assumption that the density of the detonation gas decreases only due to the gas expansion. Now, if we assume that $u(a,\ t)/a \ll 1$, Eq. III.11 becomes

$$p(t) = P_0\left(1 - (k+1)\gamma\frac{u(a,\ t)}{a}\right) \tag{III.12}$$

To solve the defined initial boundary value problem, we will use the solution developed by Tijani (1993). Firstly, we introduce the dimensionless variables

$$\xi = \frac{r}{a} \tag{III.13}$$

$$\eta = 1 + \frac{ct - r}{a} \tag{III.14}$$

By asymptotic considerations, Tijani shows that the radial displacement can be written as

$$u(r,\ t) = \frac{P_0}{\hat{E}} a\ \phi(\xi,\ \eta) \tag{III.15}$$

where ϕ is given by

$$\phi(\xi,\ \eta) = \xi^{-k}\varphi(\eta) + \xi^{-k/2}\psi(\eta) \tag{III.16}$$

$\varphi(\eta)$ and $\psi(\eta)$ are determined by minimization of the volumetric weight Γ with respect to a defined metric. $\Gamma = 0$ corresponds to the exact solution. In view of Eq. III.15 and III.16, Γ takes the from

$$\Gamma = \frac{P_0}{a}\left[k\varphi'\xi^{(-k-1)} - \left(\frac{k^2}{4} + \frac{k}{2}\right)\psi\xi^{(-2-k/2)}\right] \tag{III.17}$$

where $f'(x) = df/dx$. For the spherical cavity, it is possible to nullify Γ by simply taking

$$\psi(\eta) = \varphi'(\eta) \quad \forall\ \eta \in [0,\ +\infty[\tag{III.18}$$

In this case, the obtained solution will correspond to the exact one. However, since, we can not obtain an exact solution for the cylindrical cavity, Tijani suggests that

$$\psi(\eta) = A\varphi'(\eta) \quad \forall\ \eta \in [0,\ +\infty[\tag{III.19}$$

where A is a constant determined by the minimization of Γ. To do that, one way consists of the minimization of the distance between $f(\xi) = \frac{3}{4}A\xi^{-5/2}$ and $g(\xi) = \xi^{-2}$ defined as

$$d(f,\ g) = \left[\int_1^{\infty} \left(f(\xi) - g(\xi)\right)^2 \xi d\xi\right]^{1/2} \tag{III.20}$$

This leads to $A = 8/5$.
Finally, the general solution can be written as

$$u(r,\ t) = \frac{P_0}{\hat{E}} a\ \phi(\xi,\ \eta) = \frac{P_0}{\hat{E}} a\left[\xi^{-k}\varphi(\eta) + A\xi^{-k/2}\varphi'(\eta)\right] \tag{III.21}$$

with

- $k = 1$ and $A = 8/5$ for cylindrical cavity (approximate solution)
- $k = 2$ and $A = 1$ for spherical cavity (exact solution)
- $\varphi(0) = \varphi'(0) = 0$ (Initial conditions)
- $\sigma_r(1,\ \eta) = P_0\left[\frac{\partial\phi}{\partial\xi}(1,\ \eta) + k(1-\ell)\phi(1,\ \eta) - \frac{\partial\phi}{\eta}(1,\ \eta)\right] = -p(\eta)$ (Boundary condition)

Therefore, the only unknown function is $\varphi(\eta)$ which can be easily determined by considering the boundary condition at the cavity wall ($\xi = 1$). Thus, we obtain the following second order linear differential equation

$$\varphi'' + m\varphi' + \omega\varphi = 1/A \tag{III.22}$$

where

$$\begin{cases} m = \frac{1}{A} - \frac{k}{2} + k\ell + \gamma(k+1)\frac{P_0}{\hat{E}} \\ \omega = \frac{1}{A}\left(k\ell + \gamma(k+1)\frac{P_0}{\hat{E}}\right) \end{cases} \tag{III.23}$$

Let $\Delta = m^2 - 4\omega$. To solve Eq. III.22, we will distinguish the following three cases

- Case 1: $\Delta > 0$

$$\varphi(\eta) = F\exp\left(-(m - \sqrt{\Delta})\ \eta/2\right) + G\exp\left(-(m + \sqrt{\Delta})\ \eta/2\right) + \frac{1}{\omega A} \tag{III.24}$$

- Case 2: $\Delta = 0$

$$\varphi(\eta) = (F + G\ \eta)\exp\left(-m\ \eta/2\right) + \frac{1}{\omega A} \tag{III.25}$$

- Case 3: $\Delta < 0$

$$\varphi(\eta) = \left[F\cos\left(\sqrt{-\Delta}\ \eta/2\right) + G\sin\left(\sqrt{-\Delta}\ \eta/2\right)\right]\exp\left(-m\ \eta/2\right) + \frac{1}{\omega A} \tag{III.26}$$

where F and G are integration constants evaluated by using the initial conditions ($\varphi(0) = \varphi'(0) = 0$).

Pressure-time history on the blasthole wall

The developed analytical approach will help us to have an appreciation on the dynamic stresses on the wall of the blasthole produced by the rapid expansion detonation gases. For a given P_0 and γ, Fig. III.2 illustrates a typical result for the radial stress on the blasthole wall as a function of time for the spherical and the cylindrical cavity in limestone material. Firstly, the radial stress, starting from $-P_0$ at $t = 0$, will increase in a few micro seconds to a maximum value. In a second time, it will decrease until reaching a static value which can be given by

$$P_{Static} = \frac{-P_0}{1 + \dfrac{\gamma(k+1)P_0}{k\ell\hat{E}}} \tag{III.27}$$

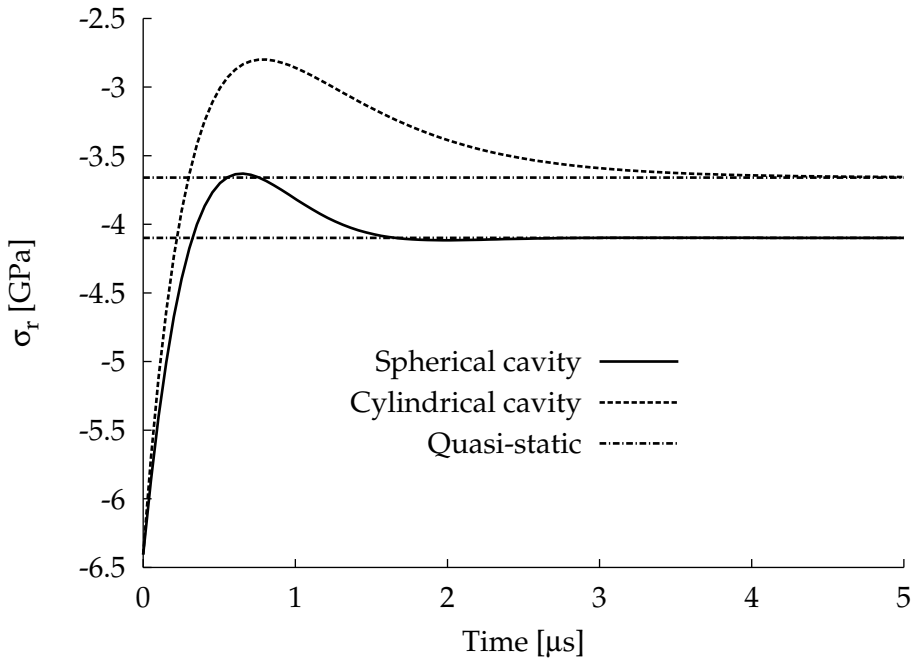

Figure III.2: Radial stress at wall cavity

The static value produces behind the stress wave a quasi-satic stress distribution in the solid. The fact of obtaining a great static value is related, probably, to the assumption that the density of the detonation gas decreases only due to the gaz expansion (i.e. the change of the gaz volume). However, since the tangantial stress (Fig. III.3), which becomes rapidly tensile, is considerably higher, radial cracks will be developed and, as a consequence, the detonation gaz density will decrease also due to the gaz flow through the created cracks.

III.2.2 Balance laws and Chapman-Jouguet state

Consider a shock front moving with the normal speed D_n. Ahead of the front, we assume that we have

$$\rho_e = \rho_e^0, \quad v_n = 0, \quad p = 0, \quad e = e_0 \tag{III.28}$$

where v_n is the normal particle velocity and e_0 is the specific internal energy in the totally expanded state. For gases

$$e_0 = e_0^s + Q \tag{III.29}$$

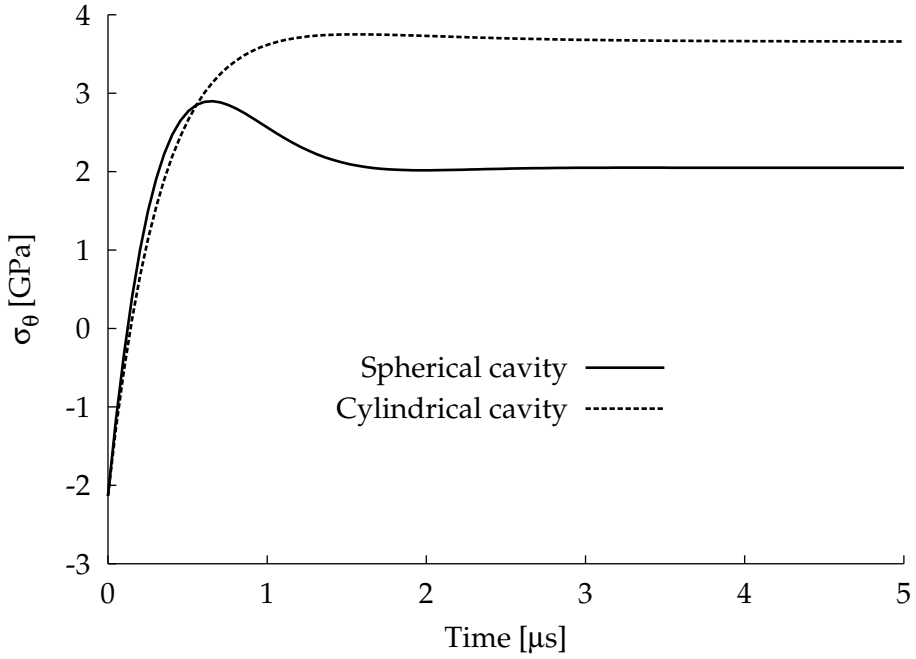

Figure III.3: Tangential stress at the wall cavity

where e_0^s is the internal energy of the solid explosive and Q is the specific chemical energy released by the detonation. In this study, we assume that $e_0^s = 0$.
Thus, the normal jump conditions across the interface can be given by

$$[\rho_e(v_n - D_n)] = 0 \tag{III.30}$$

$$[\rho_e v_n(v_n - D_n) + p] = 0 \tag{III.31}$$

$$[E(v_n - D_n) + v_n p] = 0 \tag{III.32}$$

where [ ] denote the jump in a quantity across the interface and E is the total energy, defined by

$$E = \rho_e \left(e + \frac{1}{2} v_n^2 \right) \tag{III.33}$$

With the polytropic equation of state, the jump condition algebra derives a quadratic equation for the normal velocity v_n. If we identify the speed D_n as the Chapman-Jouguet (CJ) value (D_{CJ}), the quadratic equation for v_n can be solved to give

$$v_n = \frac{D_{CJ} \pm \sqrt{D_{CJ}^2 - 2\left(\gamma^2 - 1\right) e_0}}{\gamma + 1} \tag{III.34}$$

The CJ-state is found by setting to zero the argument of the radical, which leads to the identification of either the D_{CJ} in terms of the energy e_0 or vice versa. Since we generally regard D_{CJ} as being given experimentally, we choose to write the condition as

$$e_0 = \frac{D_{CJ}^2}{2(\gamma^2 - 1)} \tag{III.35}$$

Then the CJ-state can be characterized by

$$\rho_{CJ} = \rho_e^0 \left(\frac{\gamma + 1}{\gamma} \right) \tag{III.36}$$

$$p_{CJ} = \frac{\rho_e^0 D_{CJ}^2}{\gamma + 1} \tag{III.37}$$

$$v_{CJ} = \frac{D_{CJ}}{\gamma + 1} \tag{III.38}$$

III.2.3 Explosive-Material interaction: initial shock parameters

The initial shock pressure on the borehole wall (P_0) is an unknown parameter. In order to calculate it we should take into account the explosive-material interaction.
The interaction of a detonating explosive with a material in contact with it or in close proximity is extremely complex, since it involves detonation waves, shock waves, expanding gazes, and their interrelationships (Meyers, 1994). In this study we will use a simplified approach based on the "impedance matching" technique used in solid-solid impact problems (Meyers, 1994). To do that, we proceed as the follows

- We assume that, prior to the impact on the borehole wall, the detonation gases are traveling at the CJ velocity given by Eq. III.38, whereas the solid is at rest. After impact, two compressive shock waves are created: one travels into the solid, with velocity v_0, and one travels into the detonation gases, with velocity, v_e.
- The material has to be continuous across the impact interface, that is, the same particle velocity exists in the compressed region.
- The pressure has also to be the same in the compressed region.

Therefore, prior to impact, all particles in the detonation gases have the same velocity v_{CJ}. Upon the impact, the particle velocity in the compressed region of the detonation gases is reduced by a value v_e so that the resultant particle velocity is $v_{CJ} - v_e$. In the solid, the particle velocity in the compressed region is v_0. Then from the equality of the particle velocities one can obtain

$$v_e + v_0 = v_{CJ} \tag{III.39}$$

From the balance laws (Eq. III.30, III.31, III.32) and by using the polytropic equation of state (Eq. III.2), we can express the pressure in the compressed region of detonation gases

$$P_e = \frac{1}{2}\rho_e^0(\gamma+1)v_e^2 + Q\rho_e^0(\gamma-1) \tag{III.40}$$

This pressure will be equal to P_0. Thus, from Eq. III.39 one has

$$P_0 = \frac{1}{2}\rho_e^0(\gamma+1)(v_{CJ}-v_0)^2 + Q\rho_e^0(\gamma-1) \tag{III.41}$$

On the other hand v_0 can be given by

$$v_0 = \frac{\partial u}{\partial t}(a\ ,0) = \frac{P_0}{\rho c}A\varphi''(0) \tag{III.42}$$

$\varphi''(0)$ is also function of P_0. Consequently v_0 is the solution of a non linear scalar equation which can be solved iteratively.
It is worth noting that we can obtain simply the same result by using Eq. III.39 and equating P_e to $\rho c v_0$.

The influence of the solid and explosive properties

To identify the contribution of each parameter of both the solid and the explosive, the initial shock pressure and the initial particle velocity are computed with one variable at a time while keeping the others unchanged. As can be seen from Fig. III.4a, the increase of Young's modulus increases the initial pressure but decreases strongly the particle velocity. The increase of the explosive density or the detonation velocity causes the increase of the shock pressure and the particle velocity as illustrated in Fig. III.4b and III.4c. Fig. III.4d shows the influence of the polytropic gas constant [1]. Both initial pressure and initial particle velocity decrease with increasing γ.

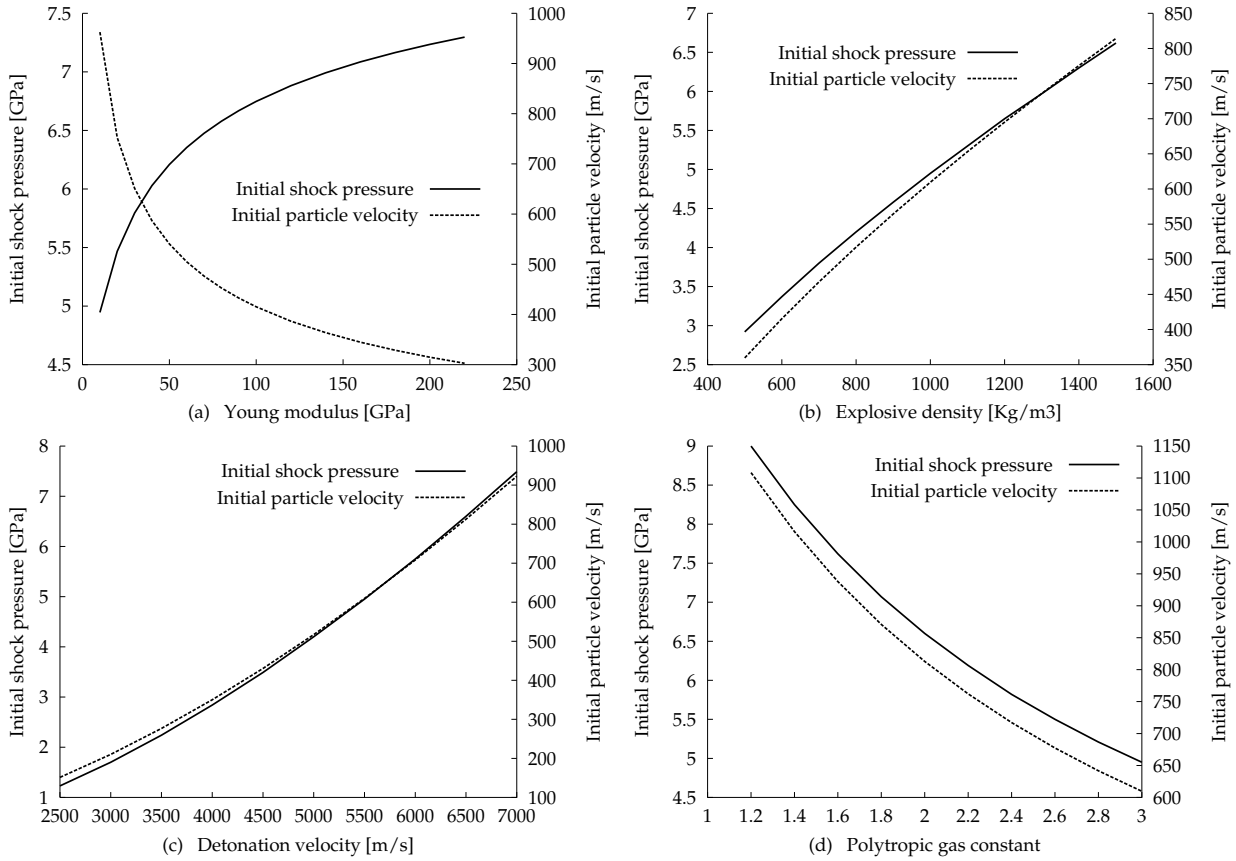

Figure III.4: Effect of Young's modulus, explosive density, detonation velocity and polytropic gas constant

III.3 Numerical Simulation of the fracture process

III.3.1 Main assumptions

III.3.1.1 Explosive-material interactions

As stated earlier, immediately after the detonation of the explosive, the whole blasthole is filled with detonation gases at very high pressure and temperature. The pressure of the explosion pulse greatly exceeds the compressive strength of the rock, as a result a thin annulus is formed around the blasthole where the rock has been broken and crushed. The

[1] For most explosives, γ is found to vary between 1.3 and 3 (Meyers, 1994).

outer boundary of this crushed annulus then exerts a radial stress on the surrounding rock. The radius of the pulverized area encloses what is called the *equivalent hole*. In this study, the boundary condition will be considered at this equivalent hole which for cylindrical charges will be of the form

$$\sigma_r(a,\ z,\ t) = -p(z,\ t) \quad \forall\ (z,\ t) \in [0,\ h] \times [0,\ T] \tag{III.43}$$

where σ_r is the radial stress; p is the applied pressure; a is the equivalent hole radius; t is time; h is the equivalent hole length; and T is the loading duration.
The detonation waves propagate with a high velocity (between 2000 to 7000 ms^{-1} depending on the type of explosive) which justifies the assumption that the pressure in the equivalent hole acts uniformly along the z-axis

$$\sigma_r(a,\ z,\ t) = -p(t) \quad \forall\ t \in [0,\ T] \tag{III.44}$$

$p(t)$ is assumed to be expressed as

$$\begin{cases} p(t) = p_0 \exp\left[-\left(\frac{t-t0}{S}\right)^2\right] & \text{if } t\ \in [0,\ t_0] \\ p(t) = p_0 \left(\frac{t}{t0}\right)^{\omega} \exp\left[\omega(1-\frac{t}{t_0})\right] & \text{if } t\ \in\ ]t_0,\ T] \\ (p_0,\ t_0,\ S,\ \omega)\ \in \mathbb{R}_+^4 \end{cases} \tag{III.45}$$

The first part of Eq. (III.45) is introduced to reproduce mainly the shock wave effect, as for the second part, it is introduced to take the blasthole gases effect into account (Fig. III.5).

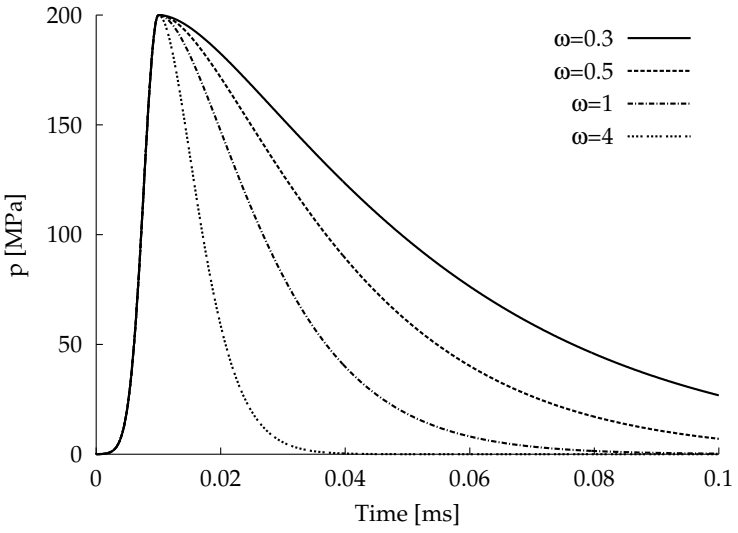

Figure III.5: Pressure-time history on the equivalent hole wall

III.3.1.2 Time-dependent fracture process

For a sufficient number of radial cracks, we assume that the fracture process can be simulated by using the constitutive law described in chapter II. The coupled rate dependent damage elasto-viscoplastic model will be used. Thus, the anisotropy introduced by radial cracks can be taken into account by the anisotropic damage model, while the compressive shear failure arround the equivalent hole, can be taken into account by the elasto-viscoplastic model. For complexe loading, the coupled models will be activated.

III.3.2 Cylindrical one-dimensional simulations

The constitutive model contains 12 parameters which can be fitted to a specific type of material from a series of experiments. The model response for uniaxial tests is given in section II.5.2. The following table gives these calibrated parameters in the case of a limestone rock type.

Elastic parameters		Elasto-Viscoplastic compression model parameters	
E(MPa)	64×10^3	K	3
ν	0.2	α_1	0.77
Tensile damage model parameters		w_c	10^5
		α	0.1
R_d(J/m^3)	7.8×10^2	R_c(MPa)	70
$v_d(s^{-1})$	5×10^6	$v_c(s^{-1})$	$30{\times}10^3$
n_d	2	n_c	2

In addition, we consider an equivalent hole with a radius equal to the blasthole radius multiplied by a factor 2. Fig. III.6 shows the pressure-time history used on the equivalent hole. p_0 can be approximated since the size of the crushed annulus can be determined by the

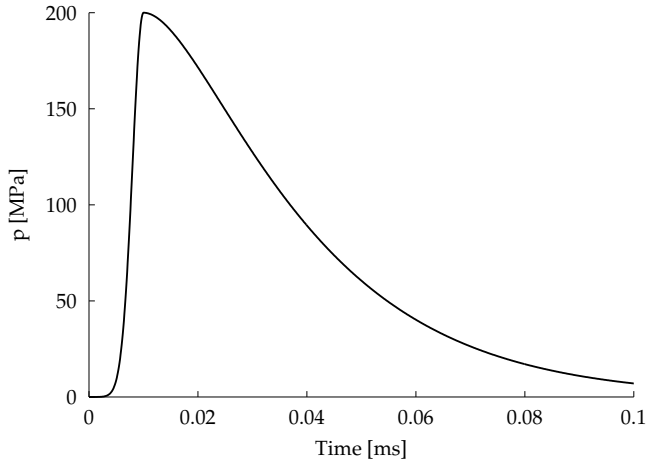

Figure III.6: Used pressure-time history

dynamic triaxial compressive strength of the rock.
The numerical results that will be described will concern three cylindrical samples : the first ($\mathcal{A}$) with a diameter of 300 mm, the second ($\mathcal{B}$) with a diameter of 100 mm, as for the third ($\mathcal{C}$), it will have a diameter of 100 mm and a fixed outside surface. Numerical solutions were obtained by using unifrom discretisations with 6 noded quadrilateral elements. 900, 300 and 300 elements were used for, respectively, sample ($\mathcal{A}$), ($\mathcal{B}$) and ($\mathcal{C}$). The time step used for computations, which were done with large strain formulation, was $\Delta t = 10^{-6}\ ms$.

Obtained numerical results indicate that the only damage tensor component which was influenced by stress waves is the tangential one. Otherwise, slabbing regions are absent which is in good agreement with experimental observations.
Fig. III.7, III.8 and III.9 show tangential stress at the inner surface of each sample. It can be seen that at first the tangential stress is tensile. When the tensile criterion is reached, tangential damage starts to increase and radial cracks appear. The compressive criterion is reached later. Fig. III.8 and III.9 show clearly that, for the same loading duration, boundary conditions can influence the stress state of the same material with the same geometry. Fig.

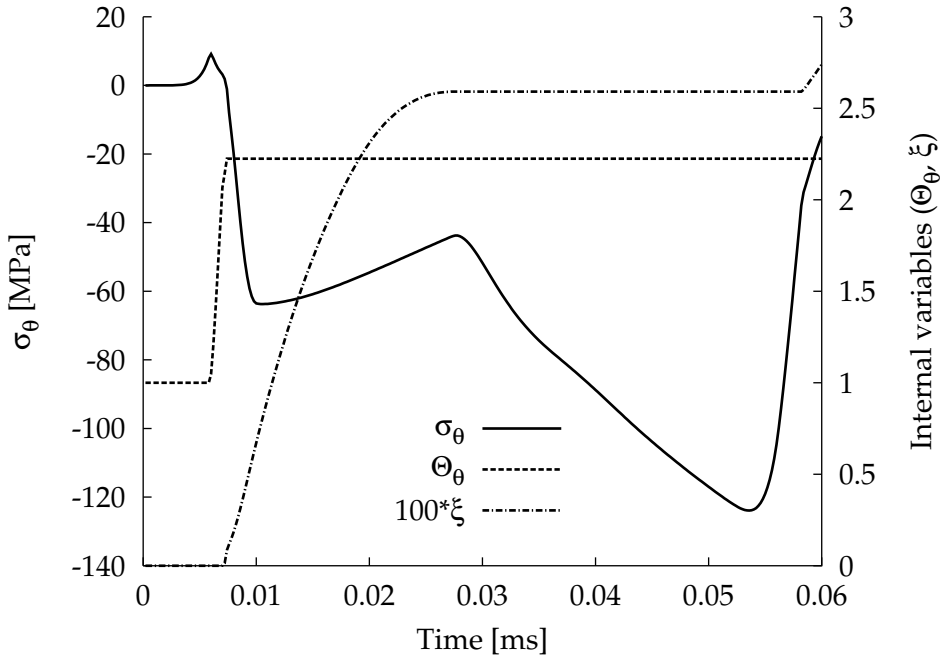

Figure III.7: Tangential stress, tangential damage and the softening variable as a function of time at the inner surface of sample ($\mathcal{A}$)

III.10, III.11 and III.12 show tangential stress at the medium of each sample. Negligible increase of tangential damage is shown in Fig. III.12 which indicates the absence of any failure mechanism. Howerver, Fig. III.10 and Fig. III.11 show two different failure mechanism. For sample ($\mathcal{A}$), failure is due to direct tensile stress, as for sample ($\mathcal{B}$), failure is the result of the reflected tangential stress.
Fig. III.13, III.14 and III.15 show tangential stress at the outside surface of each sample. Contrary to the cases of sample ($\mathcal{A}$) and sample ($\mathcal{B}$), the tangential stress at the outside surface of sample ($\mathcal{C}$) is compressive. Furthermore, this compressive state is too little to cause failure.
Fig. III.16, III.17 and III.18 show tangential damage and the softening variable as a function of radius at different times. As can be seen, two complementary region are clearly distinguished. The first region, in the close vicinity of the equivalent hole, is caused by shear failure mechanism. This region, of limited extent, is practically the same for the three considered samples. As regards the second region, commonly known as the fracture zone, the failure mechanism is due to tangential stress. For sample ($\mathcal{C}$), this region is absent since reflected tangential stresses are compressive.

III.4 Fragment size distribution prediction

In the previous section, the fracture process leading to material failure was described. Since, it is not feasible for the continuum description to account for the formation of discrete fragments, the obtained result, in terms of the thermodynamic state, of the time dependent fracture process are postprocessed to produce the fragment size distribution.
The cumulative mass of fragments having a size less than or equal to s is given by Eq. I.49. The mean fragment size is related to the mechanical quantity by Eq. I.45. In this study, we assume that the mechanical quantity is given by

$$G(\overrightarrow{x}) = \max_{t\in[0,\ T]} \left\langle \underline{\underline{\sigma}}(\overrightarrow{x},\ t) \right\rangle : \left\langle \underline{\underline{\dot{\epsilon}}}(\overrightarrow{x},\ t) \right\rangle \tag{III.46}$$

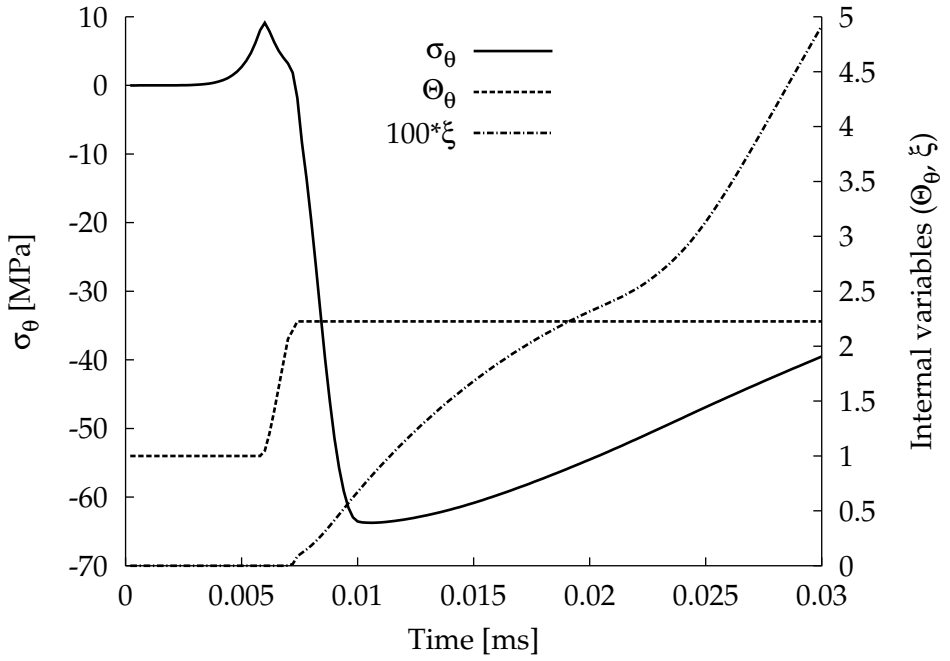

Figure III.8: Tangential stress, tangential damage and the softening variable as a function of time at the inner surface of sample ($\mathcal{B}$)

In order to show the capability of the proposed approach to predict the fragment size distribution, we consider again the three samples described in chapter I. The intrinsic function ψ is identified by curve fitting. The following empirical relationship is used

$$s_m(\overrightarrow{x}) = \psi\left(G(\overrightarrow{x})\right) = \begin{cases} \kappa\left(\frac{G(\overrightarrow{x})}{G_d}\right)^{-n_1} + s_{min} & \text{for } G(\overrightarrow{x}) \in [G_c,\ G_d[\\ \kappa\left(\frac{G(\overrightarrow{x})}{G_d}\right)^{-n_2} + s_{min} & \text{for } G(\overrightarrow{x}) \in [G_d,\ +\infty[\end{cases} \tag{III.47}$$

$(\kappa,\ n_1,\ n_2,\ s_{min},\ G_d) \in \mathbb{R}_+^5$ are **material parameters**. s_{min} and G_c are respectively the minimum fragment size and the critical mechanical quantity introduced in the first chapter. The fitting result for the considered samples is

$$\begin{cases} \kappa = 1.832 \text{ mm} \\ n_1 = 1.764 \\ n_2 = 6.601 \\ s_{min} = 0.023 \text{ mm} \\ G_d = 1.278 \text{ GPa/s} \end{cases} \tag{III.48}$$

Now, from numerical simulations of the fracture process we can calculate the distribution of the mechanical quantity G as a function of radius (Fig. III.19). Knowing the intrinsic function ψ, we can easily calculate the mean fragment size and therefore the fragment size distribution of each sample. Fig. III.20 shows that numerical predictions are in good agreement with experimental results.

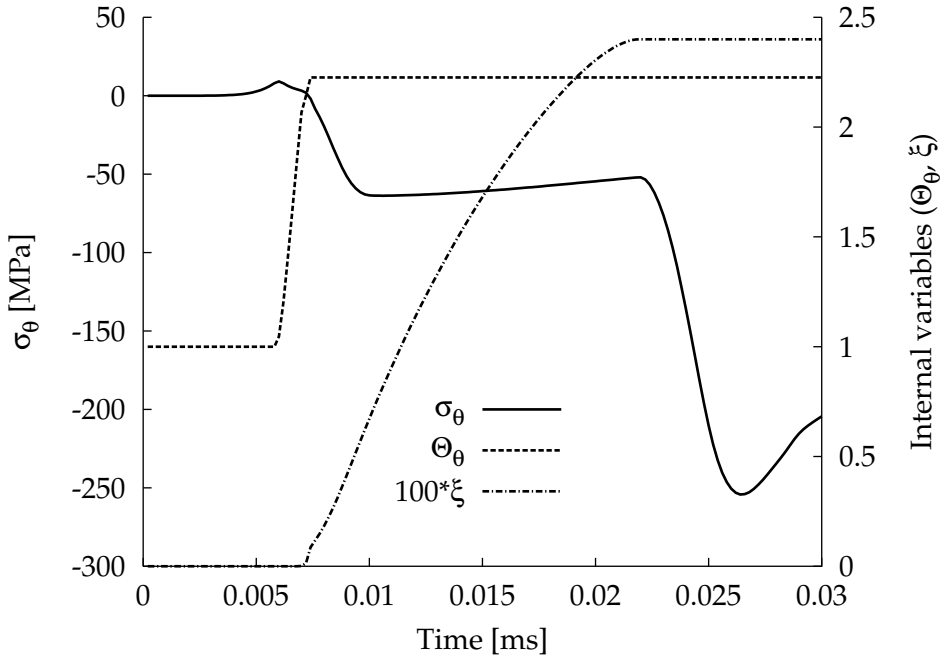

Figure III.9: Tangential stress, tangential damage and the softening variable as a function of time at the inner surface of sample ($\mathcal{C}$)

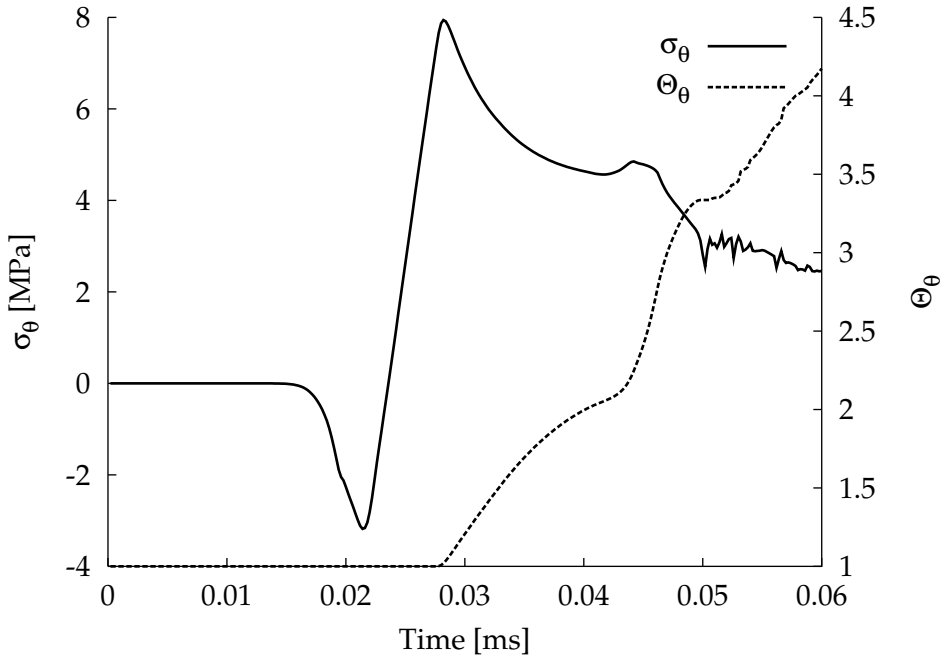

Figure III.10: Tangential stress and tangential damage as a function of time at the medium of sample ($\mathcal{A}$)

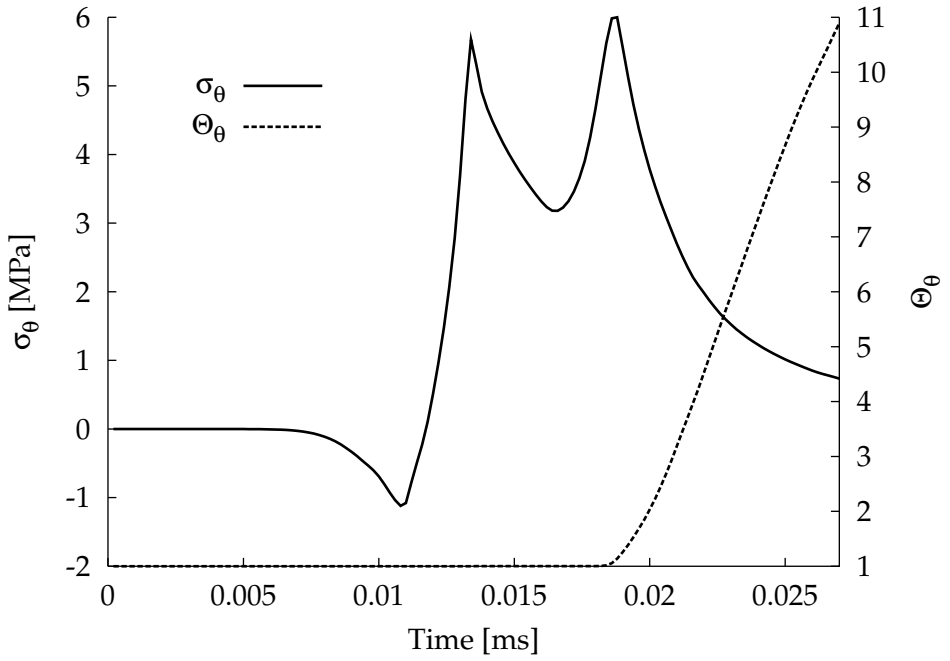

Figure III.11: Tangential stress and tangential damage as a function of time at the medium of sample ($\mathcal{B}$)

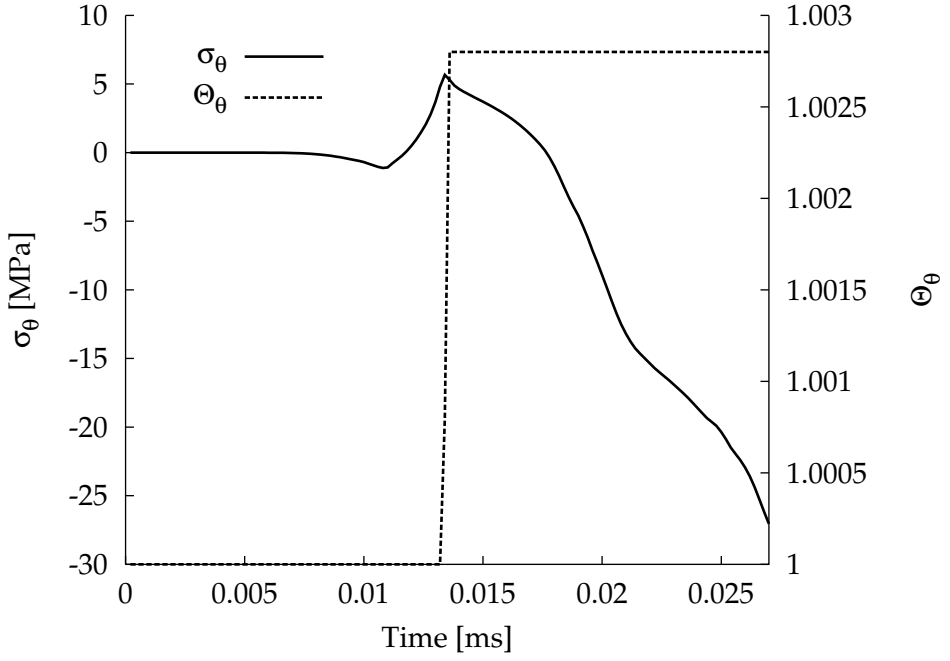

Figure III.12: Tangential stress and tangential damage as a function of time at the medium of sample ($\mathcal{C}$)

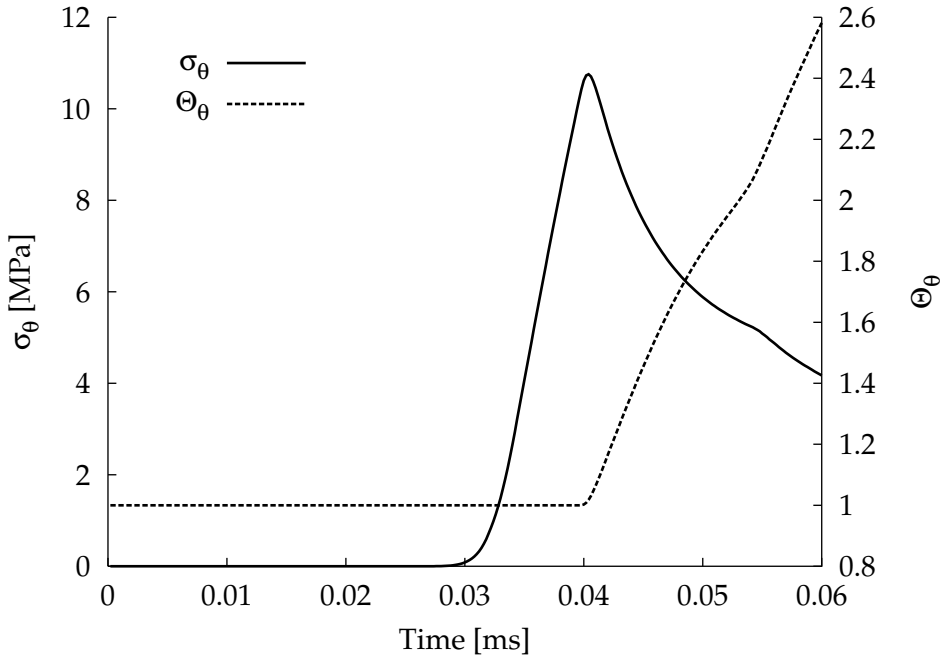

Figure III.13: Tangential stress and tangential damage as a function of time at the outside surface of sample ($\mathcal{A}$)

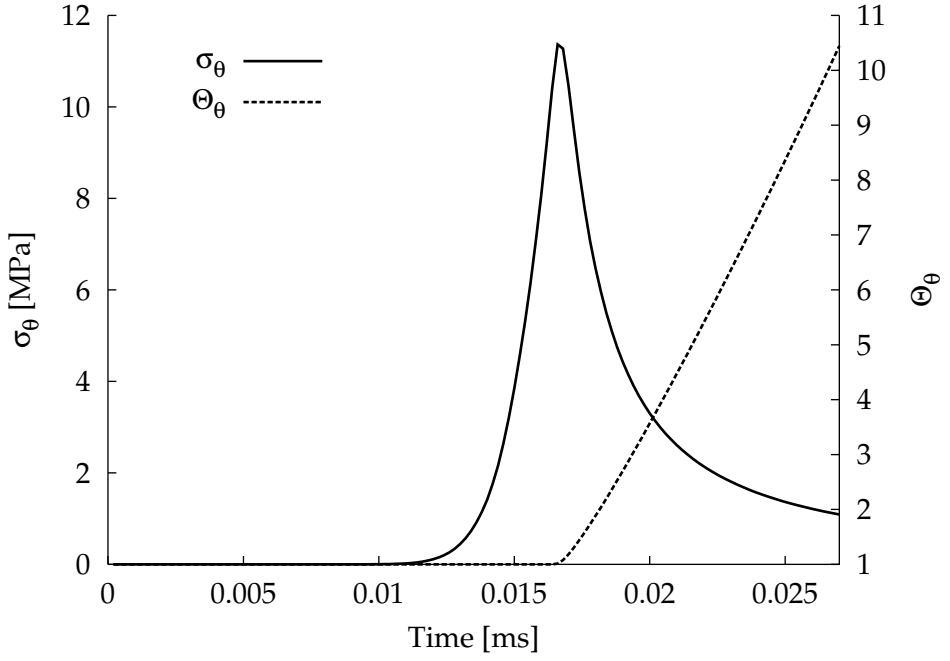

Figure III.14: Tangential stress and tangential damage as a function of time at the outside surface of sample ($\mathcal{B}$)

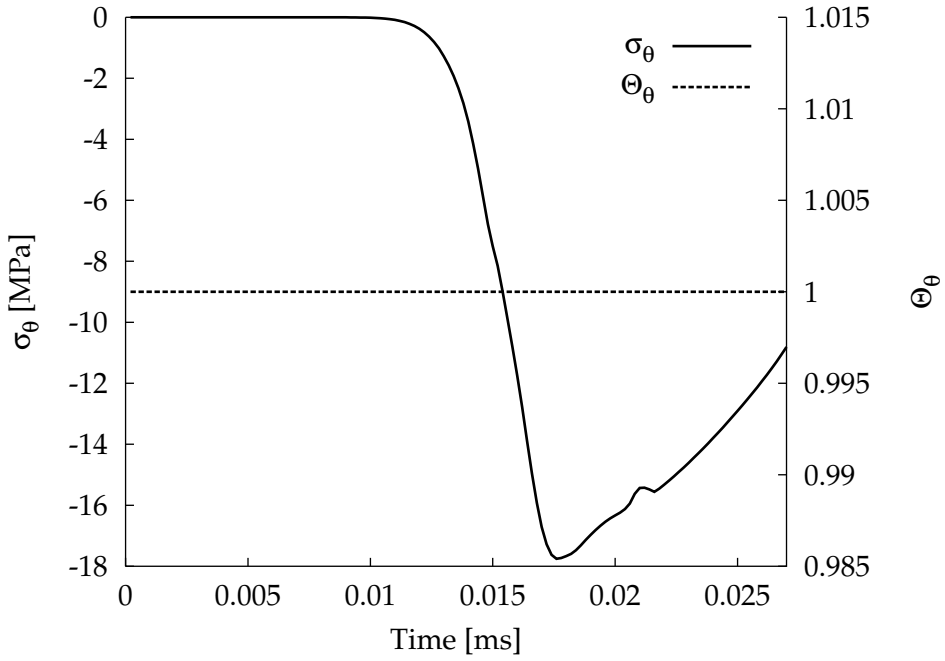

Figure III.15: Tangential stress and tangential damage as a function of time at the outside surface of sample ($\mathcal{C}$)

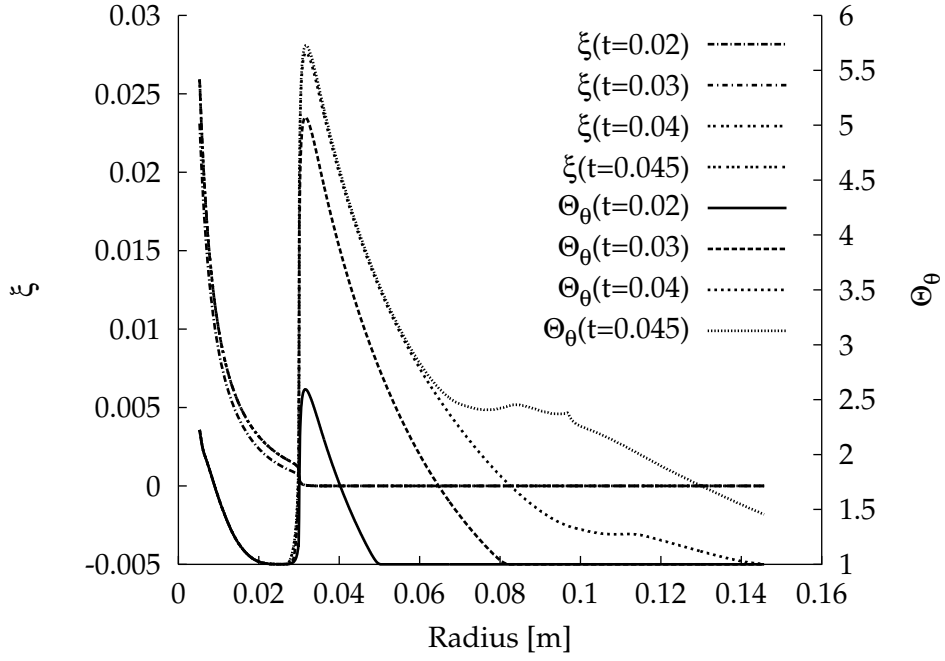

Figure III.16: The softening variable and the tangential damage as a function of radius for Sample ($\mathcal{A}$)

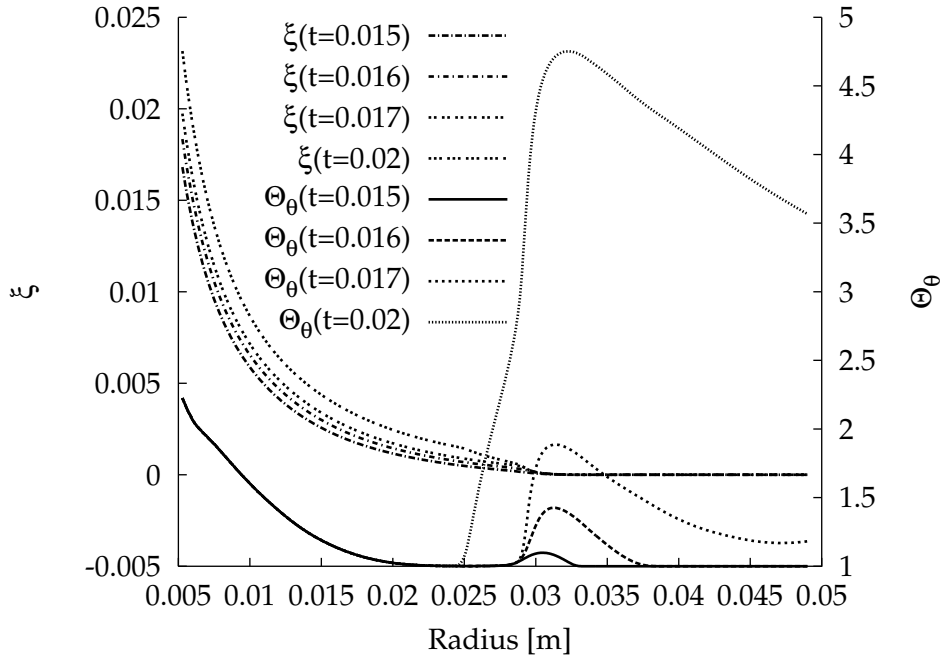

Figure III.17: The softening variable and the tangential damage as a function of radius for Sample ($\mathcal{B}$)

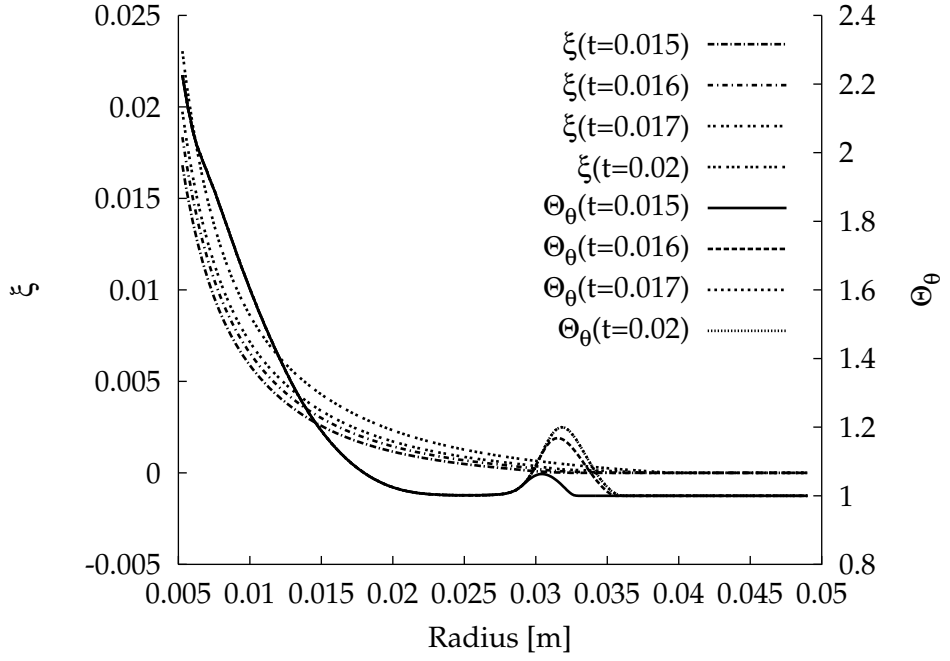

Figure III.18: The softening variable and the tangential damage as a function of radius for Sample ($\mathcal{C}$)

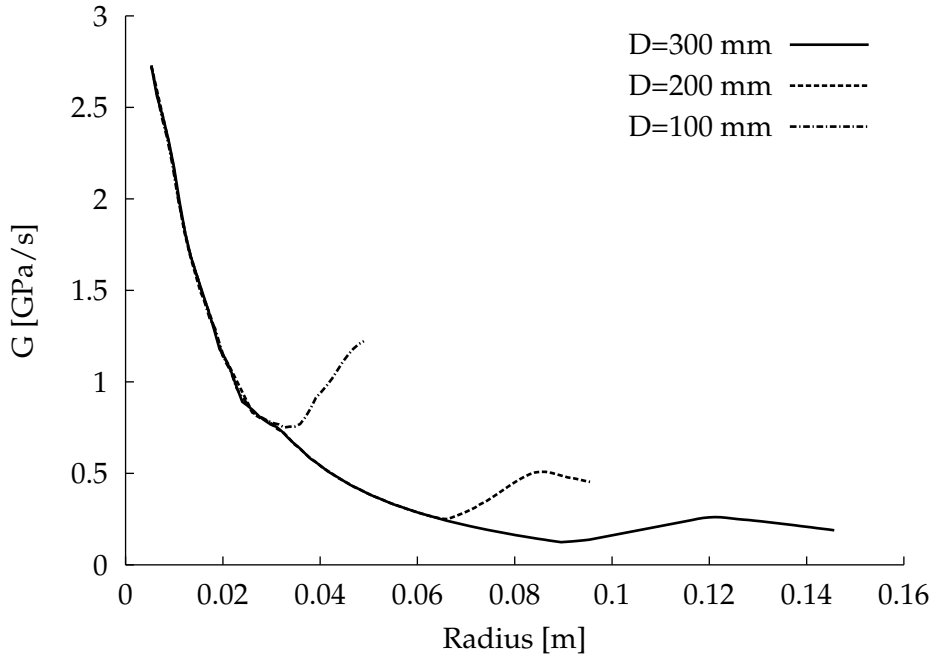

Figure III.19: G as a function of radius

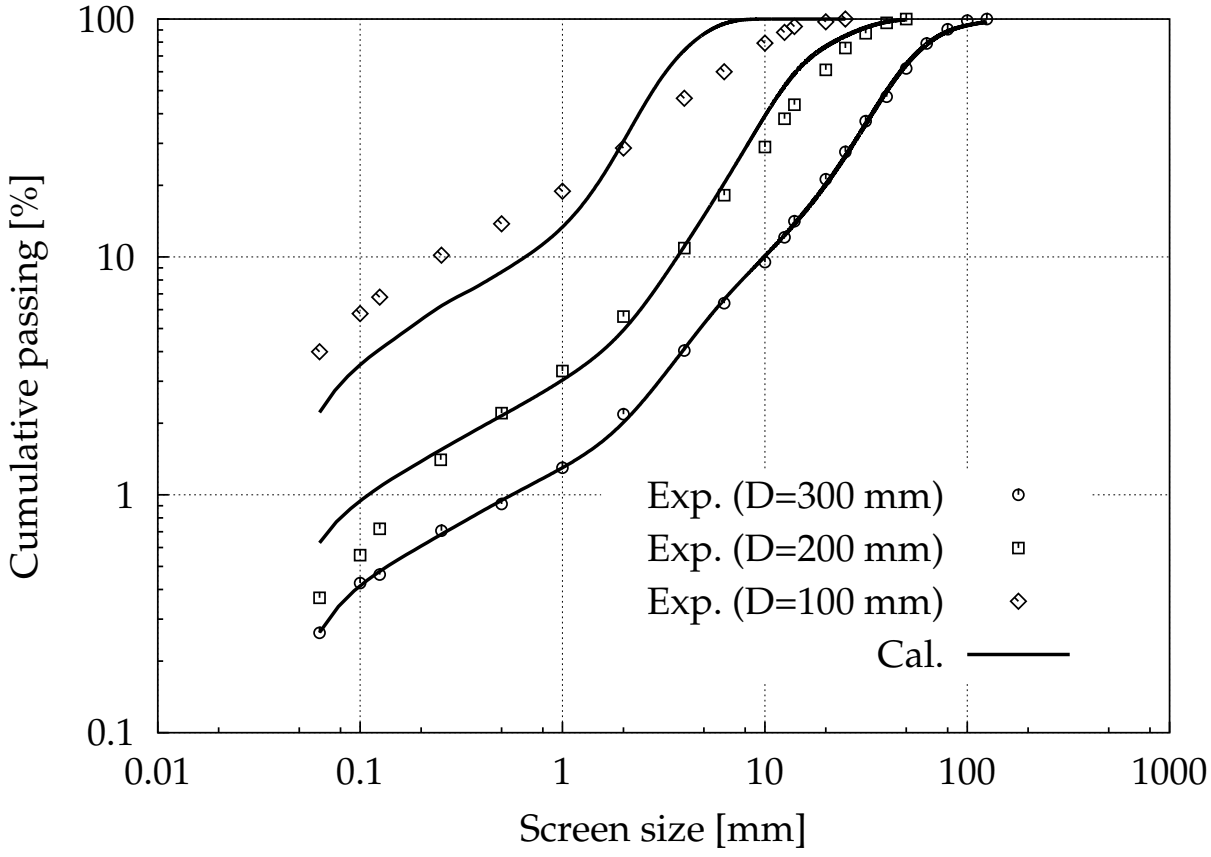

Figure III.20: Comparison of experimental and calculated particle distributions

References

Chéret R., 1988. *La détonation des explosifs condensés - Tome I.* Série scientifique, Masson.

Chéret R., 1989. *La détonation des explosifs condensés - Tome II.* Série scientifique, Masson.

Bhandari S., 1997. *Engineering rock blasting operations.* AA. Balkema, Rotterdam.

Borovikov V.A., Vanyagin I.F., 1995. *Modelling the effect of Blasting on Rock Breakage.* A.A. Balkema/Rotterdam, Brookfield.

Meyers M.A., 1994. *Dynamic behavior of materials.* John Wiley & sons, Inc.

Mohanty B., 1996. *Rock fragmentation by blasting.* A.A. Balkema/Rotterdam, Brookfield.

Rossmanith H.P, 1993. *Rock fragmentation by blasting.* A.A. Balkema/Rotterdam, Brookfield.

Tijani M., 1993. *Onde élastique autour d'une cavité sphérique ou cylindrique.* rapport interne, CGES, Ecole des Mines de Paris, France.

Whittaker B.N., Singh R.N., Sun G., 1992. *Rock Fracture Mechanics, Principles, Design and Applications.* Elsevier science publishers B.V.

Conclusions and prospects

Une formulation pour décrire et prévoir le comportement et la fragmentation des matériaux quasi-fragiles sous des chargements dynamiques sévères a été développé en utilisant les hypothèses principales suivantes :

- *Les hétérogénéités à grande échelle sont ignorées. A petite échelle, nous supposons qu'une éprouvette de laboratoire est mécaniquement homogène et continue.*
- *Le processus de rupture, dépendant du temps, peut être décrit en utilisant un modèle phénoménologique qui reproduit mathématiquement les relations macroscopiques de contrainte-déformation pour différentes conditions de chargements, négligeant les mécanismes microscopiques du comportement.*
- *Basé sur l'historique de l'état thermodynamique du matériau, nous postulons que nous pouvons remonter, en utilisant un post-traitement adéquat, à la taille des fragments.*

*Par conséquent, en utilisant ces considérations, un modèle approprié au comportement des matériaux quasi-fragiles a été développé. Il est capable de décrire le comportement non linéaire et l'anisotropie induite par le chargement. Le modèle est alors implanté dans un code de calcul par éléments finis (*Viplef3d*). Son intégration conduit au développement d'une méthode de relaxation permettant une actualisation explicite de ses variables. D'autre part, en se basant sur les essais de fragmentation en laboratoire, un modèle de fragmentation dynamique est présenté pour prédire la distribution granulométrique.*
L'approche développée est alors appliquée pour modéliser la fragmentation, en laboratoire, des roches à l'explosif. Les capacités du modèle sont alors évaluées par comparaison des résultats expérimentaux et numériques.
Cependant, ce travail pose plus de questions qu'il en répond. Dans ce qui suit, je décrirai mon point de vue concernant les futurs développements concernant les besoins liés aux domaines du comportement rhéologique, de la fragmentation dynamique et de la fragmentation des roches à l'explosif.

Comportement rhéologique: *les modèles analytiques du comportement statique ou dynamique des matériaux quasi-fragiles soumis à un large spectre de contraintes et de déformations sont souvent basés sur des lois constitutives phénoménologiques déduites des observations macroscopiques, ce qui était le cas dans cette thèse. En conséquence, les capacités prédictives de n'importe quel modèle phénoménologique dépendront essentiellement des données sur lesquelles il est basé. Malheureusement, actuellement les techniques expérimentales ne sont pas assez développées et les interprétations des données, en particulier quand il s'agit d'un matériau fragile ou quasi-fragile, sont encore incertaines. En effet, des efforts considérables doivent être adressés pour développer des techniques expérimentales précises et capables d'identifier le comportement intrinsèque des matériaux et en particulier pour clarifier le caractère adoucissant et l'effet de la dynamique sur la résistance des matériaux quasi-fragiles.*
D'autre part, bien que le progrès dans la modélisation continue de la rupture statique et dynamique soit encourageant, il est évident que plus de développements sont nécessaires. En particulier, pour une meilleure compréhension du processus de la rupture, des modèles physiques plus réalistes devraient être étudiés. Les modèles phénoménologiques, où une description locale de la rupture est employée, semblent être inadéquats pour des matériaux présentant un adoucissement. En fait, pour les modèles indépendants du temps physique, la solution numérique, obtenue par éléments finis et utilisant l'élastoplasticité standard, où une description locale de la rupture est employée, indique une grande dépendance à l'égard du maillage comme discuté dans cette thèse. Cette dépendance du maillage est la conséquence du problème mathématique mal posé, c.-à-d. le problème aux limites perd son ellipticité en statique et son hyperbolicité en dynamique. Ceci signifie que, pour la dynamique par exemple, les ondes ne peuvent plus se propager et la déformation est localisée dans une bande infiniment étroite dans laquelle les déformations peuvent évoluer indéfiniment. Ainsi, des modèles incorporant des formulations évoluées doivent être étudiés. L'ajout de termes non locaux ou de type gradients aux modèles constitutifs semblent être une approche attrayante, particulièrement dans des problèmes dynamiques où le caractère dispersif de la propagation des ondes joue un rôle important dans le processus de la rupture. Ces modèles utilisent, pour la plupart, une longueur intrinsèque liée à la micro-structure et aux mécanismes de rupture.

fragmentation dynamique: *le modèle phénoménologique utilisé pour la prédiction de la distribution granulométrique semble être attrayant, particulièrement quand le matériau à fragmenter se trouve bien caractérisé. Cependant, la relation locale entre la taille moyenne des fragments et la quantité mécanique responsable de la fragmentation semble être inappropriée pour des faibles chargements dynamiques où la fragmentation peut être considérée comme structurale. A cet égard, d'autres études doivent être entreprises pour mieux clarifier la transition entre la fragmentation statique et celle dynamique. Des données expérimentales additionnelles de haute qualité sont également nécessaires pour dériver un modèle général de fragmentation.*

Fragmentation des roches à l'explosif: *les performances des tirs à l'explosif sont déterminées par l'interaction des produits de détonation de l'explosif et de la roche environnante. Dans notre modélisation numérique l'effet de l'explosif est introduit par l'utilisation d'une pression, fonction du temps, exercée sur un trou équivalent. On a montré que la durée et la forme de la courbe de pression-temps peuvent influencer directement les mécanismes de rupture.*

Maintenant, je suis convaincu qu'un chargement en terme de pression-temps n'est qu'une approximation grossière et d'autres études doivent être entreprises pour mieux tenir compte du problème couplé comportant le processus de détonation et ceux de la rupture, de la fracturation et de la fragmentation de la roche. L'action de l'onde de choc sur le broyage de la roche autour du trou de charge doit être également le résultat du problème couplé. A cet égard, les modèles utilisant des équations d'état ou, dans le cadre de plasticité, une surface de charge à écrouissage positif et fermée sur l'axe hydrostatique afin de modéliser l'effet de l'onde de choc semblent être inadéquats. En fait, ces modèles indiquent essentiellement que l'interaction explosif-matériau aura comme conséquence un mécanisme de rupture caractérisé par la compaction des vides et des pores du matériau. De tels modèles ne peuvent pas reproduire la vraie interaction explosif-matériau qui est extrêmement complexe, puisqu'elle comporte l'interaction des ondes de détonation, des ondes de chocs, l'expansion des gaz et la circulation des gaz dans les fissures crées. Dans des problèmes de tir réels, il est évident que les propriétés du massif rocheux influenceront le processus de la fragmentation. En effet, les propriétés de la roche intacte ainsi que les discontinuités jouent un rôle important dans la détermination de la distribution granulométrique la plus appropriée. Basé sur l'approche développée dans cette thèse, la distribution des fragments de la roche intacte lors d'un tir à l'explosif peut être obtenu. D'autre part, la distribution initiale des bloc formant le massif rocheux peut être également déterminée en utilisant des méthodes de probabilité et de statistiques. Ainsi, à l'avenir, la recherche pourra se concentrer sur la manière de combiner ces différentes données afin de développer une méthodologie complète qui pourra être utilisée dans des applications industrielles.

A formulation for describing and predicting the behaviour and the fragmentation of quasi-brittle materials under high dynamic loadings has been constructed utilizing the following main assumptions:

- Material's heterogeneities on large scale are ignored. On small scale, we assume that a laboratory-sized specimen is mechanically homogeneous and continuous.
- The time dependent fracture process can be described by using a phenomenological model which reproduces mathematically the macroscopic stress-strain relations for different loading conditions, neglecting the microscopic mechanisms of the behaviour.
- Based on the history of the material's thermodynamic state, we postulate that we can go up to the fragment size by a post-processing analysis.

Therefore, using these considerations a suitable constitutive model for quasi-brittle materials has been developed. The model is capable of describing the rate-dependent non-linear behaviour and the load-induced anisotropy. This constitutive model is then implemented in a finite element program (VIPLEF3D). The integration of the rate dependent damage elasto-viscoplastic constitutive model leads to the development of a relaxation method characterized by an explicit updating of the model's variables.
On the other hand, based on experimental laboratory blasting tests, a dynamic fragmentation model is introduced to account for the fragment size distribution.

The developed approach is then applied to the modelling of the laboratory rock fragmentation by blasting. The model capabilities are then evaluated through the comparison between experimental and numerical results.

However, this work still asks more questions than it answers. In what follows, I will outline my point of view on future basic research needs in constitutive modelling, dynamic fragmentation and rock fragmentation by blasting fields.

Constitutive modelling

Analytical models of static or dynamic behaviour of quasi-brittle materials to large spectrum of stress states and strain rates are often based on phenomenological constitutive laws deduced from macroscopic observations, which was the case in this thesis. In consequence, the predictive capability of any phenomenal model will depend critically on the data on which it is based. Unfortunately, at present, techniques for experiments are not well developed and interpretation of data, in particular when the material behaves in brittle or quasi-brittle manner, are still questionable. Indeed, tremendous effort must be addressed to develop accurate experimental techniques able to identify the intrinsic material behaviour and especially to clarify the softening behaviour and the strength time-dependence of quasi-brittle materials.
On the other hand, although progress in continuum modelling of static and dynamic failure, is encouraging, it is apparent that further advancements are needed. In particular, for a best understanding of failure process, more realistic physical models should be investigated. Phenomenological models, where a local description of the softening material is used, seem to be inappropriate for materials exhibiting strong strain softening. In fact, for rate-independent models, the numerical solution which is obtained from finite element analyses employing standard continuum elasto-plasticity, where a local description of the softening material is used, reveals a great dependence on the fineness of the finite element mesh as discussed in this thesis. This mesh-dependency is the consequence of the ill-posedness of the mathematical problem, i.e. the Initial Boundary-Value Problem loses ellipticity in statics or hyperbolicity in dynamics. This means that, in dynamics for example, loading waves can no longer propagate and the deformation is trapped in an infinitely narrow band in which the strain can grow unboundedly. Thus, models incorporating higher-order formulations must be investigated. Adding nonlocal or gradient terms to the constitutive modelling appear to be an attractive approach, especially in dynamic problems where the dispersive character of wave propagation plays an important role in the fracture process. These models use, for the most part, an intrinsic length scale which is related to the microstructure and the failure mechanisms during fracture process.

Dynamic fragmentation

The phenomenal model used to predict the fragment size distribution seems to be an attractive approach, especially when the material to be fragmented is well characterized before energy input. However, the local relationship between the mean fragment size and the mechanical quantity appears to be not valid for low dynamic loadings where the fragmentation can be defined as a structural failure. In this regard, further studies must be undertaken to better clarify the transition between static and dynamic fragmentation. Additional high-quality experimental data is also needed to derive a general fragmentation model.

Rock fragmentation by blasting

Blasting performances are determined by the interaction of the detonation products of the

explosive and the confining rock mass. In our numerical modelling the blast loading is introduced by using a pressure-time history on an equivalent hole. It was shown that the magnitude, duration and shape of the pressure-time curve can influence directly the fracture mechanisms.

Now, I am convinced that a pressure-time history is only a crude approximation and further studies must be undertaken for better taking into account the coupling problem involving detonation process and the breaking, the fracturing and the fragmentation of the rock. The crush action of shock wave around the borehole must also be the result of the coupled problem. At this regard, models using equations of sate or, in plasticity framework, a hardening closed yield surface on the hydrostatic pressure side for the purpose of modelling the shock wave effect seem to be inappropriate. In fact, these models essentially indicate that the explosive-material interaction will result in a failure mechanism characterized by the compaction of material voids and pores. Such models are unable to reproduce the real explosive-material interaction which is extremely complex, since it involves detonation waves, shock waves, expanding gazes, gas flow through induced cracks, and their interrelationships. In real blasting problems, it is evident that the rock mass properties will influence the fragmentation process. Indeed, the properties of both the intact rock and the discontinuities play an important role in determining the most suitable fragmentation distribution with a minimum cost. Based on the approach developed in this thesis, the blasting fragmentation distribution of the intact rock can be obtained. On the other hand, the initial block distribution can also be determined by using probability and statistics methods. Thus, future work can focus on the way to combine these different data in order to develop a complete methodology which can be used in real industrial applications.